Comenius University in Bratislava

Faculty of Mathematics, Physics and Informatics

Department of Astronomy, Physics of the Earth, and Meteorology

Diagnostics of the Non-Maxwellian Electron Distributions in the Solar Corona and Transition Region

Dissertation Thesis

4.1.7 Astronomy & 4.1.8. Astrophysics

Supervisor: doc. RNDr. Elena Dzifčáková, CSc.

Consultant: RNDr. Jaroslav Dudík, PhD.

RNDr. Šimon Mackovjak

Bratislava, 2014

The author declares that he made this thesis on his own and using stated literature.

RNDr. Šimon Mackovjak

Acknowledgments

Abstract

RNDr. Šimon Mackovjak.

Diagnostics of the Non-Maxwellian Electron Distributions in the Solar Corona and Transition Region

[Dissertation Thesis]

Comenius University in Bratislava.

Faculty of Mathematics, Physics and Informatics.

Department of astronomy, physics of the Earth and meteorology.

Supervisor: doc. RNDr. Elena Dzifčáková, CSc.

Consultant: RNDr. Jaroslav Dudík, PhD.

Degree: PhD in 4.1.7 Astronomy & 4.1.8. Astrophysics.

Bratislava: FMPI UK, 2014, p 107

The non-Maxwellian κ-distributions have been detected in various space plasmas, including solar wind. However, no evidence of their presence in the solar corona has been found yet. The PhD thesis is focused on diagnostics of κ-distributions of electrons in the solar corona and transition region using spectroscopic data. The diagnostic methods were proposed by Dzifčáková and Kulinová (2010) for spectral lines of iron ions. These methods are here extended using lines of other ions. Lines suitable for diagnostics of κ, as well as density and temperature were selected. A specialized observation for the Hinode/EIS instrument were prepared and carried out. This dataset is analyzed and diagnosed parameters of coronal plasma are presented and discussed here. The diagnosed results shown that the investigated plasma is unlikely to be Maxwellian. The differential emission measure (DEM) of different solar regions were investigated and the influence of κ-distribution to the DEM were shown. For lower κ, the peaks of the DEMs are typically shifted to higher temperatures and the DEMs themselves become more wider. The PhD thesis provides straightforward analysis from theoretical diagnostic method to application on obtained data. The results presented here challenge the traditional Maxwellian analysis of coronal observations.

Keywords: solar corona – κ-distributions – spectroscopy – plasma diagnostics – differential emission measure

Abstrakt

RNDr. Šimon Mackovjak.

Diagostika ne-maxwellovských distribúcií elektrónov v slnečnej koróne a prechodovej oblasti

[Dizertačná práca]

Univerzita Komenského v Bratislave.

Fakulta Matematiky, Fyziky a Informatiky.

Katedra astronómie, fyziky Zeme a meteorológie.

Školiteľ: doc. RNDr. Elena Dzifčáková, CSc.

Konzultant: RNDr. Jaroslav Dudík, PhD.

Stupeň: PhD v odbore 4.1.7 Astronómia & 4.1.8. Astrofyzika.

Bratislava: FMFI UK, 2014, str. 107

Ne-maxwelovské κ-distribúcie boli úspešne detegované vo viacerých formách vesmírnej plazmy. Ich prítomnoť v slnečnej koróne však dosiaľ nebola jednoznačne preukázaná. Predkladaná dizertačná práca sa venuje diagnostike κ-distribúcií elektrónov v slnečnej koróne a prechodovej oblasti zo spektroskopických dát. Metódy na tento typ diagnostiky boli navrhnuté v práci Dzifčáková and Kulinová (2010) pre spektrálne čiary iónov železa. Tieto metódy boli v našej práci rozširené na použitie s iónmi ostatných prvkov. Spektrálne čiary a ich pomery, vhodné na diagnostiku κ-distribúcií, hustoty a teploty, boli nájdené a nami navrhnuté na špecifické pozorovanie na satelite Hinode/EIS. Dáta z tohoto pozorovania boli analyzované a získane diagnostikované parametre sú v práci prezentované a diskutované. Výsledky ukázali, že skúmaná plazma nezodpovedá Maxwellovej distribúcii. V práci sme tiež skúmali vplyv κ-distribúcií na diferenciálnu emisnú mieru (DEM) v rozličných oblastiach Slnka. Pre nízke hodnoty κ sú DEM píky širšie a sú posunuté k vyšším teplotám. Dizertačná práca prezentuje priamočiaru analýzu od teoretických diagnostických metód po priame použitie na nami získané dáta. Prezentované výsledky namietajú na vhodnosť použitia Maxwellovej distribúcie v analýze pozorovaní slnečnej koróny.

Kľúčové slová: slnečná koróna – κ-distribúcie – spektroskopia – diagnostika plazmy – diferenciálna emisná miera

Contents

Introduction

The main role of the space science is to explore the universe. The observations are in this process absolutely essential. In this sense, the solar physics is a very privileged part of space science, due to its numerous ground and space-borne observatories with a multitude of high-precision data. Despite that, there are many processes which are unresolved and their nature is still too complicated.

The assumption that the energies of the particles in the solar atmosphere are distributed by Maxwellian distribution is commonly used in the scientific community. Most of the present-day observations are interpreted under this assumption, although the non-Maxwellian distributions would offer physically more consistent interpretation. Departures from the Maxwellian distribution are argued to be ubiquitous in the solar atmosphere above $R = 1.05\,R_{\mathrm{Sun}}$ (Scudder and Karimabadi, 2013). In this respect, dynamic or nonlocal effects give rise to the κ-distributions characterized by suprathermal, high-energy tails (e.g., Vasyliunas, 1968; Owocki and Scudder, 1983; Shoub, 1983; Leubner, 2002; Tsallis, 2009; Livadiotis and McComas, 2013). The κ-distributions were detected in solar wind (e.g. Collier et al., 1996; Maksimovic, Pierrard and Riley, 1997; Zouganelis, 2008; Le Chat et al., 2011), outer heliosphere (Decker et al., 2005), inner heliosheath (Livadiotis and McComas, 2012), and also in the solar transition region (e.g., Pinfield et al., 1999; Dzifčáková and Kulinová, 2011) and flare plasmas (Kašparová and Karlický, 2009; Oka et al., 2013). However, direct evidence for the presence of κ-distributions in the solar corona is still lacking (Feldman et al., 2007) or ambiguous.

Dzifčáková and Kulinová (2010) proposed a method for the diagnostics of the κ-distributions in the solar corona using spectral lines of iron ions. In our PhD thesis, we extended this analysis and the first intended goal was to explore the possibility to diagnose the κ-distributions using the spectral lines of the other elements that can be observed by the Extreme-Ultraviolet Imaging Spectrometer (EIS) (Culhane et al., 2007) onboard of the Hinode satellite (Kosugi et al., 2007).

These could offer the "missing piece of the puzzle" in the investigation of origin and presence of the κ-distributions in our solar system plasma. Successful diagnostics of κ-distributions could be also important for interpretation of the conditions in the solar corona. Second goal of this PhD thesis was the analysis of direct influence of κ-distributions on temperature structure of the solar plasma, characterized by differential emission measure (DEM).

The organization of PhD thesis is as follows. In Chapter 1 we present basic information about solar upper atmosphere and its observation. Chapter 2 gives an overview of observations and detections of κ-distributions in the space plasma. Definition of the κ-distributions and their properties are also given. Fundamentals of spectral synthesis and influence of κ-distributions on spectral lines are presented in Chapter 3. The chapters $4-6$ consists of our original research. In Chapter 4 we introduced the diagnostic methods and investigated the sensitivity of EUV line ratios to the κ-distributions. We analyzed the spectral lines of ions belonging to elements Al, Ar, Ca, Mg, Ni, O, S, and Si and subsequently the possibility to diagnose parameter κ from Hinode/EIS spectra. The diagnostic methods are applied in Chapter 5 on the data observed by our proposal on Hinode/EIS. The plasma parameters, κ, temperature, and electron density were determined for an observed coronal loop. In Chapter 6 we analyzed effects of κ-distributions on the calculated DEM that show us temperature structure of emitting plasma. We performed DEM reconstruction on three active region cores, quiet Sun region and prominence-corona transition region data and discussed the results for Maxwellian and κ-distribution.

The PhD thesis contains results that were presented on several international scientific meetings (e.g., 13th European Solar Physics Meeting, 5th and 6th Coronal Loops Workshop, Hinode 6 meeting, 15th and 16th Consultation of Solar Physics meeting) and have been published in refereed papers (Mackovjak et al., 2013, 2014) and conference proceedings (Dzifčáková et al., 2013). It also contains analysis and some preliminary results already presented in rigorous thesis (Mackovjak, 2013).

Chapter 1

The upper solar atmosphere and its observations

1.1 The solar corona and the transition region

The solar atmosphere consists of several well characterized layers: photosphere, chromosphere, transition region and corona. The photosphere is the bottom layer that emits almost all radiation in the visible part of spectrum and its base constitutes the boundary between solar interior and solar atmosphere with typical temperature about 5700 K. The chromosphere, the layer above photosphere, is observable in selected spectral lines, usually in H_α line with wavelength 6562.8 Å. The temperature in the chromosphere rise up to 20 000 K. The transition region is a strongly structured thin layer which separates the chromosphere from the solar corona. The temperature in this layer rises from chromospheric values up to 1 MK. Therefore, it is strongly unhomogenous with a high gradient of temperature and density. The solar corona as the upper layer of solar atmosphere was historically observed only during total solar eclipses. The progress in physics and observation techniques results in wide understanding of physical parameters and processes of the solar atmosphere plasma. Nevertheless, there are still many problems that are unresolved. One of them is the coronal heating problem, with the mechanism causing the dramatic increase of temperature from photosphere to corona. The basic properties of the solar atmosphere, temperature of electrons T [K], densities [cm^{-3}] of neutral hydrogen atoms (N_H) and electrons (N_e), are plotted in Fig. 1.1.

The solar corona is much less intensive than the visible disk of the Sun. The maximum brightness ratio of the corona to the photosphere is about 10^{-6}, and it decreases to $\approx 10^{-9}$
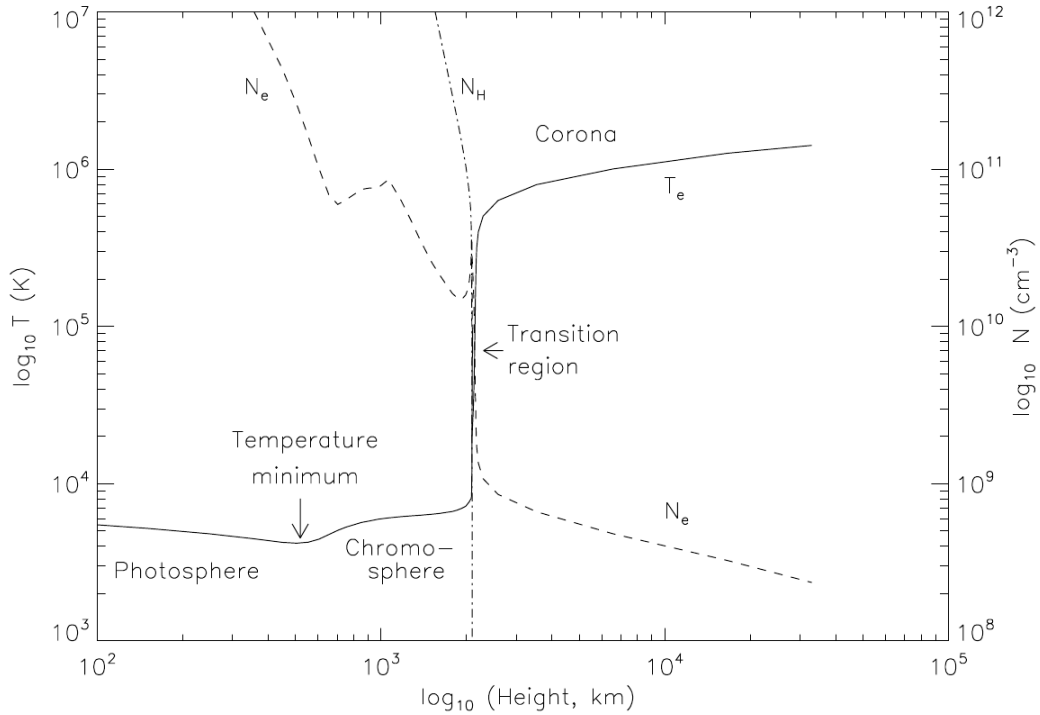
Figure 1.1: The variation of electrons temperature T (solid curve), number density of neutral hydrogen atoms N_H (dot-dash curve) and electrons N_e (dash curve) with height in the solar atmosphere. The model is based on the calculation of Vernazza et al. (1981), Fontenla et al. (1988), and Gabriel (1976) for the quiet Sun (Phillips et al., 2008, Fig 1.1).

within a single solar diameter away from the visible limb. Nevertheless, corona is well observable in different wavelengths by specialized space and ground-based instruments (Fig. 1.2). There are three main components that contribute to the coronal radiation. They are distinguished by the mechanisms producing the radiation and are labeled as the K, F, and E corona. The continuous spectrum of K corona originates by scattering of the photospheric light on the coronal free electrons. The F corona is actually unrelated to the corona itself. It arises out of scattering of the photospheric light by small dust particles in the ecliptic plane, and it may be though of as the inner zodiacal light. The E corona is the only component that represents true emission of coronal plasma. It consists of emission in isolated spectral lines formed by the high-temperature coronal ions. Therefore, it is possible to observe many of these lines quite clearly by using spectrometers or narrow-band filters centered on the desired wavelengths. The characterization of the transition region is more complicated and mainly it serves as a natural demarcation of the corona which is very inhomogeneous.
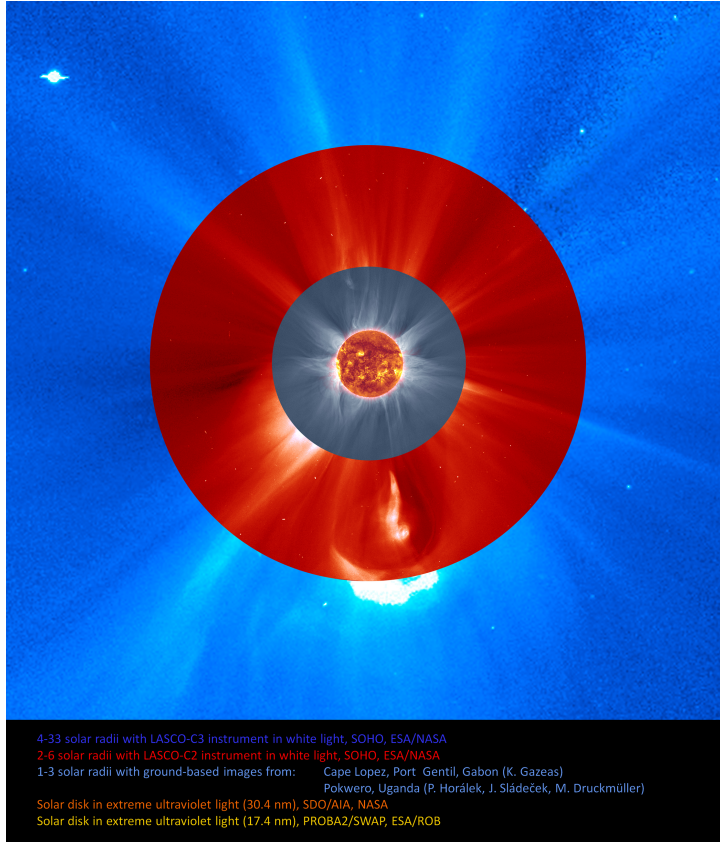
Figure 1.2: A composition of space and ground-based observations of the Sun in different wavelengths. The observations were obtained during the solar eclipse on 3 November 2013. The result is an overall view of the solar corona extending far out into space. Particular observations, instruments, and credits are indicating in the figure by different colors (*www.esa.int/spaceinimages/Images/*2013/12/*Multiwavelength_solar_view*).

1.2 Space-borne instruments

The earth atmosphere inhibits the transfer of radiation with wavelengths bellow $\sim 2000\,\text{Å}$. The observation of upper solar atmosphere in the ultraviolet (UV), extreme-ultraviolet (EUV) and X-ray spectral ranges are possible only via space-borne telescopes. Here, we introduce three present-day instruments that observe regions of upper solar atmosphere and their data are used in our work. The instruments differ in observed spectral ranges, spectral resolution, accessibility of the data, etc., but all of them offer possibility to investigate the environment of the different solar structures.

The SUMER - Solar Ultraviolet Measurements of Emitted Radiation (Wilhelm et al., 1995)

was designed to investigate structures of associated dynamical processes occurring in chromosphere, transition region, and the inner corona, over temperatures from $10,000\,\text{K}$ to $2\,\text{MK}$ or more. These observations permit spectroscopic diagnostics of plasma densities and temperatures in many solar features, and support studies of underlying physical processes. Specifically, SUMER observes over the broad wavelength range from 500 to $1610\,\text{Å}$ with spectral resolution $\sim 0.04\,\text{Å}$, angular resolution 1 arcsec (approximately $1000\,\text{km}$ in spatial extent on the Sun), and temporal resolution down to 1 s. It allows to measure profiles and intensities of EUV lines and to determine Doppler shifts and line broadening. The SUMER, telescope and spectrometer, has worked on the Solar and Heliospheric Observatory - SOHO (Domingo et al., 1995) since 1995.

The EUV Imaging Spectrometer - EIS (Culhane et al., 2007) on the Hinode satellite (Kosugi et al., 2007) observes the solar corona and the upper transition region emission lines with the wavelength ranges $170\text{-}210\,\text{Å}$ and $250\text{-}290\,\text{Å}$. The EIS contribution to the goals of the Hinode mission involves the measurements of line intensities, Doppler velocities, line widths, temperatures and densities for the plasma in the Sun's atmosphere. The spatial resolution of the instrument is 1 arcsec and the spectral resolution is $0.0223\,\text{Å}\,\text{px}^{-1}$. The telescope primary mirror images EUV radiation from the Sun onto the spectrograph slit. Light passing through the slit is dispersed and stigmatically re-imaged by the toroidal grating on two $1024\,\text{x}\,2048\,\text{pixel}$ CCD detectors, each with 2048 pixels in the dispersion direction. High-resolution spectroheliograms (raster images) are formed by moving the solar image across the spectrograph slit. An interchange mechanism allows selection among two slits (1 and 2 arcsec width) and two slots (40 and 266 arcsec width).

The Atmospheric Imaging Assembly - AIA (Lemen et al., 2012) with its four telescopes operates onboard Solar Dynamics Observatory - SDO (Pesnell et al., 2012). It is able to observe the Sun in ten different wavelengths nearly simultaneously. The AIA covers a large temperature range (60,000 K - 20 MK) from the photosphere to the corona by narrow-band imaging of seven EUV band passes centered on specific lines: Fe XVIII (94 Å), Fe VIII, XXI (131 Å), Fe IX (171 Å), Fe XII, XXIV (193 Å), Fe XIV (211 Å), He II (304 Å), Fe XVI (335 Å) and filters: C IV (1600 Å) and the nearby continuum (1700 Å). The solar full-disk images with 4096×4096 pixels and 1.5 arcsec spatial resolution are obtained at a cadence of 12 seconds in each filter. The AIA advanced our understanding of the mechanisms of solar variability and of how the Sun's energy is stored and released into the heliosphere and geospace.

Chapter 2

Non-Maxwellian κ-distributions

2.1 Observations and detections in space plasmas

The observations of space plasma during last four decades have demonstrated that non-Maxwellian distributions are ubiquitous in the solar wind, planetary magnetospheres, heliosphere and even in planetary nebulae, and could be present in the solar corona. The enhanced populations of particles at high energies can be usually described by characteristics power-law tails.

The first observations of the power-law suprathermal tails were carried out by Vasyliunas (1968) in the Earth's magnetosphere with OGO 1 and OGO 3 satellites. He also proposed an empirical function, called the κ-function, to simultaneously describe the low-energy, Maxwellian-like core and the high-energy power-law tail of the electron distribution. Feldman et al. (1975) tried to explain the observations of velocity distributions of electrons in the solar wind by superposition of two Maxwellian functions. The first Maxwellian function characterizes the low-energy electrons and the second one describes the distinct high-energy component. Pilipp et al. (1987) compared the electron distribution functions observed by the Helios 1 and 2 probes in the solar wind between 0.3 AU and 1 AU with the theoretical predictions. The most obvious differences of the analyzed electron distribution functions from the Maxwellian one were observed at energies above 50-100 eV.

The main progress in the exploring of the solar wind and detection of κ-distributions came with the Ulysses spacecraft (Wenzel et al., 1989). Maksimovic, Pierrard and Riley (1997) fitted 16 000 velocity distribution functions (hereafter VDFs) of electrons measured in the solar wind by the κ-distributions. The observed electron distributions has strong high-energy tails in the fast solar wind, but their shapes are closer to Maxwellian distribution in the slow solar

wind. According to these observations, Maksimovic, Pierrard and Lemaire (1997) presented a kinetic model of the solar wind based on the κ-distributions of the particle velocities escaping out of the coronal regions. They showed that κ-distribution gives a better approximation to the VDF than the sum of two isotropic Maxwellian VDFs presented by e.g. Feldman et al. (1975). Although both models are qualitatively comparable, the model using κ-distributions is more economic since it requires one parameter less (Fig. 2.1). The solar wind model with κ-distributions does also a better job in describing the high speed solar wind streams compared to the exospheric, purely collisionless models (e.g. Lemaire and Scherer, 1971) or hydrodynamic models (e.g. Sturrock and Hartle, 1966). The hydrodynamic models required unreasonably large coronal temperatures or additional heating of the outer regions of the corona to achieve the observed speed of solar wind. The kinetic model with κ-distributions departs from earlier models, gives the plasma parameters in agreement with the observed parameters at 1 AU and supports the results of kinetic theory that the suprathermal electrons influence the solar wind acceleration. Zouganelis et al. (2004) and Zouganelis et al. (2005) generalized models of the solar wind over a large range of coronal conditions. They also showed that a connection exists between the fast wind speed and coronal electron distribution with suprathermal tail.
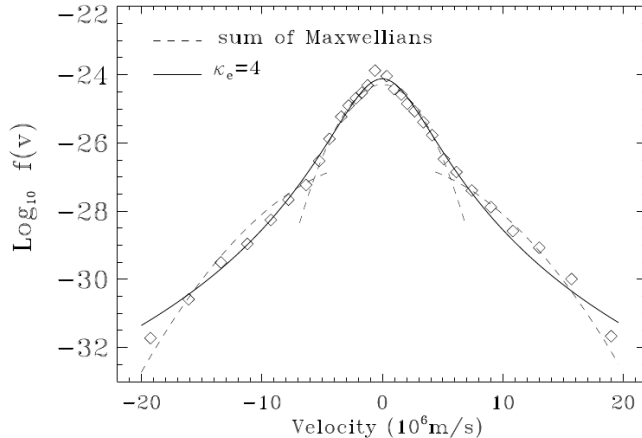
Figure 2.1: Electron VDF in the solar wind (diamonds) fitted by the dashed lines corresponding to the classical model made of the sum of two Maxwellian distributions: a core ($n_c = 30.8\,\mathrm{cm}^{-3}$ and $T_c = 1.6\,10^5\mathrm{K}$) and a halo ($n_h = 2.2\,cm^{-3}$ and $T_h = 8.9\,10^5 K$). The full line represents a κ-distribution with $\kappa_e = 4$, $n = 33.9\,\mathrm{cm}^{-3}$, and $T_\kappa = 1.9\,10^5\,\mathrm{K}$ (Maksimovic, Pierrard and Lemaire, 1997, Fig. 3).

Zouganelis (2008) fitted in situ electron velocity measurements by κ-distributions using the quasi-thermal noise spectroscopy method (Meyer-Vernet and Perche, 1989). citetzouganelis08 found parameter κ in the range $2-5$ for the Ulysses/URAP observations (Fig. 2.2). Le Chat et al. (2009) demonstrated that these observations using quasi-thermal noise spectroscopy are better fitted by κ-distribution function than by the sum of two Maxwellian distributions. Le Chat et al. (2011) diagnosed other parameters of the fast solar wind plasma - electron density and temperature as well.
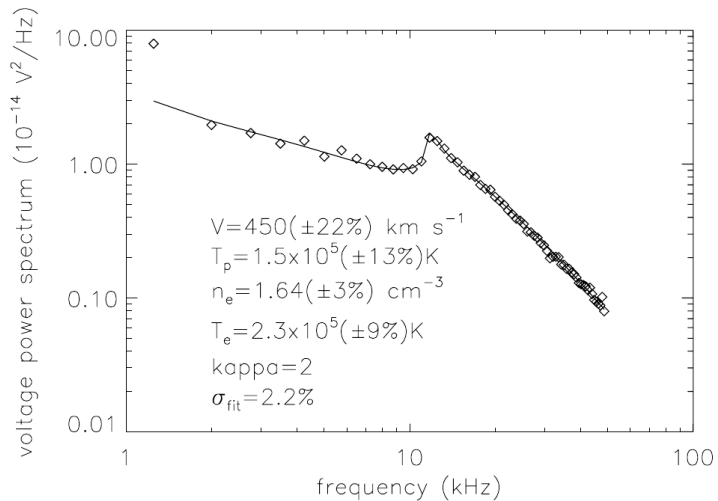
Figure 2.2: Typical voltage power spectrum measured with Ulysses/URAP and fitted with the parameters indicated (Zouganelis, 2008, Fig. 4a).

The measurements of the distribution functions of the Ne, O, and He ions by WIND spacecraft demonstrated that the high energy tails can also be fitted by κ-distributions (Collier et al., 1996). This type of distribution also provides a good fit to the observations of solar wind particle distributions recorded by the CLUSTER spacecraft (Qureshi et al., 2003). The measurements from VOYAGER indicate that ion distribution functions in the outer heliosphere are also well described by κ-distributions (e.g., Decker and Krimigis, 2003; Decker et al., 2005). Livadiotis et al. (2011) and Livadiotis and McComas (2012) analyzed the Interstellar Boundary Explorer (IBEX) spectra to estimate the κ values in the inner heliosheath.

The presence of the distributions with characteristic suprathermal tails were detected also in the magnetospheres of the planets. They were observed in the near-Earth plasma sheet (Gloeckler and Hamilton, 1987; Kletzing et al., 2003). Pierrard and Lemaire (1996) proposed model of ions in exosphere using κ-distribution. Xiao et al. (2008) modeled spectra of solar

energetic particles by κ-type distribution in the Earth's radiation belts. Collier and Hamilton (1995) applied κ-distributions on the energetic ion spectra at Jupiter, and Schippers et al. (2008) and Dialynas et al. (2009) found them in the ion spectra in the Saturnian magnetosphere.

Nicholls et al. (2012) studied the measurements of electron temperature and metallicity in an planetary nebulae by adopting the κ-distribution for the electron energies. They showed that even a small departure from an equilibrium distribution, κ-distribution with value κ=10, is able to explain the discrepancies which were not resolved for several decades. They argued that the κ-distributions offer an important new insight into the physics of gaseous nebulae, both in the Milky Way and elsewhere. Moreover, Zhang et al. (2014) explained the discrepancy in abundance in planetary nebulae using κ-distributions.

The observed shape of VDF in the solar wind is affected by non-Maxwellian distributions. But what is its origin? Do such distributions occur in the solar atmosphere or are they only a consequence of the solar wind transport in the interplanetary medium? Shoub (1983) was the first to show how the gradient in density and temperature affects electron VDF in collisional plasma in the solar transition region. His calculations of the VDF lead to the conclusion that the widely invoked assumption that in weakly inhomogeneous plasma the distribution function remains close to local Maxwellian distribution is incorrect. Scudder (1992) showed that the velocity filtration process can explain the existence of a hot stellar envelope. This process naturally produced non-Maxwellian κ-distributions in the transition region and corona with theoretical values of κ from 2.2 to 6.3. This values of κ are sufficient to cover radiative losses in the corona and produce solar wind speed at 1 AU between $300-600\,\mathrm{km\,s^{-1}}$. The non-Maxwellian distributions seem to be ubiquitous in the entire corona and solar wind (Scudder and Karimabadi, 2013).

Pierrard et al. (1999) used the kinetic model (by Maksimovic, Pierrard and Lemaire, 1997) of solar wind and the typical electron VDF observed at 1 AU by WIND spacecraft as a boundary condition to determine the electron VDF in the solar corona at $4\,R_\mathrm{S}$ using Fokker-Planck equations. They also considered that observed particles are affected by external forces and Coulomb collisions with a background plasma. Their results indicates that suprathermal tails must exist in the lower corona in order to be observed at 1 AU. The suprathermal tails are much less important close to the Sun than at larger distances. The distribution function of the background plasma coming from lower atmospheric layers does not remove suprathermal tails. Vocks and Mann (2003) demonstrated that the resonant interaction with whistler waves in the

solar corona can also significantly increase the flux of solar wind electrons in the keV range. The model calculations show that the quiet solar corona is capable of producing high-energy electrons.

There are only a few direct evidences of presence the κ-distributions in solar corona and transition region. Dufton et al. (1984) and Pinfield et al. (1999) showed that the observed intensity of Si III emission lines, and the 1313 Å line in particular, do not correspond to the Maxwellian distribution in the transition region. Following these results, Dzifčáková and Kulinová (2011) showed that the Si III spectra can be well described by the κ-distributions. They found that the deviation from the Maxwellian distribution increases with the magnetic activity. They diagnosed $\kappa = 13$ for coronal hole, $\kappa = 11$ for quiet sun, and $\kappa = 7$ for active region. Furthermore, these authors showed that the diagnostics is valid also for a plasma with a differential emission measure. This work provides the first spectroscopic evidence of κ-distributions in the solar transition region. Lee et al. (2013) studied the Fe XV line profiles and found that they are much better fitted with a κ-velocity distribution than a single Gaussian corresponding to the Maxwellian distribution.

Non-Maxwellian power-law tails are ubiquitous in the solar flare plasma, which contains accelerated particles (e.g. Brown, 1971; Holman et al., 2003). Fletcher et al. (2011) and Zharkova et al. (2011) offered the comprehensive reviews of solar flares and of particle acceleration processes during flares. Kašparová and Karlický (2009) showed that the X-ray emission of some sources in the solar corona during flares can also be described under the assumption of the κ-distributions. If non-Maxwellian distributions are indeed present, their influence on the interpretations of the observations has to be considered. As Dudík et al. (2009) showed, the κ-distributions significantly change the filter responses of the TRACE EUV filters. The κ-distributions also affect the shape of free-free and bound-free continuum (Dudík et al., 2012) and the radiative losses in the entire considered temperature range (Dudík et al., 2011b).

The changes in ionization, recombination, and excitation rates by the presence of κ-distributions allow its diagnostic from the solar spectra (Dzifčáková, 1992, 2002, 2006b; Dzifčáková and Mason, 2008; Dzifčáková and Dudík, 2013). Dzifčáková and Kulinová (2010) proposed the method for the diagnostics of the κ-distributions from Fe spectral lines observable by the Hinode/EIS and by Coronas-F/SPIRIT (Zhitnik et al., 2005) spectrometer. They used strong EUV lines of Fe in various degrees of ionization and analyzed sensitivity of their line ratios to the shape of the distribution function. The lines suitable for the diagnostics of κ-distribution were proposed
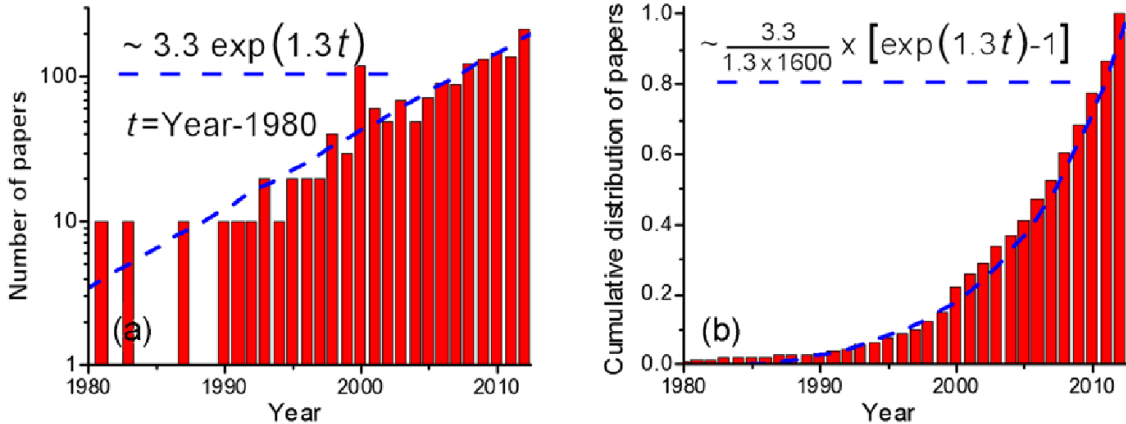
Figure 2.3: Number (*left*) and cumulative distribution (*right*) of N $\approx$ 1600 papers cataloged in Google Scholar from 1980 through 2012 that are related to κ-distributions and include these distributions in their title. The fit curve (blue dash) in both figures show the exponential growth of these studies (Livadiotis and McComas, 2013, Fig. 1)

and problems of diagnostics were discussed. Mackovjak et al. (2013) continued in investigation of the possibility to diagnose κ-distributions from EUV spectra with updated excitation and deexcitation rates corresponding to CHIANTI version 7 (Landi et al., 2012). They considered observable lines by Hinode/EIS of the most abundant elements except Fe. The influence of κ on the diagnostics of electron density was presented. The pairs of the line ratios suitable for the diagnostics of κ-distribution in the solar corona and upper transition region were listed (see Chapter 4). Although the κ-distributions were not instantly diagnosed, specialized observations became desirable to minimize the errors due to photon statistics (see Chapter 5). Dudík et al. (2014) investigated the diagnostics possibility from the IRIS spectra, showing that the Si IV and O IV ratios are a good indicator of departures from the Maxwellian distribution.

Leubner (2002) provided the missing link for power-law models of non-Maxwellian features from the fundamental physics. He showed that κ-distributions are a consequence of the entropy generalization in nonextensive Tsallis statistics (Tsallis, 1995), physically related to the long range nature of the Coulomb potential, turbulence and intermittency (Leubner and Vörös, 2005; Treumann and Jaroschek, 2008). Leubner (2002) also showed that the κ-distribution is equivalent to the q distribution function obtained from the maximization of the Tsallis entropy. Fundamental issues on κ-distributions in space plasmas and interplanetary proton distributions were emphasized in Leubner (2004). The relation of systems with long-range interactions

and correlations to non-Maxwellian distributions was shown in Leubner (2008). How the κ-distributions arise naturally from Tsallis statistical mechanics was examined also by Livadiotis and McComas (2009). In this work, definitions of temperature using various approaches were consulted. The authors showed that the temperature can be naturally generalized also for κ-distributions.

As we could see, since the observation of κ-distributions by Vasyliunas (1968), many scientific papers have been published to show the ability of κ-distributions to describe the space plasma (Fig. 2.3). The nice review on the occurrences and applications of the κ-distributions in the space plasma was provided also by Pierrard and Lazar (2010).

2.2 Properties of the κ-distributions

The κ-distribution of velocities is defined as (e.g., Maksimovic, Pierrard and Lemaire, 1997)

$$f(v, \kappa) = \frac{1}{2\pi(\kappa v_\kappa^2)^{3/2}} \frac{\Gamma(\kappa + 1)}{\Gamma(\kappa - 1/2)\Gamma(3/2)} \left(1 + \frac{v^2}{\kappa v_\kappa^2} \right)^{-(\kappa+1)} \tag{2.1}$$

where κ is a parameter of the distribution and v is velocity. Equivalent thermal speed is given by

$$v_\kappa = \left(\frac{(2\kappa - 3)}{\kappa} \frac{k_\mathrm{B}T}{m} \right)^{1/2}, \tag{2.2}$$

where k_B is the Boltzmann constant, m is particle mass and T is equivalent temperature. The distribution is normalized to unity. The velocity distributions with different κ are plotted in the Fig. 2.4 (*left*). The shape of the bulk is quite similar for each of distributions but the mean energy is different for each one.

The corresponding κ-distribution of particle energies E is given by the expression (e.g. Owocki and Scudder, 1983; Livadiotis and McComas, 2009)

$$f(E, \kappa)\mathrm{d}E = A_\kappa \frac{2}{\sqrt{\pi}(k_\mathrm{B}T)^{3/2}} \frac{E^{1/2}\mathrm{d}E}{\left(1 + \frac{E}{(\kappa - 3/2)k_\mathrm{B}T} \right)^{\kappa+1}}, \tag{2.3}$$

where A_κ is normalization constant

$$A_\kappa = \frac{\Gamma(\kappa + 1)}{\Gamma(\kappa - 1/2)(\kappa - 3/2)^{3/2}}. \tag{2.4}$$

The distribution is again normalized to unity. The parameter T is the temperature and κ is a free parameter which changes the shape of the distribution function from $\kappa \to 3/2$ corresponding to

the highest deviation from Maxwellian distribution, to $\kappa \to \infty$ which is a Maxwellian distribution

$$f(E)\mathrm{d}E = \frac{2}{\sqrt{\pi}(k_{\mathrm{B}}T_{\mathrm{th}})^{3/2}} \, e^{-\frac{E}{k_{\mathrm{B}}T_{\mathrm{th}}}} \, E^{1/2}\mathrm{d}E \,. \tag{2.5}$$

The mean energy $\langle E \rangle = 3k_{\mathrm{B}}T/2$ is the same for both Maxwellian and κ-distributions. Therefore, T can be also identified as the thermodynamic temperature $[T_{\mathrm{th}}]$ (Livadiotis and McComas, 2009). The κ-distributions with $\kappa = 2, 3, 5, 10$ and the Maxwellian distribution are plotted in Fig.2.4 (*right*) for $T = 10^{6.5}$ K. The mean energy of the particles is the same for each distribution.
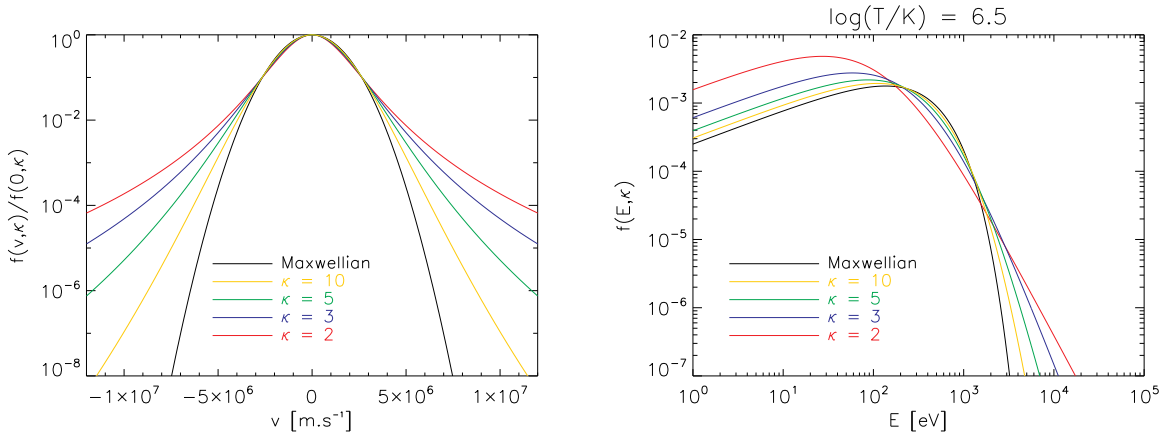
Figure 2.4: A comparison of the κ-distribution with $\kappa = 2, 3, 5, 10$ and the Maxwellian one. *Left*: The velocity distributions. *Right*: The energy distributions for the same $T = 10^{6.5}$ K and the mean energy.

The pressure for the κ-distribution can be expressed using the relation between the pressure and the mean energy of particles (Dzifčáková and Kulinová, 2010)

$$P = \frac{2}{3}\,n\langle E \rangle = nk_{\mathrm{B}}T \,, \tag{2.6}$$

where n is the particle density. This expression is the same as for the Maxwellian distribution. However, the most probable particle energy $[E_{\mathrm{p}}]$ is defined as

$$E_{\mathrm{p}} = \frac{\kappa - 1.5}{2\kappa + 1}\,k_{\mathrm{B}}T \,. \tag{2.7}$$

The E_{p} is equal to the most probable energy of the Maxwellian distribution if $\kappa \to \infty$. For $\kappa \to 3/2$, the most probable particle energy goes to zero. For $\kappa = 2$ we obtain $E_{\mathrm{p}} = k_{\mathrm{B}}T/10$. We note that $\kappa = 2$ is the strongest non-Maxwellian κ-distribution function that we use in our analysis in subsequent chapters.

Chapter 3

EUV spectroscopy of optically thin plasma for κ-distributions

3.1 Intensity of spectral line

Relatively high temperatures and low densities in the upper chromosphere, transition region and corona result in a spectrum with many emission lines and continuum in the UV $(1000\text{-}2000\,\text{Å})$, EUV $(100\text{-}1000\,\text{Å})$ and X-ray $(1\text{-}100\,\text{Å})$ ranges. For theoretical calculation of line intensity we assume that the upper solar atmosphere is optically thin. This assumption is usually fulfilled in the transition region and solar corona. All photons emitted along the line of sight eventually could reach the observer, due to the mean free path of photons in the upper solar atmosphere being greater than the length scale of the system. Therefore, the intensity of a spectral line is simply given by the sum of all contributions from the plasma along the line of sight. The spectral line emissivity, i.e. the energy emitted per unit volume in a spectral line formed by the transition from atomic level j to i in the ion $X_j^{+\mathrm{m}}$ can be written as (e.g., Phillips et al., 2008):

$$\varepsilon_{ji} = N(X_j^{+m})A_{ji}h\nu_{ji} \qquad [\mathrm{erg\,s^{-1}\,cm^{-3}}], \qquad (3.1)$$

where ν_{ji} is the photon frequency $(\nu_{ji} = c/\lambda_{ji})$ corresponding to the energy of the transition, h is the Planck constant, A_{ji} is the Einstein's coefficient of the probability for the spontaneous emission, and $N(X_j^{+m})$ is the density of the m-times ionized ion of the element X with the electron on the excited upper level j. The intensity I_{ji} of a spectral line along the line of sight

l is then defined as

$$I_{ji} = \frac{1}{4\pi} \int_l N(X_j^{+m}) A_{ji} h\nu_{ij} \, dl \qquad [\mathrm{erg\, cm^{-2}\, s^{-1}\, sr^{-1}}]. \tag{3.2}$$
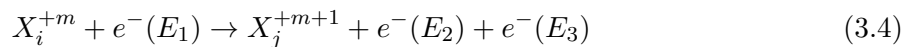
The density of emitters can be expressed as a function of the electron density using the relation

$$N(X_j^{+m}) = \frac{N(X_j^{+m})}{N(X^{+m})} \frac{N(X^{+m})}{N(X)} \frac{N(X)}{N(H)} \frac{N(H)}{N_e} N_e, \tag{3.3}$$
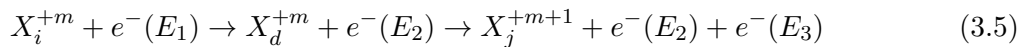
where $N(X_j^{+m})\,/\,N(X^{+m})$ is the relative level population, $N(X^{+m})\,/\,N(X)$ is the relative ion population, $N(X)\,/\,N(H)$ is the abundance of the element X relative to hydrogen, and $N(H)\,/\,N_e$ is the abundance of hydrogen relative to the electron density.

3.2   Ionization and excitation equilibrium
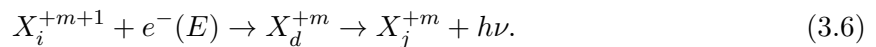
Plasma in the coronal conditions has relatively low density and small number of collisions. Therefore, the direct electron ionization, auto-ionization, radiative and dielectronic recombination must be taken into account to calculate the ionization equilibrium and the relative ion population. The direct electron ionization occurs by interaction of the m-times ionized ion, X_i^{+m}, with an electron, e^-, that has a sufficient energy for its ionization

$$X_i^{+m} + e^-(E_1) \rightarrow X_j^{+m+1} + e^-(E_2) + e^-(E_3) \tag{3.4}$$
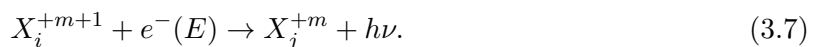
and produces ion in the higher ionization state X_j^{+m+1}. An ion in a doubly excited state, X_d^{+m} can undergo spontaneous auto-ionization

$$X_i^{+m} + e^-(E_1) \rightarrow X_d^{+m} + e^-(E_2) \rightarrow X_j^{+m+1} + e^-(E_2) + e^-(E_3) \tag{3.5}$$

to give an ion and a free electron. The dielectronic recombination also involve a doubly excited state

$$X_i^{+m+1} + e^-(E) \rightarrow X_d^{+m} \rightarrow X_j^{+m} + h\nu. \tag{3.6}$$

In the radiative recombination, a free electron is captured by an ion into one of its available energy states and the excess energy is removed by emission of a photon

$$X_i^{+m+1} + e^-(E) \rightarrow X_j^{+m} + h\nu. \tag{3.7}$$

The rates of each process can be written as

$$R = <\sigma v> = \int_0^\infty \sigma \left(\frac{2E}{m_e}\right)^{1/2} f(E)\mathrm{d}E \tag{3.8}$$

where $E = m_e v^2/2$. They depend on the type of the electron distribution function $f(E)$ and can be calculated for known cross sections $\sigma(E)$. The ionization equilibrium in the solar corona can be then expressed as

$$\frac{N_i}{N_{i+1}} = \frac{R_{i+1}}{C_i} \tag{3.9}$$

where N_i and N_{i+1} are the concentrations of i-times and $i+1$-times respectively ionized ion, the ionization rate C_i from state i to $i+1$ is the sum of direct ionization rate R_{DI} and auto-ionization rate R_{AI}, $C_i = R_{\mathrm{DI}} + R_{\mathrm{AI}}$, and recombination rate R_{i+1} from state $i + 1$ to i is a sum of the dielectronic α_{DR} and radiative R_{RR} recombination rate, $R_{i+1} = \alpha_{\mathrm{DR}} + R_{\mathrm{RR}}$. The ionization and recombination rates, and the ionization equilibrium for the Maxwellian distribution have been calculated by e.g., Mazzotta et al. (1998); Badnell et al. (2003); Dere (2007); Dere et al. (2009).
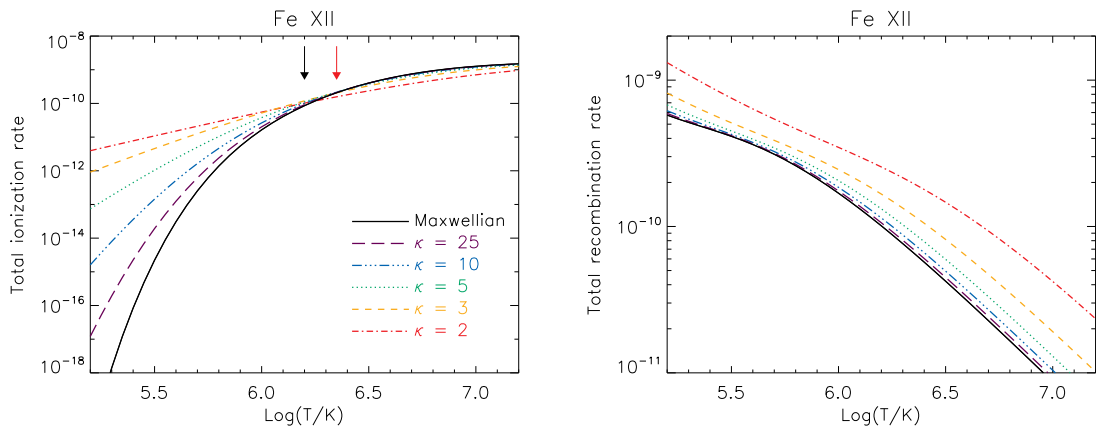
Figure 3.1: Total ionization (*left*) and recombination (*right*) rates for Fe XII. The values of κ are indicated. Black and red arrows denote maximum of the ion abundance for the Maxwellian and κ-distribution with $\kappa = 2$. (Dzifčáková and Dudík, 2013, Fig. 2).

The effect of the κ-distributions on the ionization and recombination rates and on the ionization equilibrium has been calculated by Dzifčáková (1992, 2002)), Wannawichian et al. (2003), and Dzifčáková and Dudík (2013). The presence of the high-energy electrons enhances the ionization rates for the κ-distributions (Fig. 3.1, *left*) in the comparison with the Maxwellian one. The enhancement depends on the value of κ and the ratio of the ionization energy to temperature. The rate of the radiative recombination decreases with temperature as result its relation to the number of the low-energy electrons. The κ-distributions contain more low energy electrons in comparison with Maxwellian distribution at the same temperature (Fig. 2.4, *right*).
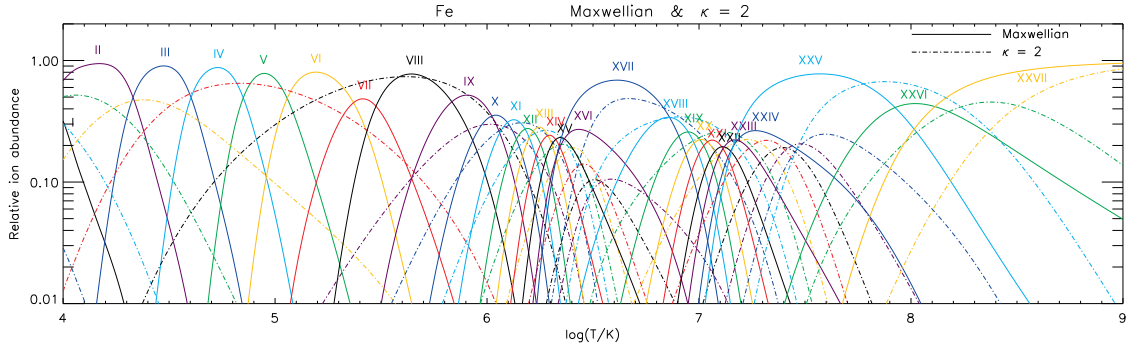
Figure 3.2: The ionization equilibrium for Maxwellian distribution (solid lines) and for κ-distribution with $\kappa = 2$ (dot dashed lines) for Fe. Individual ionization stages are indicated (Dzifčáková and Dudík, 2013, Fig. 3).

The result is that the radiative recombination rates for the κ-distributions increase with a decrease of the parameter κ (Fig. 3.1, *right*). The effect of the κ-distributions on the dielectronic recombination rates is not such straightforward as for the other processes (Fig. 3.1, *right*). The dielectronic recombination rates depend on the number of particles in distribution with energies that correspond to the stabilization photon transitions (Eq. 3.6). The changes in the ionization and recombination rates are reflected in significant changes in the ionization equilibrium. The ionization peaks are wider and flatter and they can also be shifted to higher or lower temperatures. The highest differences are in comparison of ionization peaks for Maxwellian and κ=2 distribution (Fig. 3.2). We note, that consequences of changes in ionization equilibrium for κ-distributions are used in our analysis (chapters 4 - 6).

The relative level population could be determined by solving the excitation equilibrium equations for a number of low-lying levels of the ion including all the important collisional and radiative excitation and de-excitation mechanisms. The collisional excitation occurs by collision of an atom X_i with a free electron e^-

$$X_i + e^-(E_1) \rightarrow X_j + e^-(E_2). \tag{3.10}$$

The kinetic energy from the collision is transferred to one of the atom's bound electrons and it jumps from a lower i to higher j energy state. The atom can by also exited by photon in the process of photo-excitation

$$X_i + h\nu \rightarrow X_j. \tag{3.11}$$

In the process of collisional de-excitation

$$X_j + e^-(E_1) \rightarrow X_i + e^-(E_2) \tag{3.12}$$

and radiative de-excitation

$$X_j \rightarrow X_i + h\nu \tag{3.13}$$

bound electron loses its energy and falls back to the lower energy state. The electron excitation and radiative de-excitation usually dominate in the coronal conditions. The statistical equilibrium equation for calculation of the level populations is defined as:

$$\sum_{i \neq j}^{k} N_i P_{ij} = \sum_{j \neq i}^{k} N_j P_{ji} \,, \tag{3.14}$$

where N_i is the density of ions with excited level i and the number of energetic levels of the considered ion is k. $N_i P_{ij}$ is the number of population transfers from level i to level j and $N_j P_{ji}$ is the number of the population transfers from level j to level i. The probability of transition $i \rightarrow j$ can be expressed as $P_{ij} = C_{ij} + A_{ji} + B_{ij} I_\nu$. C_{ij} is sum probabilities for all collisional transitions and depends on the density of colliding particles, their energy distribution, cross sections and excitaion energy of transition. The last two components correspod to the radiative transitions where A_{ji} and B_{ij} are Einstein coefficients for the spontaneous and absorption/stimulated emission and I_ν is the radiation field. Since the coronal plasma is optically thin, the absorption and stimulated emission can be usually neglected. Therefore, $P_{ij} = C_{ij} + A_{ji}$. Note, that the accuracy of the calculation of the level populations also depends on the number of considered energetic levels.

The excitation and de-excitation rates can be obtained by integrating of the appropriate cross-sections. Unfortunately, databases usually contain only Maxwellian averaged excitation and de-excitation rates. For unavailable cross-sections, the method described in Dzifčáková (2006a,b) and tested in Dzifčáková and Mason (2008) can be used for the calculation of the electron excitation rates for the κ-distributions. The presence of κ-distributions increases the electron excitation rates for high ratios of the excitation energies to temperature. If the excitation energy increases for low temperature than the enhancement of the electron excitation rates for κ-distributions also increases and can be several order higher than for Maxwellian distribution (Fig. 3.3). These effects have been studied by Dzifčáková and Tóthová (2007); Dzifčáková and Kulinová (2011).
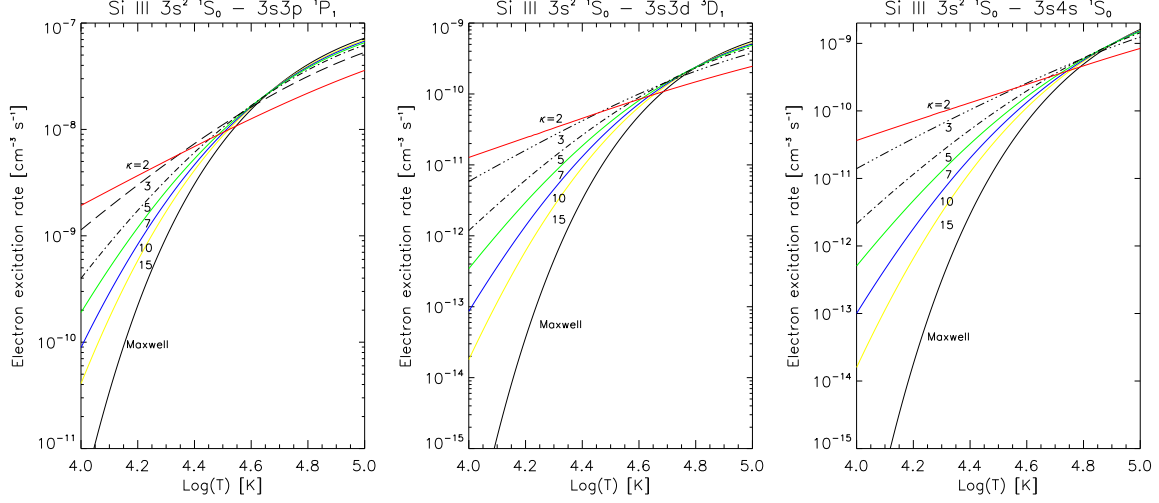
Figure 3.3: Dependence of the electron excitation rates on T for the κ-distributions with $\kappa = \dot{2}$, 3, 5, 7, 10, 15 and for Maxwellian distribution. Figures are plotted for three different transition with different excitation energies (Dzifčáková and Kulinová, 2011, Fig. 4)

.

3.3 Contribution function and emission measure

The contribution function $G_{ji}(T, N_e, \kappa)$ as a function of temperature, electron density and value of κ-distribution is defined as (e.g., Phillips et al., 2008)

$$G_{ji}(T, N_e, \kappa) = \frac{N(X_j^{+m})}{N(X^{+m})} \frac{N(X^{+m})}{N(X)} \frac{N(X)}{N(H)} \frac{N(H)}{N_e} \frac{A_{ji}}{N_e} h\nu_{ji}, \qquad (3.15)$$

and using Eq. 3.2 the intensity of the spectral line can be written as

$$I_{ji} = \frac{1}{4\pi} \int_l G_{ji}(T, N_e, \kappa) N_e^2 \, dl. \qquad (3.16)$$

The emission measure (EM) along the line of sight is defined as a quantity $N_e^2 dl = d(EM)$, and has units of [cm^{-5}]. It depends on the number of free electrons ($N_e dl$) and on the electron density (N_e) along the line of sight, and therefore on the physical conditions of the emitting plasma. The total emission measure EM of the plasma is given by

$$EM = \int_V N_e^2 dl. \qquad (3.17)$$

In the most cases, the plasma along the light of sight does not have constant temperature and density. It can be divided into several intervals dl where the temperature and density lie

in the $T + dT$ and $N_e + dN_e$ ranges. Therefore, Eq. (3.16) can be rewritten as an integral over T and N_e:

$$I_{ji} = \frac{1}{4\pi} \iint G_{ji}(T, N_e, \kappa)\psi(T, N_e) \, dT \, dN_e, \qquad (3.18)$$

where the $\psi(T, N_e)$ is the emission measure differential. It can be considered to be a measure of the emission from the plasmas as a function of T and N_e. Note that we do not consider here the possible dependence of ψ on κ for the reason of simplicity. Since the sensitivity of the contribution function $G_{ji}(T, N_e, \kappa)$ to N_e is usually weak compared to its sensitivity to T, the quantity $\psi(T, N_e)$ is typically reduced to the emission measure differential in temperature, $DEM(T)$, also called the differential emission measure (DEM):

$$DEM(T) = N_e^2 \frac{dl}{dT} \qquad [\mathrm{cm^{-5}K^{-1}}]. \qquad (3.19)$$

Using Eqs. (3.16) and (3.19), the observed line intensity can be written as

$$I_{ji} = \frac{1}{4\pi} \int_T G_{ji}(T, N_e, \kappa) DEM(T) \, dT. \qquad (3.20)$$

The inversion of equation 3.20 provides $DEM(T)$ for temperature range from observed intensities and calculated contribution functions. Such inversion poses several problems. Therefore, many techniques have been developed to carry it out (see Chapter 6.1).

Finally, the line intensities and contribution functions $G_{ji}(T, N_e, \kappa)$ can be calculated for the Maxwellian distribution by the CHIANTI software and database, and for the κ-distributions by the modification of CHIANTI (Dzifčáková, 2006a,b). CHIANTI is the unique atomic database and software that aims to include calculations of the optically thin spectrum of astrophysics objects and carry out spectroscopic plasma diagnostics. The database includes atomic energy levels, wavelengths, radiative transition probabilities, collision excitation rate coefficients, and ionization and recombination rate coefficients, as well as data to calculate free-free, free-bound, and two-photon continuum emission. Thus, CHIANTI database fulfill its basic goal and it is the database that includes the best available calculations of atomic parameters for analyzing astrophysical emission line spectra (Dere et al., 1997; Landi et al., 2012). The atomic database and a suite of computer programs are continuously improved and updated. Version 7.1 is to date the most recent release (Landi et al., 2013). The modification of CHIANTI for the κ-distributions has extended database that contains approximations of the cross-sections for all atomic transitions which are originally included in CHIANTI 7.1 version and special software for the calculation of the line intensities and synthetic spectra for the κ-distributions (provided by Dzifčáková, 2014, private communication).

CHIANTI software and its modification are written in the Interactive Data Language (IDL), that is the environment for processing of large amounts of data. All data in our PhD thesis were also analyzed in IDL and SolarSoftWare (SSW). SSW is a set of integrated software libraries, databases and system utilities that provide a programing and data analysis tools for the solar physics (Freeland and Handy, 1998).

Chapter 4

Diagnostics of κ-distributions

4.1 Method

The method of κ-distributions diagnostics from the coronal and transition region spectral line intensities were developed by Dzifčáková and Kulinová (2010) and Mackovjak et al. (2013). We introduce this method with applying of observed data by Brown et al. (2008) in this chapter.

The shape of the distribution function affects the ionization, recombination, and excitation rates. This is because the rates of individual processes are an integral of the product of the corresponding cross-section with the distribution function (see Chap 3). We used the modification of CHIANTI (Dzifčáková, 2006b) with the ionization balances of Dzifčáková (2002) and with updated database for calculation of the excitation and deexcitation rates corresponding to CHIANTI version 7 (Landi et al., 2012), in this chapter. Generally, the line intensities and intensity ratios depend on three parameters: T, n_{e} and κ. If n_{e} is known, the value of κ can be determined from the observations using ratios of line intensities, if the lines involved differ either in the excitation energy, or in the behavior of the excitation cross-section with E, or if they belong to different ions. Otherwise, changes in line intensities due to κ cannot be separated from the changes due to temperature, which is also a parameter of the distribution function.

Dzifčáková and Kulinová (2010) proposed a method to diagnose the κ-distributions using Fe lines observed by EIS. The method is based on the ratio-ratio diagrams, $i.e.$, dependence of one ratio of line intensities to the other one for different plasma parameters. This allows for simultaneous diagnostics of two parameters, T and κ, if the changes due to T and κ can be separated. This is often not the case of the Fe lines observed by Hinode/EIS.

In addition, line ratios also depend on the electron density. Thus, proper determination of

κ from observations requires either an a priori determination of n_{e}, or they must be density-independent. To determine n_{e} a priori, the ratios used for diagnostics of n_{e} cannot be strongly dependent on κ. The dependence of these density-sensitive ratios on T increases the error in determination in n_{e}, so that the best available ratios offer precision of about 0.1 dex in the determination of n_{e}.

We analyzed the possibility of diagnosing the κ-distributions together with T and n_{e} from the lines of Al, Ar, Ca, Mg, Ni, O, S, and Si observable by the Hinode/EIS instrument. We employed the line ratio analysis similar to that of Dzifčáková and Kulinová (2010). We used only lines that have sufficient observed intensities and are not heavily blended. The investigated lines are listed in Table 4.1. The blends (bl) and self-blends (sbl) are indicated. The presented lines are formed in wide ranges of temperatures and densities corresponding to the transition region and coronal conditions. We calculated the synthetic intensities of these lines for $\log(T[\mathrm{K}]) = 5.0 - 7.5$, $\log(n_e[\mathrm{cm}^{-3}]) = 8 - 12$ and κ-distributions with $\kappa = 2$, 3, 5, and 10 together with the Maxwellian distribution. Then we searched for line ratios suitable for diagnostics of n_{e} (Chapter 4.2) and subsequently for line ratios suitable for simultaneous diagnostics of T and κ (Chapter 4.3).

To test the proposed diagnostics based on ratios of synthetic intensities, we compare these with the observations reported by Brown et al. (2008). These authors provide a spectral atlas of lines observed in various regions of the solar atmosphere. The observed features include a quiet Sun (QS) region, two active regions on the solar disk (AR1, AR2), and an active region on the limb, where the EIS slit was located right on the limb (L), and $20''$ above the limb (L+20). The exposure times were 60 s for the L and L+20 regions, and 600 s for the QS and both AR1 and AR2. We estimate the error of these observations as a combination of the calibration error, which is about 10% based on the in-flight calibration of EIS Wang et al. (2011), and the errors due to the photon statistics.

We note that the diagnostics proposed in this chapter should be used only for homogenous plasma characterized by a single temperature and single density. These conditions are fulfilled *e.g.* in the single-strand structures. We do not consider the effect of DEM on the diagnostics.

Table 4.1: The list of the investigated lines. Known blends (bl) and self-blends (sbl) are indicated.

Ion	$\lambda\,[\text{Å}]$	Transition	Notes
Al v	278.70	$2s^2\,2p^5\,{}^2P_{3/2}$ - $2s\,2p^6\,{}^2S_{1/2}$	bl Fe xiv
Al viii	250.14	$2p^2\,{}^3P_2$ - $2s\,2p^3\,{}^3S_1$	
Al viii	251.36*	$2p^2\,{}^1D_2$ - $2s\,2p^3\,{}^1P_1$	
Al ix	282.42	$2s^2\,2p\,{}^2P_{1/2}$ - $2s\,2p^2\,{}^2P_{1/2}$	
Ar xiv	191.40	$2s^2\,2p\,{}^2P_{3/2}$ - $2s\,2p^2\,{}^2P_{1/2}$	
Ar xiv	194.40	$2s^2\,2p\,{}^2P_{1/2}$ - $2s\,2p^2\,{}^2S_{1/2}$	
Ca xiv	183.46	$2s^2\,2p^3\,{}^4S_{3/2}$ - $2s\,2p^4\,{}^4P_{1/2}$	bl Ar xiv
Ca xiv	186.61*	$2s^2\,2p^3\,{}^4S_{3/2}$ - $2s\,2p^4\,{}^4P_{3/2}$	bl Fe viii
Ca xiv	193.87	$2s^2\,2p^3\,{}^4S_{3/2}$ - $2s\,2p^4\,{}^4P_{5/2}$	
Ca xv	176.93*	$2s^2\,2p^2\,{}^3P_1$ - $2s\,2p^3\,{}^3P_1$	
Ca xv	181.90*	$2s^2\,2p^2\,{}^3P_2$ - $2s\,2p^3\,{}^3P_2$	
Ca xv	182.87	$2s^2\,2p^2\,{}^3P_2$ - $2s\,2p^3\,{}^3P_1$	
Ca xv	200.97	$2s^2\,2p^2\,{}^3P_0$ - $2s\,2p^3\,{}^3D_1$	
Ca xv	208.32	$2s^2\,2p^2\,{}^3P_1$ - $2s\,2p^3\,{}^3D_1$	bl Fe xii
Ca xvi	208.60*	$2s^2\,2p\,{}^2P_{1/2}$ - $2s\,2p^2\,{}^2D_{3/2}$	
Ca xvii	192.85*	$2s^2\,{}^1S_0$ - $2s\,2p\,{}^1P_1$	bl Fe xi
Ca xvii	199.56*	$2s\,2p\,{}^3P_2$ - $2p^2\,{}^1D_2$	bl Fe ix
Mg v	276.58	$2s^2\,2p^4\,{}^1D_2$ - $2s\,2p^5\,{}^1P_1$	
Mg vi	268.99	$2s^2\,2p^3\,{}^2D_{3/2}$ - $2s\,2p^4\,{}^2P_{1/2}$	
Mg vi	270.39	$2s^2\,2p^3\,{}^2D_{5/2}$ - $2s\,2p^4\,{}^2P_{3/2}$	
Mg vii	276.15	$2s^2\,2p^2\,{}^3P_0$ - $2s\,2p^3\,{}^3S_1$	bl Fe xi
Mg vii	277.00*	$2s^2\,2p^2\,{}^3P_1$ - $2s\,2p^3\,{}^3S_1$	bl Si viii
Mg vii	278.40	$2s^2\,2p^2\,{}^3P_2$ - $2s\,2p^3\,{}^3S_1$	bl Ni xv
Mg vii	280.74	$2s^2\,2p^2\,{}^1D_2$ - $2s\,2p^3\,{}^1P_1$	bl Fe xiv
Ni xv	189.24	$3s^2\,3p^2\,{}^3P_2$ - $3s^2\,3p\,3d\,{}^3P_2$	
Ni xv	195.52	$3s^2\,3p^2\,{}^1D_2$ - $3s^2\,3p\,3d\,{}^1D_2$	
Ni xvi	185.23*	$3s^2\,3p\,{}^2P_{1/2}$ - $3s^2\,3d\,{}^2D_{3/2}$	bl Fe viii
Ni xvi	194.05	$3s^2\,3p\,{}^2P_{3/2}$ - $3s^2\,3d\,{}^2D_{5/2}$	
Ni xvi	195.27*	$3s^2\,3p\,{}^2P_{3/2}$ - $3s^2\,3d\,{}^2D_{3/2}$	bl Fe xiv
Ni xvi	288.17	$3s^2\,3p\,{}^2P_{1/2}$ - $3s\,3p^2\,{}^2D_{3/2}$	
Ni xvii	249.19	$3s^2\,{}^1S_0$ - $3s\,3p\,{}^1P_1$	

Table 4.1: Continued.

Ion	λ [Å]	Transition	Notes
O IV	182.71*	$2s^2\,2p\,^2P_{1/2}$ - $2s\,2p\,(1P)\,3p\,^2D_{3/2}$	
O IV	202.89	$2s^2\,2p\,^2P_{1/2}$ - $2s\,2p\,(3P)\,3p\,^2S_{1/2}$	bl Ni XV
O IV	203.04	$2s^2\,2p\,^2P_{3/2}$ - $2s\,2p\,(3P)\,3p\,^2S_{1/2}$	
O IV	207.18	$2s^2\,2p\,^2P_{1/2}$ - $2s\,2p\,(3P)\,3p\,^2D_{3/2}$	sbl
O IV	207.23	$2s^2\,2p\,^2P_{3/2}$ - $2s\,2p\,(3P)\,3p\,^2D_{5/2}$	sbl
O IV	208.91*	$2s^2\,2p\,^2P_{3/2}$ - $2s\,2p\,(3P)\,3p\,^4P_{5/2}$	bl Ne VI
O IV	208.96*	$2s^2\,2p\,^2P_{3/2}$ - $2s\,2p\,(3P)\,3p\,^4P_{3/2}$	bl S VIII
O IV	253.08*	$2s\,2p^2\,^2P_{3/2}$ - $2s\,2p\,(1P)\,3d\,^2D_{5/2}$	sbl
O IV	253.10*	$2s\,2p^2\,^2P_{3/2}$ - $2s\,2p\,(1P)\,3d\,^2D_{3/2}$	sbl
O IV	271.57*	$2s\,2p^2\,^2D_{5/2}$ - $2s\,2p\,(3P)\,3d\,^4F_{3/2}$	sbl
O IV	271.58*	$2s\,2p^2\,^2D_{3/2}$ - $2s\,2p\,(3P)\,3d\,^4F_{3/2}$	sbl
O IV	272.27*	$2s\,2p^2\,^4P_{3/2}$ - $2s\,2p\,(3P)\,3s\,^4P_{1/2}$	sbl
O IV	272.31*	$2s\,2p^2\,^4P_{5/2}$ - $2s\,2p\,(3P)\,3s\,^4P_{3/2}$	sbl
O IV	279.63	$2s^2\,2p\,^2P_{1/2}$ - $2s^2\,3s\,^2S_{1/2}$	
O IV	279.93	$2s^2\,2p\,^2P_{3/2}$ - $2s^2\,3s\,^2S_{1/2}$	
O V	172.17*	$2s^2\,^1S_0$ - $2s\,3p\,^1P_1$	bl Ni XIV
O V	192.90*	$2s\,2p\,^3P_2$ - $2s\,3d\,^3D_3$	bl Fe XI
O V	248.46	$2s\,2p\,^1P_1$ - $2s\,3s\,^1S_0$	bl Al VIII
O V	270.84*	$2p^2\,^3P_1$ - $2s\,3p\,^3P_1$	sbl
O V	270.87*	$2p^2\,^3P_1$ - $2s\,3p\,^3P_0$	sbl
O V	271.04*	$2p^2\,^3P_2$ - $2s\,3p\,^3P_1$	
O VI	183.94	$1s^2\,2p\,^2P_{1/2}$ - $1s^2\,3s\,^2S_{1/2}$	bl Ni XIV
O VI	184.12	$1s^2\,2p\,^2P_{3/2}$ - $1s^2\,3s\,^2S_{1/2}$	
Si VI	246.01	$2s^2\,2p^5\,^2P_{3/2}$ - $2s\,2p^6\,^2S_{1/2}$	
Si VI	249.12*	$2s^2\,2p^5\,^2P_{1/2}$ - $2s\,2p^6\,^2S_{1/2}$	
Si VII	272.64	$2s^2\,2p^4\,^3P_2$ - $2s\,2p^5\,^3P_1$	
Si VII	275.35	$2s^2\,2p^4\,^3P_2$ - $2s\,2p^5\,^3P_2$	
Si VII	275.67	$2s^2\,2p^4\,^3P_1$ - $2s\,2p^5\,^3P_1$	
Si VIII	250.47	$2s^2\,2p^3\,^2P_{1/2}$ - $2s\,2p^4\,^2S_{1/2}$	
Si VIII	250.81	$2s^2\,2p^3\,^2P_{3/2}$ - $2s\,2p^4\,^2S_{1/2}$	

Table 4.1: Continued.

Ion	$\lambda\,[\text{Å}]$	Transition	Notes
Si X	253.79	$2s^2\,2p\,^2P_{1/2}$ - $2s\,2p^2\,^2P_{3/2}$	
Si X	258.37	$2s^2\,2p\,^2P_{3/2}$ - $2s\,2p^2\,^2P_{3/2}$	
Si X	261.06	$2s^2\,2p\,^2P_{3/2}$ - $2s\,2p^2\,^2P_{1/2}$	
Si X	271.99*	$2s^2\,2p\,^2P_{1/2}$ - $2s\,2p^2\,^2S_{1/2}$	
Si X	277.26	$2s^2\,2p\,^2P_{3/2}$ - $2s\,2p^2\,^2S_{1/2}$	
S X	180.73	$2s^2\,2p^3\,^2D_{5/2}$ - $2s\,2p^4\,^2P_{3/2}$	
S X	196.11	$2s^2\,2p^3\,^2P_{1/2}$ - $2s\,2p^4\,^2P_{3/2}$	
S X	196.81	$2s^2\,2p^3\,^2P_{3/2}$ - $2s\,2p^4\,^2P_{3/2}$	
S X	257.15	$2s^2\,2p^3\,^4S_{3/2}$ - $2s\,2p^4\,^4P_{1/2}$	*bl* Fe XV
S X	259.50*	$2s^2\,2p^3\,^4S_{3/2}$ - $2s\,2p^4\,^4P_{3/2}$	*bl* Fe XII
S X	264.23	$2s^2\,2p^3\,^4S_{3/2}$ - $2s\,2p^4\,^4P_{5/2}$	
S XI	188.67	$2s^2\,2p^2\,^3P_1$ - $2s\,2p^3\,^3S_1$	*bl* Fe IX
S XI	190.36	$2s^2\,2p^2\,^1D_2$ - $2s\,2p^3\,^1P_1$	
S XI	191.27	$2s^2\,2p^2\,^3P_2$ - $2s\,2p^3\,^3S_1$	*bl* Fe IX
S XI	246.89	$2s^2\,2p^2\,^3P_2$ - $2s\,2p^3\,^3P_2$	
S XI	281.40	$2s^2\,2p^2\,^3P_0$ - $2s\,2p^3\,^3D_1$	
S XI	285.59	$2s^2\,2p^2\,^3P_1$ - $2s\,2p^3\,^3D_1$	
S XI	285.82	$2s^2\,2p^2\,^3P_1$ - $2s\,2p^3\,^3D_2$	*sbl*
S XI	285.85	$2s^2\,2p^2\,^1D_2$ - $2s\,2p^3\,^3P_1$	*sbl*

* These lines cannot be observed for exposure times shorter than $60\,\text{s}$.

4.2 Density Diagnostics

The diagnostics of the electron density is usually required prior to the simultaneous diagnostics of T and κ. We prefer to evaluate the electron density from lines of ions which can also be used for diagnostics of T and κ. Young (2007) and Young et al. (2007, 2009) proposed several line ratios belonging to Ar, Fe, Ni, S, and Si suitable to determine n_e (Table 4.2). We note that CHIANTI version 7 shows that some of these lines are blended. The known blends and self-blends are indicated in Table 4.2. Unfortunately, some of the blends have non-negligible intensities and cannot be removed using branching ratios. Our analysis involving lines from Table 4.1 did not reveal any additional ratios without blends applicable for the density diagnostics.

Table 4.2: The line ratios of Ar, Ni, S, Si, and Fe suitable for the diagnostics of the electron density.

Ion	Ratio	$\log(T_{\max}[\mathrm{K}])$		Density range
		Maxwell	$\kappa = 2$	$\log(n_{\mathrm{e}}[\mathrm{cm}^{-3}])$
Si x	261.06 / 258.37	6.15	6.20	$8 - 9.5$
S x	196.81 / 264.23	6.15	6.20	$10 - 12$
Fe xii	$(186.85 + 186.88)\,(bl\ \mathrm{S\,xi})/(195.12 + 195.18)$	6.15	6.25	$8 - 11.5$
Fe xiii	196.53 / 202.04	6.20	6.30	$9 - 11$
Fe xiii	$(203.82 + 203.83) / 202.04$	6.20	6.30	$8.5 - 10.5$
S xi	190.36 / 191.27 $(bl^{\star}\ \mathrm{Fe\,ix})$	6.25	6.30	$10 - 12$
S xi	$(285.82 + 285.85) / 281.40$	6.25	6.35	$8 - 10$
Fe xiv	264.78 $(bl\ \mathrm{Fe\,xi}) / 274.20\ (bl\ \mathrm{Si\,vii})$	6.30	6.45	$8.5 - 11$
Ni xvi	194.05 / 185.23 $(bl^{\star}\ \mathrm{Fe\,viii})$	6.40	6.60	$9.5 - 11.5$
Ar xiv	191.40 / 194.40	6.50	6.70	$10.5 - 12$

* These blends cannot be removed

Usually, these line ratios can be used for the electron density diagnosing in a limited range of densities only. For instance, the ratio S xi 285.80 Å / 281.40 Å can be used for $\log(n_{\mathrm{e}}[\mathrm{cm}^{-3}]) = 8 - 10$ only and the ratio Ni xvi 194.05 Å / 185.23 Å for $\log(n_{\mathrm{e}}[\mathrm{cm}^{-3}]) = 9.5 - 11.5$, *i.e.*, for flare densities. The electron density ranges for the considered ratios are summarized in Table 4.2. This table also lists the peak formation temperatures of these lines for the Maxwellian and κ-distribution with $\kappa = 2$.

The line ratios used for density diagnostics are also influenced by T and the electron distribution (Figures 4.1 and 4.2), as noted already for the Fe ratios by Dzifčáková and Kulinová (2010). The sensitivity to T and κ of the line ratios usable for density diagnostics is shown in Figure 4.1 (left column) for S lines and in Figure 4.2 (left column) for Si, Ni, and Ar lines. To capture the influence of T on these ratios, Figures 4.1 and 4.2 (right columns) show these ratios as a function of n_{e} for T corresponding to the maximum of their emissivity (full lines, see also Table 4.2), and only 1% of this maximum (dashed and dot-dashed lines). In these figures, the ratios are plotted for the Maxwellian distribution (black) and κ-distribution with $\kappa = 2$ (red).

Except for the Ni xvi 194.05 Å /185.23 Å ratio, these line ratios show mild dependence on T for Maxwellian distribution, which can introduce an error up to $0.2 - 0.3$ dex in determination
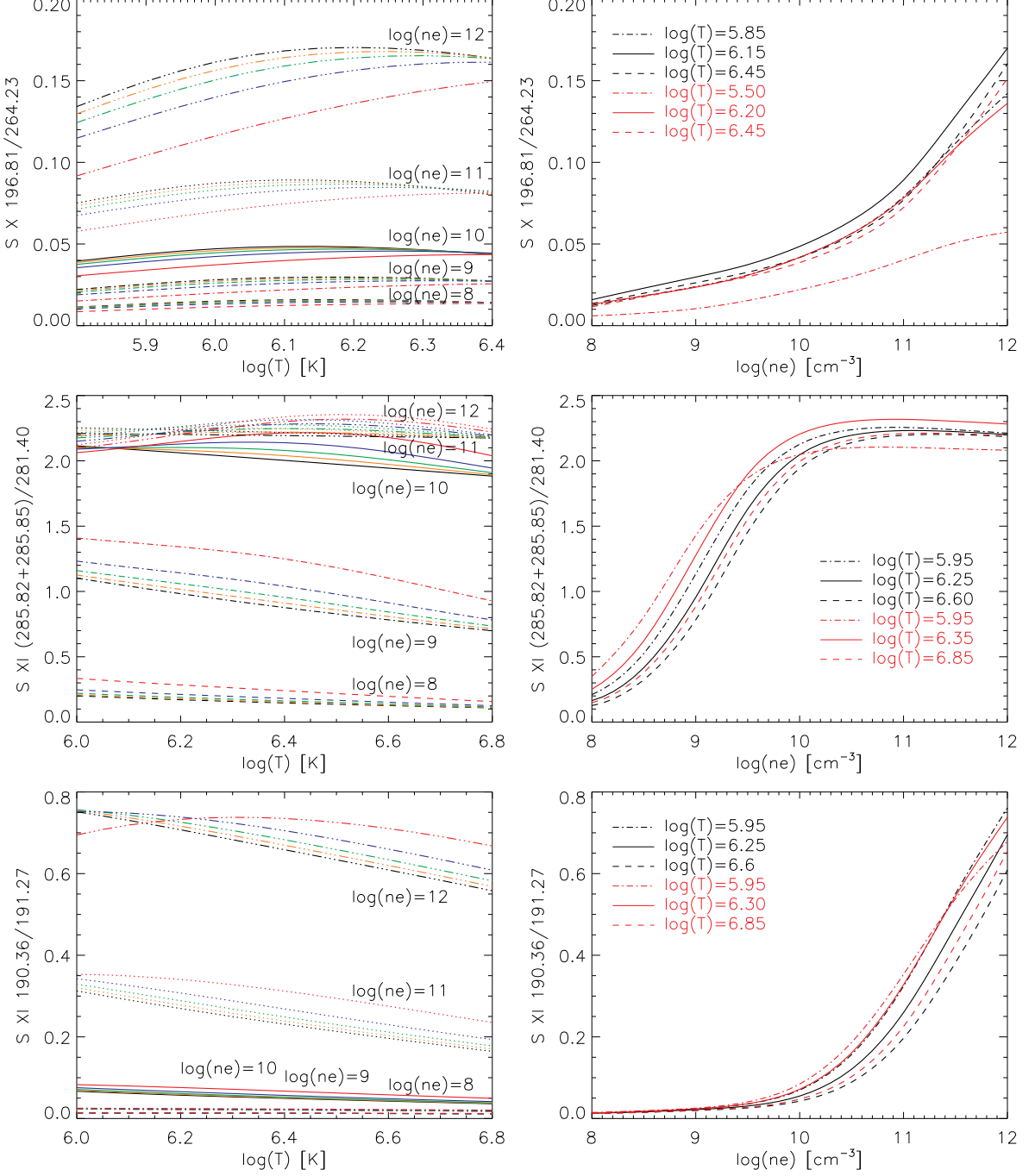
Figure 4.1: The density diagnostics from S line ratios. Left: The temperature dependencies for $\log(n_e \ [\mathrm{cm}^{-3}]))=8$ (dashed lines), 9 (dot-dashed), 10 (solid), 11 (dotted), 12 (dot-dot-dot-dashed), and for the κ-distributions ($\kappa = 2$, 3, 5, and 10 correspond to red, green, blue, and orange lines) and Maxwellian distribution (black lines). Right: Diagnostics of n_e for κ-distribution with $\kappa=2$ (red lines) and for the Maxwellian distribution (black lines). Full lines correspond to the temperature of the maximum of the line emissivities, dashed and dot-dashed lines belong to the temperature for which line emissivity reach 1% of its maximum.
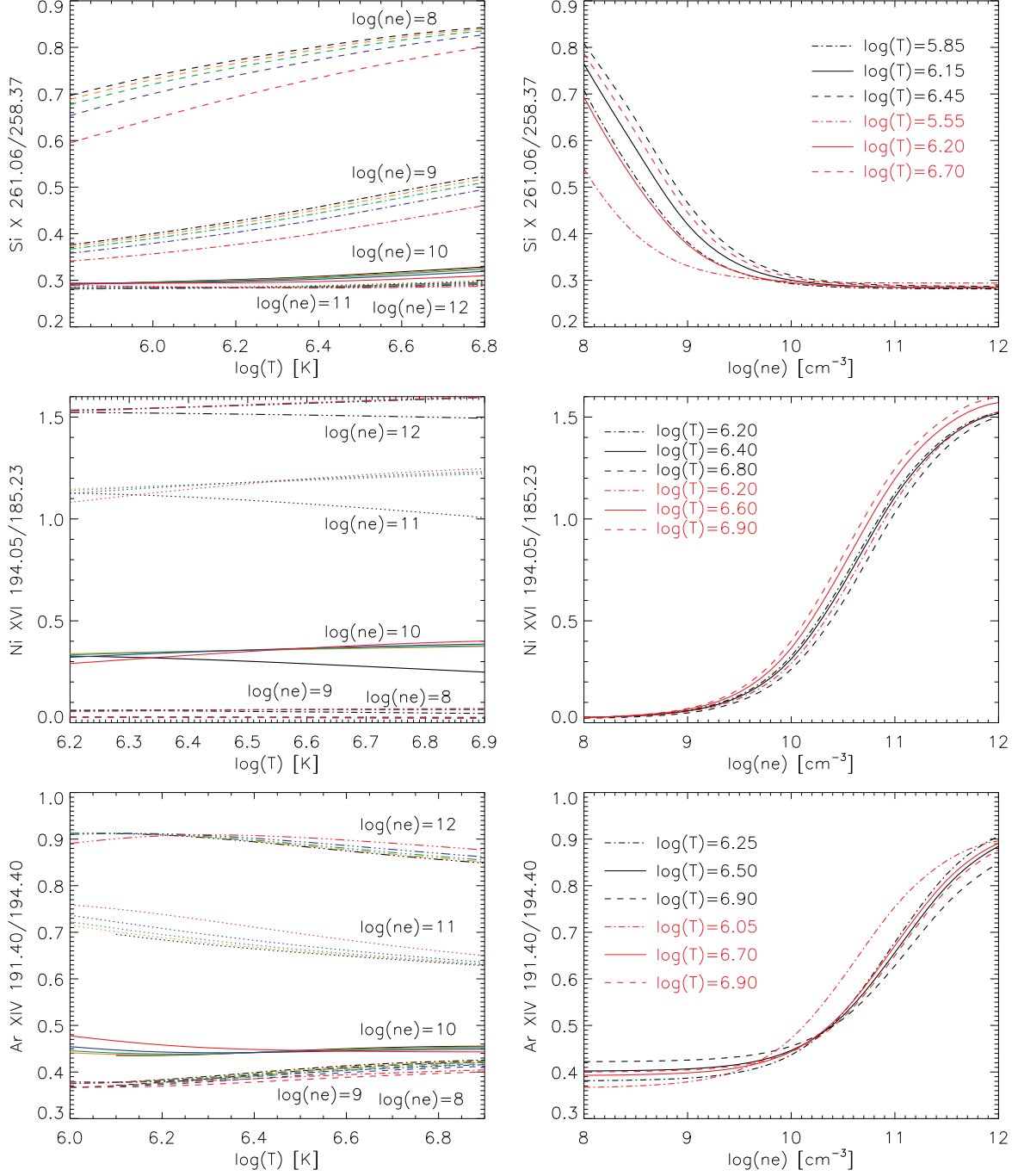
Figure 4.2: The density diagnostics from Si, Ni, and Ar line ratios. The image layout and
line and color coding are the same as in Figure 4.1.

of n_e if T is unknown. The sensitivity of these ratios to the value of κ can increase this error
even further. This is a result of two effects. First, changes in the ionization equilibrium with
κ shift the temperatures of the maximum line emissivities to different Ts (e.g., Figure 4.3).
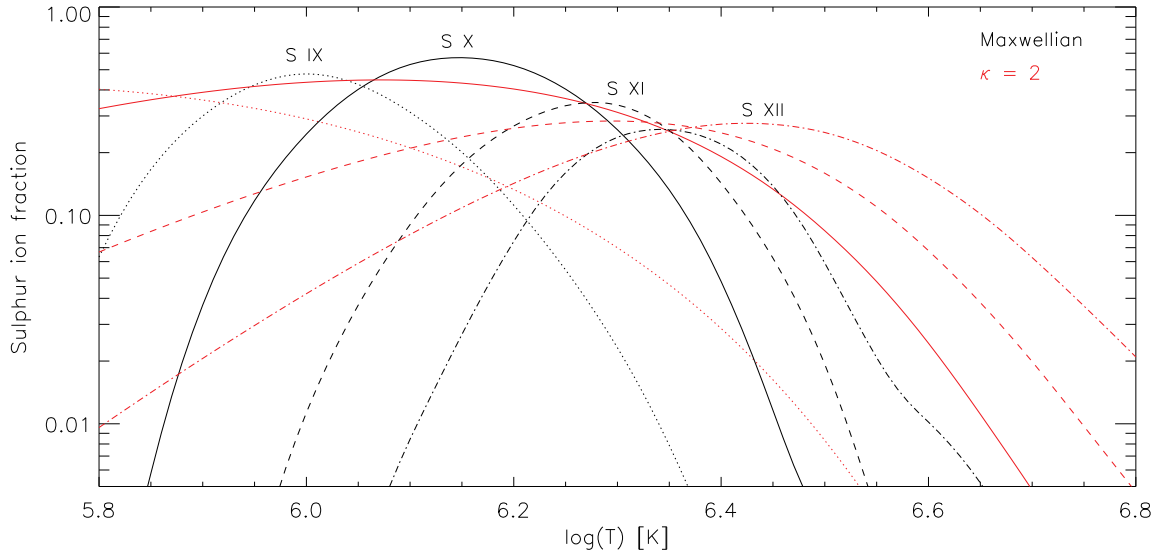
Figure 4.3: Sulphur ionization equilibrium for the Maxwellian distribution (black lines) and
κ-distribution with $\kappa = 2$ (red lines).

Simultaneously, the changes in both ionization and excitation equilibrium with κ widen the
interval of T in which the lines are formed. For $\kappa = 2$, this results in large changes with T
in the S x 196.81 Å / 264.23 Å and Si x 261.06 Å / 258.37 Å ratios (top rows of Figures 4.1 and
4.2). These changes preclude density diagnostics. Therefore, we do not recommend to use these
ratios.

Of all the lines involved in the density-sensitive line ratios, Brown et al. (2008) lists inten-
sities of several S x and Ar xiv lines only. All of the ratios calculated using these observed
intensities are either out of the theoretical ranges of the diagnostic diagrams in Figures 4.1 and
4.2 (Table 4.3), or they correspond to unrealistically high electron densities. This is probably a
result of unknown line blends. We therefore conclude that none of the proposed density-sensitive
ratios are applicable for our purposes.

Table 4.3: The observed intensity ratios for the density diagnostics.

Ratio	QS	AR1	AR2	L	L+20
S x 196.81/264.23	0.33 ± 0.04	0.12 ± 0.02	0.36 ± 0.02	0.12 ± 0.02	0.16 ± 0.02
Ar xiv 191.4/194.4			2.3 ± 0.3	2.8 ± 0.3	2.1 ± 0.4

Since we are unable to use any of the non-Fe lines for density diagnostics, we are forced

to diagnose n_{e} using the Fe lines. The density diagnostics from Fe lines and its limitations due to dependencies on T and κ are discussed in Dzifčáková and Kulinová (2010). The results for Maxwellian and $\kappa = 2$ distributions, and different regions on the Sun observed by Brown et al. (2008) are shown in Figure 4.4 and listed in Table 4.4. We note that the Fe XII $186.85 + 186.88\,\text{Å}$ is partially blended with S XI $186.84\,\text{Å}$. The intensity of S XI $186.84\,\text{Å}$ was assessed using the observed S XI $191.27\,\text{Å}$ line Young (2007), since S XI $186.84\,\text{Å}\,/\,191.27\,\text{Å} = 0.195$ for all T, n_{e}, and κ (branching ratio).
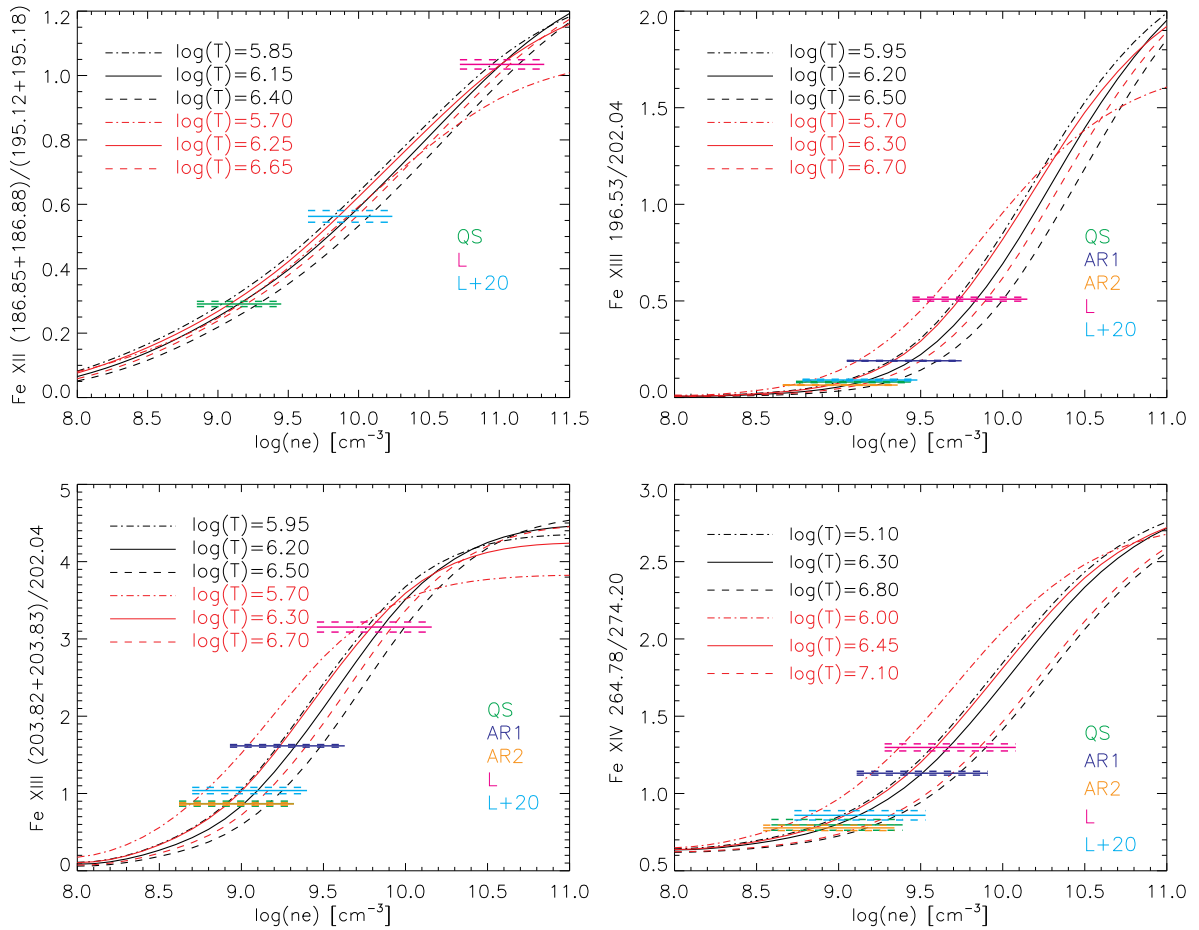
Figure 4.4: The diagnostics of the density from the Fe line ratios using observed line intensity ratios and their errors for the five regions on the Sun. The line and color coding is the same as in Figure 4.1. The self-blends are indicated as a sum of two spectral lines.

The densities diagnosed from the two Fe XIII ratios and the Fe XIV ratio are consistent within their respective errors for all five regions for Maxwellian and for $\kappa = 2$ distributions.

In this density diagnostics we do not consider the errors due to calibration, since the used ratios involve lines whose wavelengths are close to each other. In spite of this, the errors in determination of n_e are rather large, up to ≈ 0.3 dex or even larger (Table 4.4), mainly due to the dependence of the individual ratios on T (Figure 4.4). This shows the limitations of density diagnostics that are not usually considered in the literature (e.g. Tripathi et al., 2009; Warren et al., 2010; O'Dwyer et al., 2011; Winebarger et al., 2011); but see also (Young, 2007; Schmelz, Rightmire, Saar, Kimble, Worley and Pathak, 2011). However, known T can greatly improve the precision of density diagnostics. The important implication of our analysis is the finding that the densities diagnosed for $\kappa = 2$ are systematically lower by approximately 0.1 dex than for the Maxwellian distribution.

Table 4.4: Diagnosed $\log(n_e\ [\mathrm{cm}^{-3}])$ with their respective errors for the Maxwellian (Mxw) and κ-distribution with $\kappa = 2$.

Ratio	Distr.	QS	AR1	AR2	L	L+20
Fe XII						
	Mxw	$9.15^{+0.17}_{-0.15}$	Saturated	Saturated	$^{\dagger}11.02^{+0.16}_{-0.11}$	$^{\dagger}9.93^{+0.18}_{-0.16}$
(186.85+186.88)/						
(195.12+195.18)	$\kappa=2$	$9.09^{+0.15}_{+0.04}$	Saturated	Saturated	$^{\dagger}11.03^{\ddagger}$	$^{\dagger}9.85^{+0.17}_{+0.09}$
Fe XIII	Mxw	$9.14^{+0.19}_{-0.15}$	$9.45^{+0.16}_{-0.13}$	$9.06^{+0.19}_{-0.14}$	$9.85^{+0.17}_{-0.14}$	$9.18^{+0.19}_{-0.14}$
196.53/202.04	$\kappa=2$	$9.03^{+0.19}_{-0.25}$	$9.34^{+0.17}_{-0.22}$	$8.96^{+0.18}_{-0.25}$	$9.74^{+0.18}_{-0.18}$	$9.07^{+0.18}_{-0.25}$
Fe XIII						
	Mxw	$9.02^{+0.17}_{-0.12}$	$9.33^{+0.17}_{-0.11}$	$9.02^{+0.16}_{-0.12}$	$9.86^{+0.16}_{-0.12}$	$9.10^{+0.17}_{-0.12}$
(203.82+203.83)/						
202.04	$\kappa=2$	$8.92^{+0.18}_{-0.24}$	$9.24^{+0.17}_{-0.20}$	$8.92^{+0.17}_{-0.23}$	$9.80^{+0.15}_{-0.13}$	$9.01^{+0.18}_{-0.24}$
Fe XIV	Mxw	$8.99^{+0.32}_{-0.21}$	$9.51^{+0.24}_{-0.11}$	$8.94^{+0.28}_{-0.17}$	$9.68^{+0.24}_{-0.13}$	$9.13^{+0.29}_{-0.17}$
264.78/274.20	$\kappa=2$	$8.91^{+0.36}_{-0.32}$	$9.43^{+0.28}_{-0.23}$	$8.86^{+0.32}_{-0.27}$	$9.60^{+0.28}_{-0.25}$	$9.05^{+0.33}_{-0.29}$
Mean	Mxw	$9.08^{+0.21}_{-0.15}$	$9.44^{+0.19}_{-0.12}$	$9.01^{+0.21}_{-0.14}$	$9.80^{+0.19}_{-0.13}$	$9.14^{+0.22}_{-0.15}$
	$\kappa=2$	$8.99^{+0.22}_{-0.30}$	$9.34^{+0.22}_{-0.22}$	$8.91^{+0.23}_{-0.25}$	$9.72^{+0.20}_{-0.17}$	$9.04^{+0.24}_{-0.26}$

† This value is not included in the mean density

‡ The error cannot be specified (see Figure 4.4, top left).

The density diagnostics based on Fe XII ratio gives different results than other ratios, except for the quiet Sun (QS) region, where the results are consistent. For the limb regions (L and

L+20), the n_e diagnosed using the Fe XII ratio is much higher than indicated from other Fe density-sensitive ratios (Table 4.4). The fact that the electron densities diagnosed using Fe XII are problematic is well-known (e.g. Young et al., 2009; Warren et al., 2010). For the AR1 and AR2, the Fe XII 195.12 Å line is unusable for density diagnostics, since it is saturated in the 600 s exposure Brown et al. (2008).

4.3   Diagnostics of κ-Distributions

4.3.1   Single-Ion Diagnostics

Next we searched for line ratios suitable for diagnostics of the κ-distributions. First, we considered only ratios of lines produced by the same ion. In this case, the error of the theoretical line ratio is given only by errors in the excitation equilibrium and is independent of uncertainties in the ion fraction or abundances. Thus, κ-sensitive single-ion ratios should introduce the smallest uncertainty in determination of κ.

From the EIS lines listed in Table 4.1, the O IV line ratios alone satisfy previous conditions and have great sensitivity to κ. The O IV ion fraction has a maximum at $\log(T_{\max}[\mathrm{K}]) = 5.2$ for the Maxwellian distribution. These O IV line ratios are only weakly density sensitive; therefore the density diagnostics is not required for determination of κ. The ratio-ratio diagrams 182.71 Å / 202.89 Å to (253.08 + 253.10 Å) / 182.71 Å (Figure 4.5 top left), 182.71 Å / (271.57 + 271.58 Å) to (207.18 + 207.24 Å) / 182.71 Å (Figure 4.5, top right) are very sensitive to κ. Unfortunately, there are regions on the ratio-ratio diagrams where the simultaneous diagnostics of T and κ is not unique (Figure 4.5, top). These lines are also weak, so only several of them were observed by Brown et al. (2008). A dedicated observation with high exposure time to minimize the errors due to photon statistics (*i.e.*, to maximize the signal-to-noise ratio) would be required to use these low intensity lines for the determination of κ.

Instead of the self-blend 207.18 + 207.24 Å, the O IV 202.89 Å or 203.04 Å lines can be used. The line 202.89 Å is blended, but this blend can be removed (Table 4.5). The self-blend 207.18 + 207.24 Å is also blended by Mg IX 207.23 + 207.27 Å ($\log(T_{\max}[\mathrm{K}]) = 6.1$). These blends cannot be removed using branching ratio. We nevertheless tried to estimate the intensity of these blends. We used CHIANTI to calculate synthetic spectra for different DEMs included therein. We note that these DEMs were derived using the assumption of the Maxwellian distribution
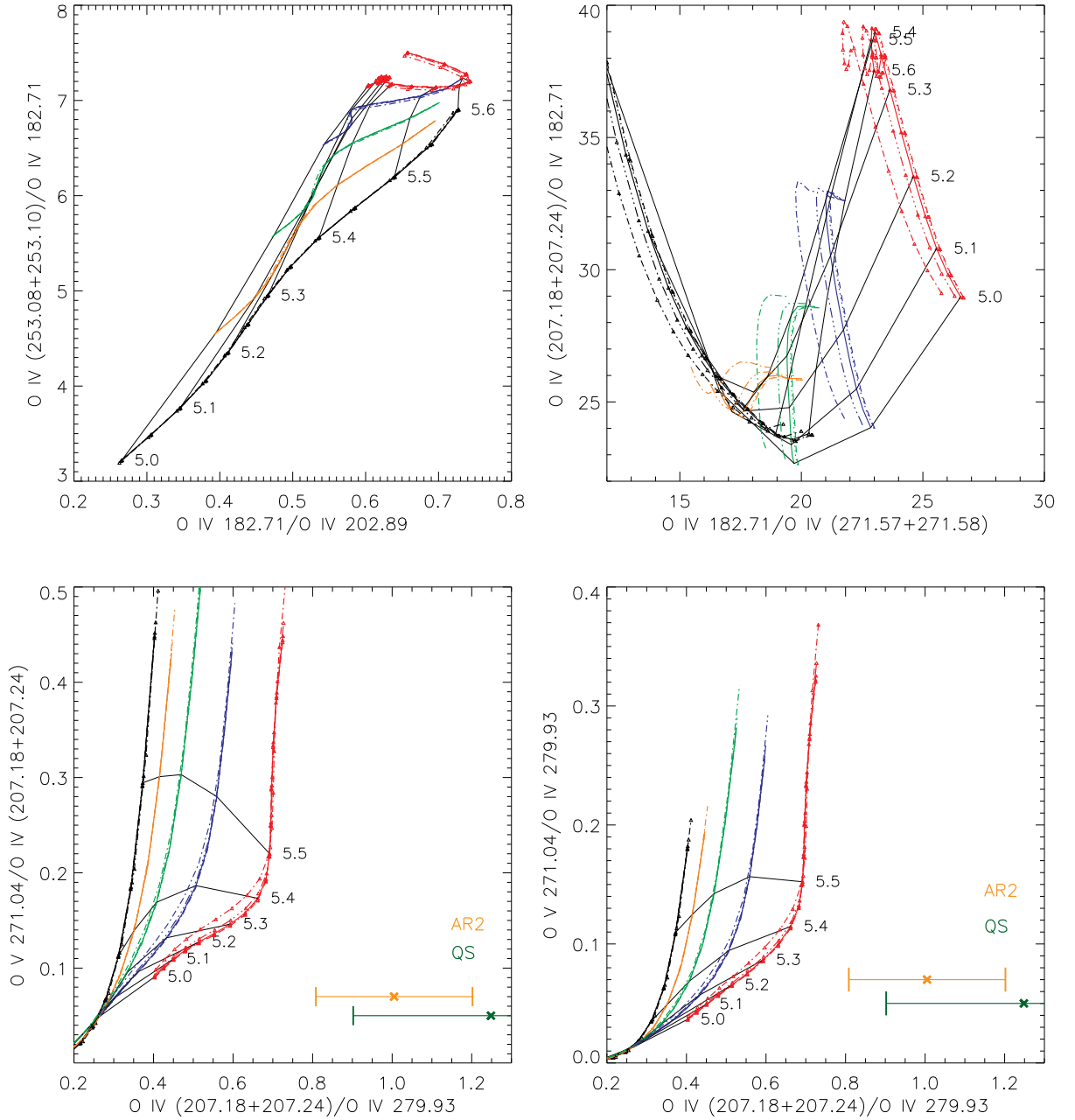
Figure 4.5: Ratio-ratio diagrams for determination of κ from oxygen lines. The line ratios are indicated in each image. The color coding represents the value of κ: $\kappa = 2$ (red lines), $\kappa = 3$ (blue), $\kappa = 5$ (green), $\kappa = 10$ (yellow), and Maxwellian distribution (black). Points with constant value of $\log(T[\text{K}])$ are connected with thin black lines. The error bars in the bottom images denote the observed O IV $(207.18 + 207.24\,\text{Å}) / 279.93\,\text{Å}$ ratios for QS (dark green) and AR2 (dark orange).

(Vernazza and Reeves, 1978; Dere and Cook, 1979). We assumed coronal abundances and different pressures ($n_e \times T = 10^{15} - 10^{16}$ cm^{-3}K). For the DEM of the coronal hole, quiet sun, active region, and flare, the contribution of Mg IX lines to the total intensity of the 207.2 Å line is approximately 1%, 7%, 38%, and 1%, respectively. Except DEM for active region, this contribution of Mg IX lines should introduce only a small error in the diagnostics. However, the real DEMs for the solar regions observed by Brown et al. (2008) are unknown. The DEM analysis is beyond the scope of this chapter, since the DEM is likely to be dependent on κ through line intensities (see Chapter 6).

4.3.2   Diagnostics Involving Ionization Equilibrium

The ions in different degrees of ionization offer additional possibilities of diagnostics. This is because the changes in the ionization equilibrium with κ are added to the changes in the excitation equilibrium Dzifčáková (2006a). On the other hand, the ionization equilibrium is a possible source of additional atomic data errors.

The combinations of O IV with O V show wide ranges of changes with κ. An example is provided in Figure 4.5 (bottom). Unfortunately, Brown et al. (2008) lists intensities of O IV (207.18 + 207.24 Å) and 279.93 Å lines for QS and AR2 only. The observed line ratios together with their error bars are shown in Figure 4.5 (the second row). The simultaneous determination of T is precluded by the absence of the O V 271.04 Å line in the observations. The ratios of the observed lines do not correspond to the Maxwellian distribution. The observed line ratio is greater for QS than for AR2. Moreover, the lower limits given by the error bars are still higher than any theoretical line ratios for $\kappa = 2$. However, we note that $\kappa = 2$ is not a limit value (Chapter 2.2).

If we consider that the contribution of Mg IX lines is up to 40% (Chapter 4.3.1), the observed line ratios still do not correspond to the Maxwellian distribution. However, since the DEMs corresponding to these observed regions are unknown, we cannot estimate the contribution of the blending Mg IX lines. Moreover, atomic data errors or additional unknown blends cannot be ruled out.

From the rest of the considered elements, Ca offers the combination of line ratios Ca XV 200.97 Å / 176.93 Å and Ca XV 200.97 Å / 182.87 Å sensitive to κ. However, these ratios show similar changes with κ so they alone cannot be used for simultaneous diagnostics of κ and T.
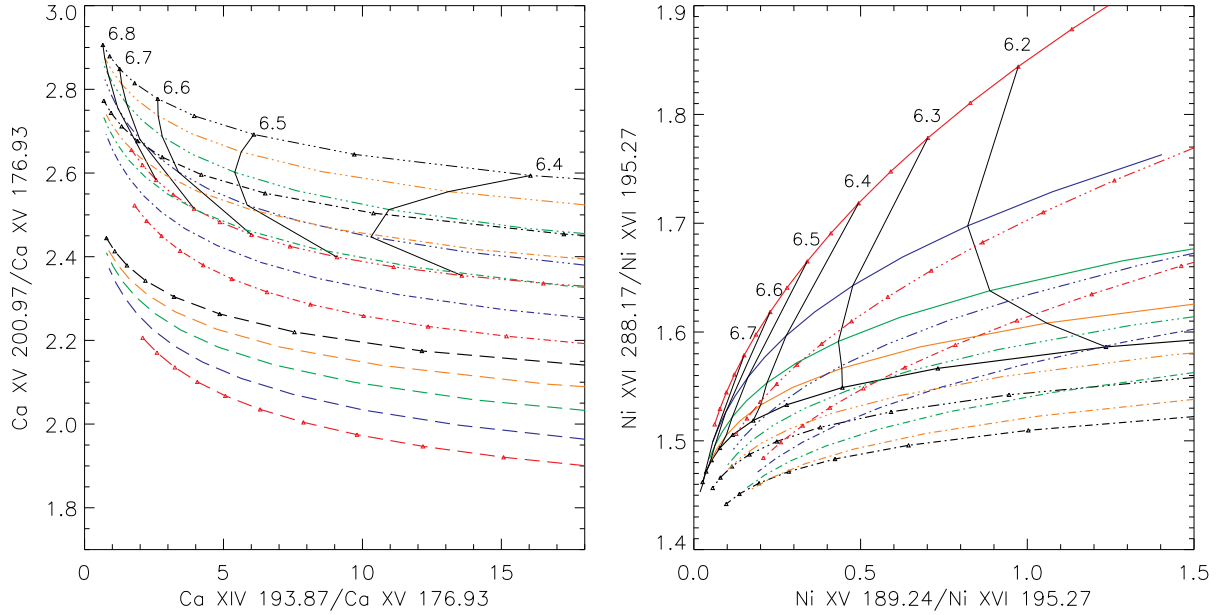
Figure 4.6: The κ-sensitive ratio-ratio diagrams for Ca (left) and Ni (right). The color coding is the same as in Figure 4.5. Different linestyles denote the values of $\log(n_{\mathrm{e}}[\mathrm{cm}^{-3}]) = 9$ (solid lines), 9.5 (dot-dot-dot-dashed), 10 (dot-dashed), and 10.5 (long dashes).

These ratios have to be combined with a line ratio containing a line of Ca ion in a higher or lower degree of ionization. An example of such a combination is shown in Figure 4.6 (left). These line ratios are also sensitive to the electron density which must be diagnosed first. Analysis involving these Ca XIV and Ca XV lines is relevant for flare or intermoss plasma.

There are only a few Ni lines in the EIS spectral bands with observable intensities (Table 4.1). From these, only Ni XVI 288.17 Å / 195.27 Å ratio ($\log(T_{\max}[\mathrm{K}]) = 6.4$) is sensitive to κ. It can be used in combination with Ni XV 189.24 Å / Ni XVI 195.27 Å (Figure 4.6, right), with an independent preceding density diagnostics. Unfortunately, Brown et al. (2008) did not observe these Ni lines so we cannot compare them with our theoretical predictions.

Sulphur lines also offer possibilities to determine the value of κ. To do it simultaneously with the diagnostics of T, the ratio of the S X lines 264.23 Å / 180.73 Å ($\log(T_{\max}[\mathrm{K}]) = 6.2$) sensitive to κ has to be used in combination with ratios involving different ionization stages, *e.g.*, with S X 264.23 Å / S XI 246.89 Å and S XI 246.89 Å / S X 180.73 Å. (Figure 4.7, top). Brown et al. (2008) lists intensities of these lines only for L and L+20. Observed ratios together with their error bars are shown in Figure 4.7 (middle and bottom rows). Here, the diagnostic ratio-
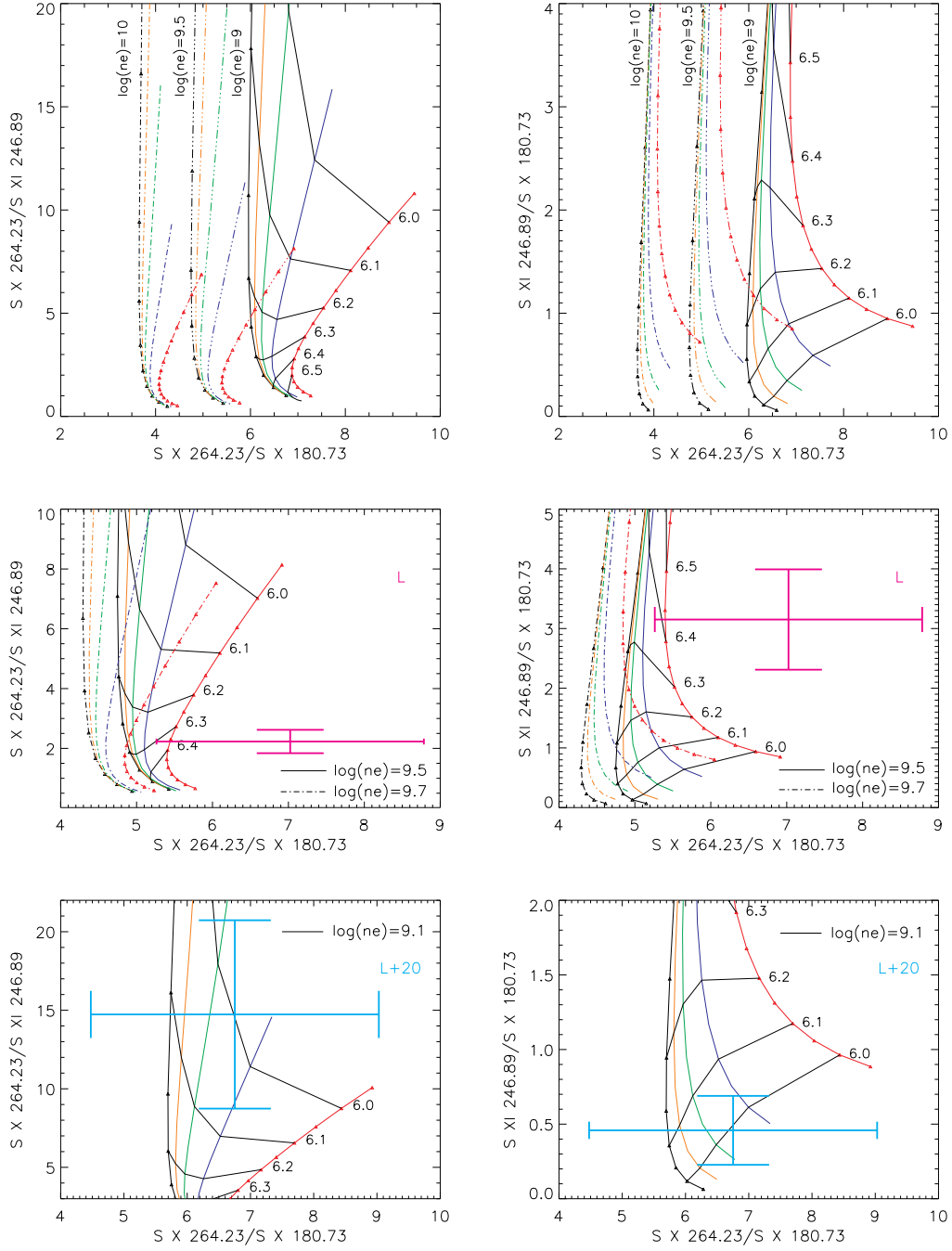
Figure 4.7: Top row: The κ-sensitive ratio-ratio diagrams for S lines. The densities and line ratios used are indicated. The color coding is the same as in previous figures. Middle row: Diagnostics of the κ-distribution from the observations on limb (L). The ratio-ratio diagram is plotted for $\log(n_e\ [\mathrm{cm}^{-3}]) = 9.5$ and 9.7 according to the diagnosed values (Table. 4.4). The observed ratios with the respective error bars are depicted by thick violet cross. Bottom row: Same as in the middle row, but for the L+20 region and the diagnosed $\log(n_e[\mathrm{cm}^{-3}]) = 9.1$. The observed ratios with their respective errors are shown by thick, light blue cross.

Table 4.5: The pairs of the line ratios observable by EIS suitable for the diagnostics of κ.

The pairs of the line ratios (wavelength in Å)
O IV 182.71 / O IV 202.89[†] – O IV (207.18 + 207.24) / O IV 202.89[†]
O IV 182.71 / O IV 202.89[†] – O IV (207.18 + 207.24) / O IV 203.04
O IV 182.71 / O IV 202.89[†] – O IV (253.08 + 253.10)[‡] / O IV 182.71
O IV 182.71 / O IV (271.57 + 271.58) – O IV (207.18 + 207.24) / O IV 182.71
O IV (207.18 + 207.24) / O IV 279.93 – O V 271.04 / O IV (207.18 + 207.24)
O IV (207.18 + 207.24) / O IV 279.93 – O V 271.04 / O IV 279.93
Ca XIV 193.87 / Ca XV 176.93 – Ca XV 200.97 / Ca XV 176.93
Ca XIV 193.87 / Ca XV 176.93 – Ca XV 200.97 / Ca XV 182.87[♮]
Ni XV 189.24 / Ni XVI 195.27[♯] – Ni XVI 288.17 / Ni XVI 195.27
S X 264.23 / S X 180.73 – S X 264.23 / S XI 246.89
S X 264.23 / S X 180.73 – S X 246.89 / S XI 180.73

[†] The Ni XV 202.86 Å blend can be removed using ratio
Ni XV 202.86 Å / 189.24 Å = 0.64 (branching ratio).

[‡] The Fe XV 253.10 Å blend can be removed using ratio
Fe XV 253.10 Å / 202.81 Å = 1.48 (branching ratio).

[♮] The Ni XV 182.84 Å blend can be removed using ratio
Ni XV 195.52 Å / 182.84 Å = 13.15 (branching ratio).

[♯] The Fe XIV 195.246 Å blend can be removed using ratio
Fe XIV 195.25 Å / 286.98 Å = 18.87 (branching ratio).

ratio diagrams are shown for the densities diagnosed for L and L+20 (Table 4.4). We note that the S X lines are formed at the same temperature as the Fe lines used for density diagnostics (Chapter 4.2).

For L observation, the line ratio S X 264.23 Å / 180.73 Å indicates that $\kappa \leq 3$ and plasma is strongly non-Maxwellian (Figure 4.7, middle row). However, the limb region is likely to be multithermal due to contributions of many overlapping structures along the line of sight (*e.g.*, moss and possibly loops; Figure 2 in Brown et al. (2008). Therefore, we cannot be sure that the plasma is non-Maxwellian. We use the data of Brown et al. (2008) for illustration of the method only.

The L+20 observation has large errors in the intensity of the S lines (Figure 4.7, third row).

The error bars are so large that the type of the distribution cannot be diagnosed even if the electron density is known. The data can only lead to constraints for T. Diagnosed $\log(T[\mathrm{K}])$ is approximately $6.0-6.2$ for the Maxwellian distribution and temperature can be lower by $\approx 0.1\,\mathrm{dex}$ for $\kappa = 2$.

Other ratios of S X or S XI lines are also sensitive to κ but they involve blended lines or have strong density sensitivity or both. These line ratios are *e.g.* S X 196.11 Å / 257.14 Å, S XI 191.27 Å / 242,59 Å, and S XI 246.90 Å / 281.40 Å.

No line ratios of Al, Ar, Mg, and Si are suitable for the diagnostics of κ-distribution. This is because the observable lines either have unknown blends, their sensitivity to κ is low, or the lines sensitive to κ are weak and thus unobservable. We summarize all ratios suitable for determination of κ in Table 4.5.

The presented methods for diagnostics of κ, temperature, and electron density from line ratios observable by Hinode/EIS are not simple. They require long-exposure observations of a single structure to minimize the errors due to photon statistics and the DEM. To reach this goal, we submitted a proposal for Hinode/EIS observations (Chapter 5) and we investigated the influence of the κ-distributions on the DEM (Chapter 6).

Chapter 5

Diagnostics of plasma parameters from HOP 226

5.1 Proposal for Hinode/EIS observations

We proposed specific observation on Hinode satellite to obtain spectral lines which could be used to diagnose κ using the methods described in Chapter 4. Selected wavelength intervals contained lines allowing for simultaneous diagnostics of electron density, temperature, and κ. The proposal was named *'Diagnostics of Non-Maxwellian electron distributions in the solar corona'* and was accepted on 20 December 2012 and was listed as the Hinode Operation Program (HOP) 226 (*http://www.isas.jaxa.jp/home/solar/hinode_op/hop.php?hop=0226*).

The proposal contained several specific requests for the Extraultraviolet Imaging Spectrometer (EIS). To reduce errors due to photon statistics for very weak lines, we proposed scanning raster type observation with 2" slit. Raster scans with 60 s and 600 s exposures was required to observe a region of 512" x 20" uninterruptedly. The slit should be located through the center of an active region near the center of the solar disk, encompassing the AR core, moss, and outlying coronal loops. We also required some additional calibration data to monitor cosmic rays and hot/warm pixels. We selected desired wavelength intervals because EIS is not able to provide the full spectra of its range, due to telemetry restrictions after failure of the primary antenna. The specifications were collectively named $KAPPA$ and $KAPPA\_SHORT$ studies for the 600 s and 60 s observations, respectively.

For the actual observation, the pointing was selected several days before the observation by the EIS observer Dr. David Williams. The observation was set to track the center of the active

region NOAA 11704 as it moved across the Sun (Fig. 5.1) on 2013 March 29 – 30.
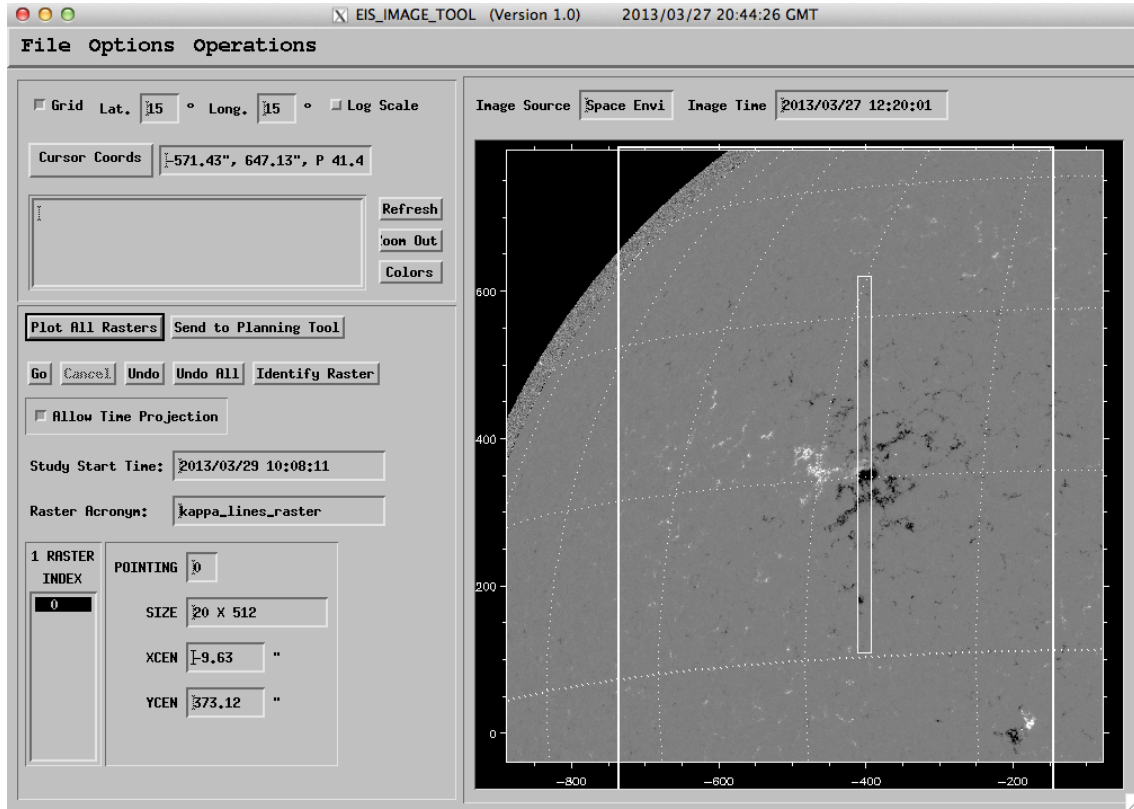
Figure 5.1: The pointing, white rectangle on magnetogram, of prepared HOP 226 displayed in operation software by EIS observer Dr. David Wiliams.

5.2 Data analysis of HOP 226

The observed level_0 data are available in .fits format online on *http://tinyurl.com/cw5cuvt*. After download, the files were calibrated by standard *eis_prep* routine using the latest in-flight radiometric calibration of the Hinode/EIS (Del Zanna, 2013a). The calibrated level_1 data contain calibrated intensities and the 1σ errors of the observed intensities at each pixel. The arrays are stored in the separate error .fits files that also contain flags for missing pixels which are not usable for scientific purposes. These missing pixels arise from a variety of causes, including saturation, detector artifacts (dust, warm pixels, hot pixels), cosmic ray hits, and missing data packets. The level_1 intensities are in physical units [$\mathrm{erg\,cm^{-2}\,s^{-1}\,sr^{-1}\,\AA^{-1}}$]. The calibration process details can be found in the EIS Software notes (available on *http://solarb.mssl.ucl.ac.uk/eiswiki/*).
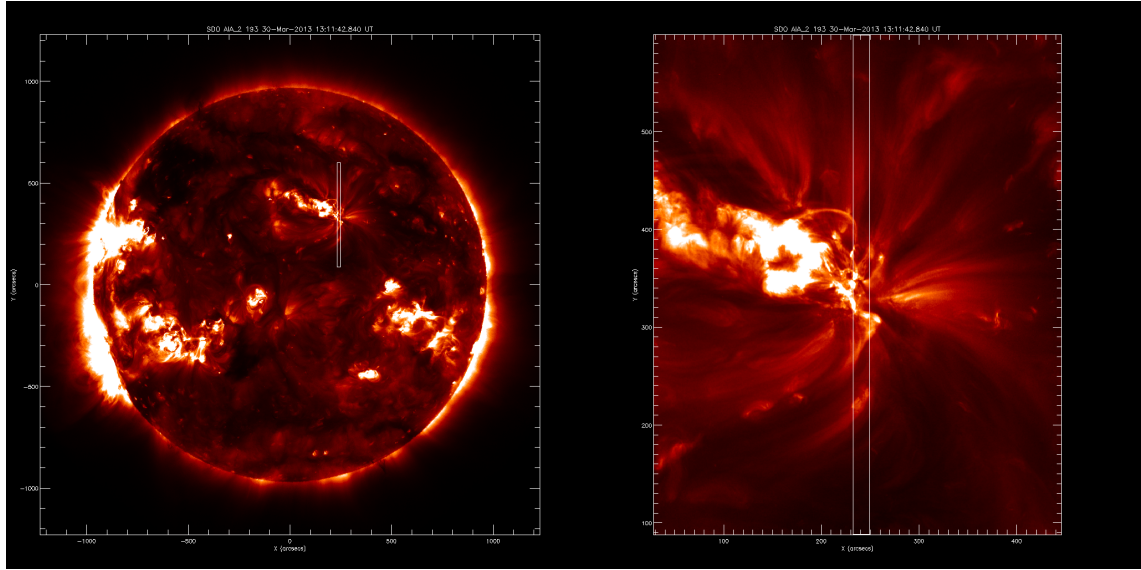
Figure 5.2: The position of EIS raster on solar disc (*left*) and on selected area (*right*) during chosen observation. The overview of solar disc is observed by AIA 193 for sufficient display of coronal structures.

The observed intensities of HOP 226 are organized in a data cube of $10 \times 512 \times 32$ pixels representing 10×2 arcsec in the x-direction, 512×1 arcsec in the y-direction, and 32×0.0223 Å in the wavelength direction. The spectral windows of Fe XIII 202.04 Å, Ca XIV 193.87 Å, and Ar XIV 194.41 Å are an exception since they contain 48, 24, and 24 pixels in wavelength direction, respectively.

The HOP 226 observation was originally proposed in order to observe weak spectral lines that could be suitable for diagnostics of plasma parameters. The exposures were set to be as long as possible to eliminate the errors due to photon statistics. Unfortunately, the rasters of 600 s exposures were burdened by missing pixels covering more than 30 % of detector. In part, this was a result of a high number of cosmic rays hits. Therefore the fitting process of weak spectral lines would be very difficult and inaccurate. Even more so, since the long-wavelength channel has suffered by degradation, making the weak lines even more weak due to very low signal to noise ratio (Del Zanna, 2013*a*).

Therefore, we focused on the observation with 60 s exposures in our analysis. The observation that started at 13:11:14 30 March 2013 contains a bright coronal loop. We assume that this loop consists of near-isothermal plasma and allows diagnostics of density and type of distribution much easier than multithermal plasma. The overview of EIS raster position
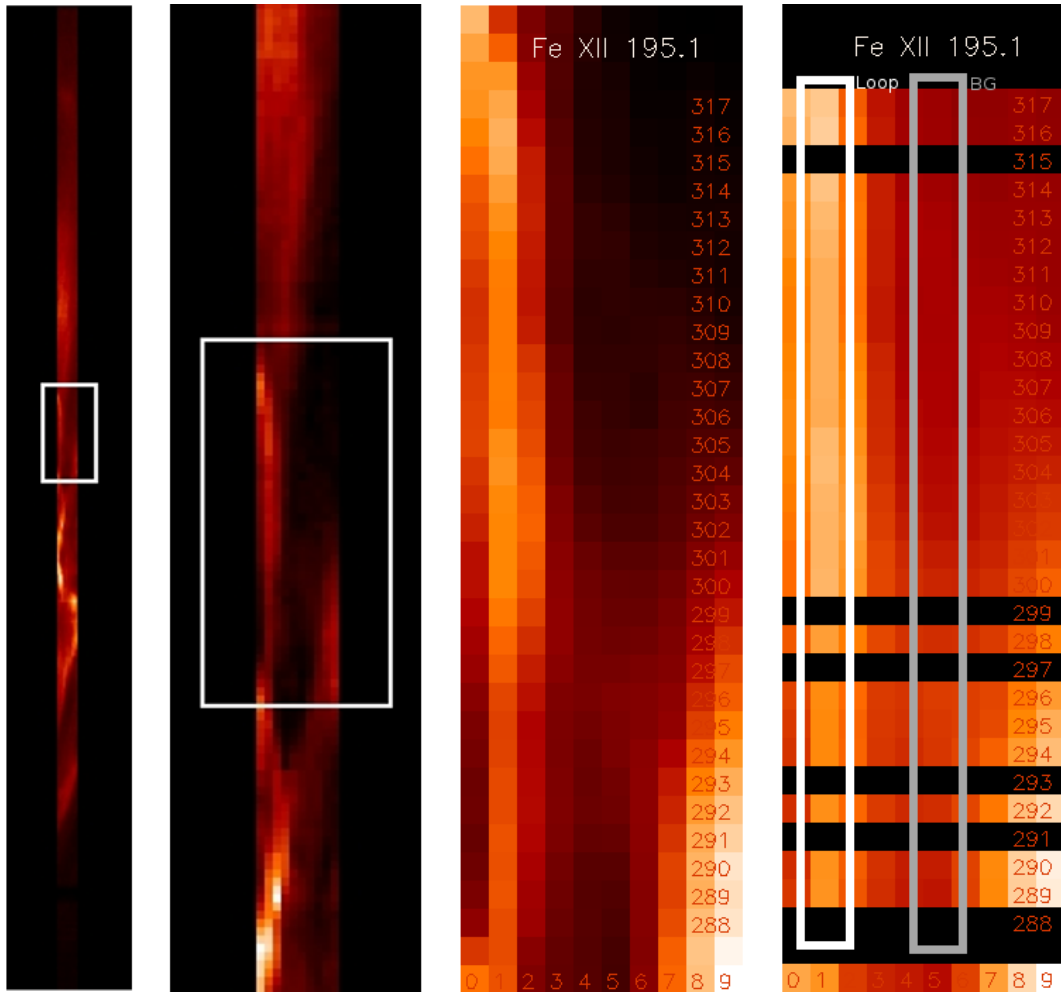
Figure 5.3: The selected area of interest is denoted by white rectangle on a full scan raster (*left*). The zoom in of selected area with the well-visible coronal loop (*middle-left*). Zoom of the selected area with spatial position of individual pixels is shown in *middle-right*. Selected loop and background pixels are shown in *right*. Each pixel shows the total integrated intensity over the entire Fe XII wavelength window containing the $195.12\,\text{Å} + 195.18\,\text{Å}$ self-blend. If the peak of the line profile contains any missing pixels, the pixel is left black.

during this observation is shown in Fig. 5.2. The position of the analyzed structure within the selected observation is displayed in Fig. 5.3, where the intensity of each spatial pixel is a sum of intensities over whole spectral window. We selected the specific pixels that show the bright coronal loop, as well as the nearby coronal background (Fig. 5.3, *right*). Than the spatial pixels were averaged for each wavelength while the missing pixels were excluded. After that, averaged background spectrum was subtracted from the averaged loop spectrum and the result was fitted

by a Gaussian profile with the *xcfit* routine. Examples of fitted spectra are displayed in Fig. 5.4. It was necessary to involve all intense lines and their blends to obtain good approximations. Once the line center intensity and FWHM of the line are obtained by the fit, the total intensity is easily calculated.

5.3 Diagnostics of density, κ-distributions, and temperature

For the diagnostics of plasma parameters, we used the methods described in Chapter 4. As we presented in Chapter 4.2 several strong Fe lines are very suitable for density diagnostics. However, we were not able to use the O and S line ratios proposed for the diagnostics of κ and T in Chapter 4. The intensities of the proposed lines were very low in the 60 s exposures. Therefore we used strong Fe lines according to the new atomic data for the diagnostics of κ and T that were selected by Dzifčáková (2014, private communication). These ratios were investigated and selected using the modification of CHIANTI 7.1 for the calculation of synthetic spectra for κ-distributions. The synthetic intensities were calculated for densities $\log(n_e[\mathrm{cm}^{-3}]) = 8$–12, temperatures $\log(T[\mathrm{K}])=5.0$–7.5, and Maxwellian and κ-distributions with $\kappa=10$, 5, 3, 2. The Fe lines selected for the diagnostics are listed in Table 5.1 together with their observed intensities and 1-σ uncertainties determined using the method described in Chapter 5.2 with calibration errors.

Densities diagnosed using the line ratios of Fe XI and Fe XIII are shown in Table 5.2 and in Fig. 5.5. The dependence of the line ratios on density in Fig. 5.5 is shown for the temperature, for which the emissivity of the line reaches its maximum (solid lines) and for temperatures for which the emissivity of the line falls on the 1 % of its maximum (dashed and dot-dashed lines). Densities for the loop structure from different line ratios agree within their errors (Table 5.2). The mean density for the Maxwellian distribution is diagnosed as $\log(n_e[\mathrm{cm}^{-3}]) = 9.38^{+0.19}_{-0.15}$ and for the κ-distribution with $\kappa=2$ as $\log(n_e[\mathrm{cm}^{-3}]) = 9.29^{+0.19}_{-0.15}$. This result is also consistent with our previous analysis (see Chapter 4.2), where the densities diagnosed for $\kappa = 2$ were systematically lower by approximately 0.1 dex in comparison with the Maxwellian distribution.

The diagnostics of κ-distribution is presented in Fig. 5.6 and in Table 5.3. The ratios of Fe XI to Fe XII line intensities have a high sensitivity for diagnostics of κ. These ratios are also affected by changes in the ionization equilibrium with κ. Changes in the ionization equilibrium
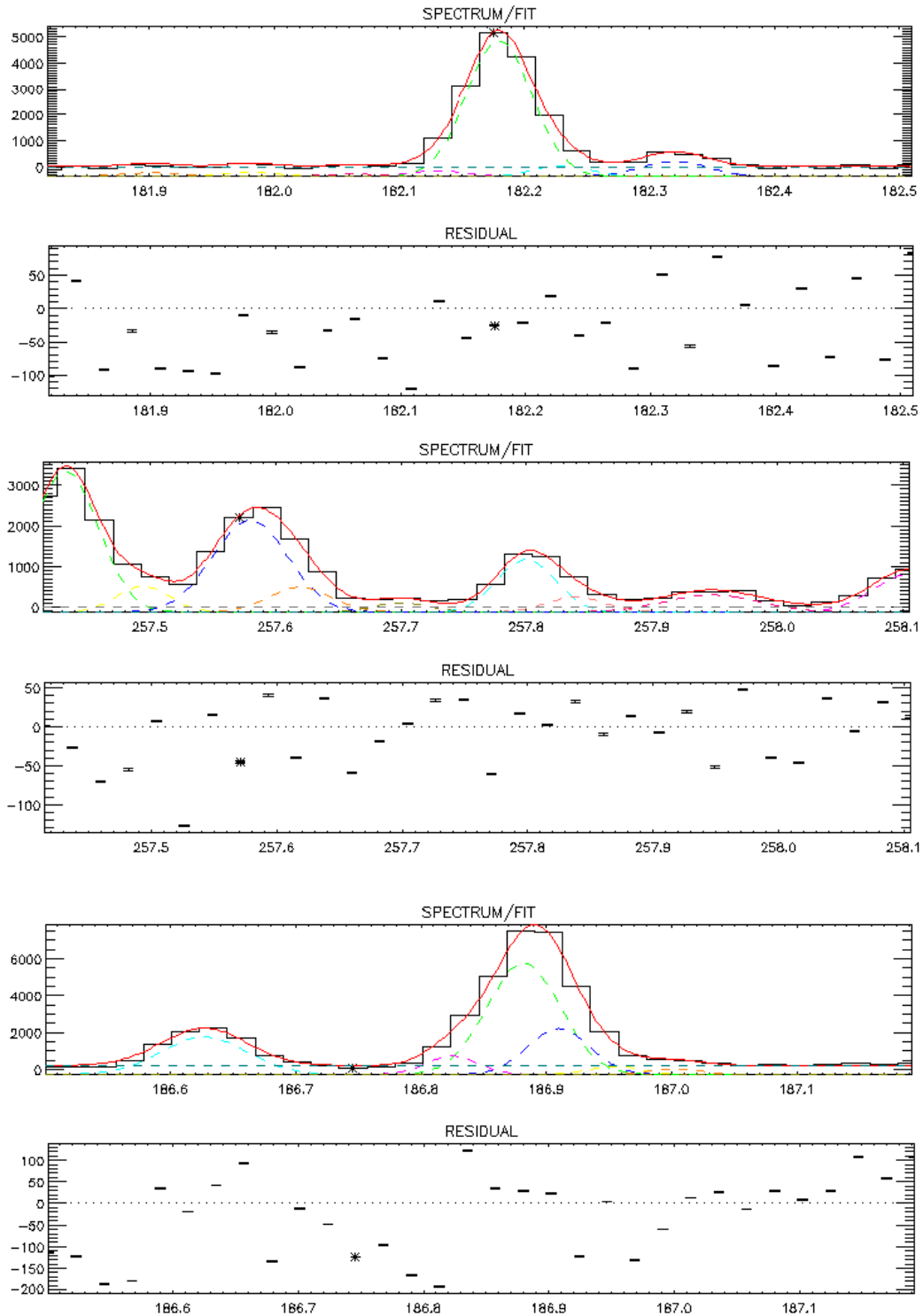
Figure 5.4: Observed spectra in the wavelength windows of Fe XI 182.17 Å (*top*), Fe XI (257.54+257.55) Å (*middle*), and Fe XII (186.85+186.88) Å (*bottom*) are fitted by Gaussian functions in *xcfit* routine. The respective residuals for fitted spectrum are shown bellow each spectrum and they present the precision of approximations.
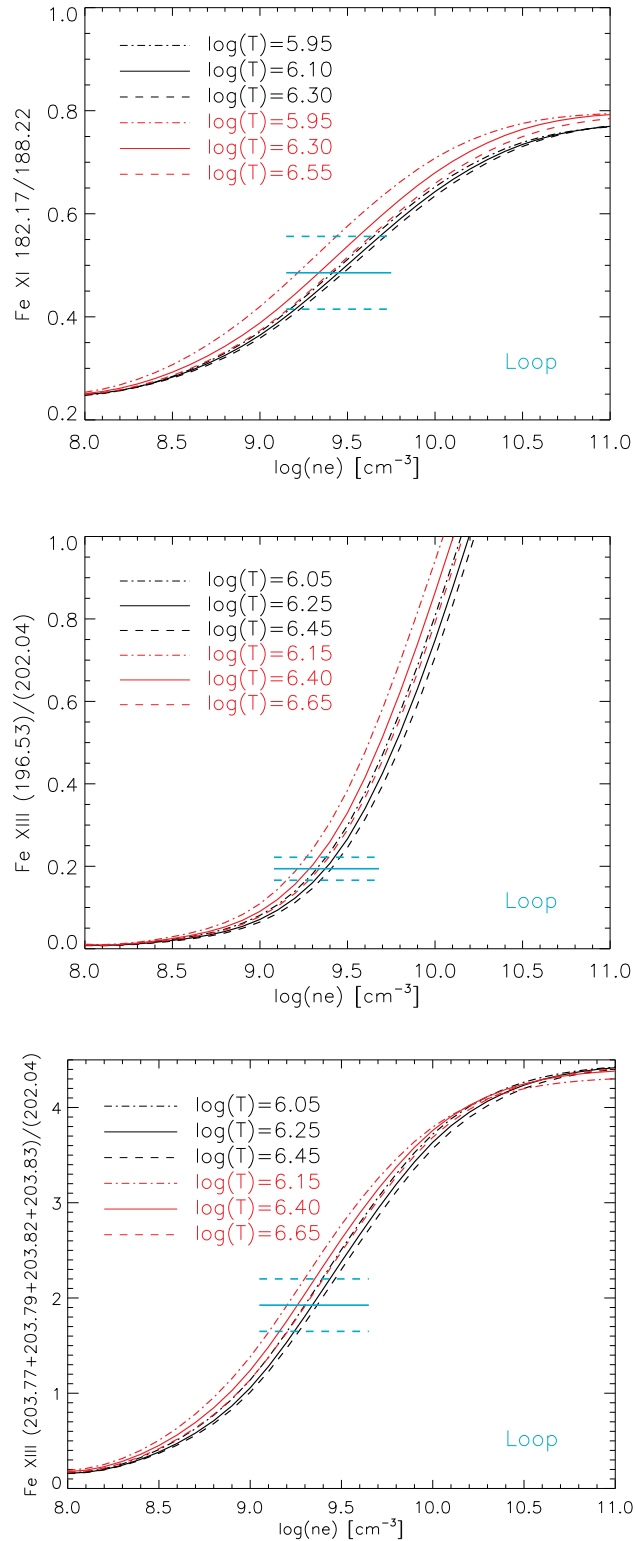
Figure 5.5: Density diagnostics using Fe line ratios. Synthetic intensities for Maxwellian distributions (*black*) and $\kappa=2$ distribution (*red*) are displayed. Observed intensity ratios of loop are indicated with their respective errors.

Table 5.1: List of lines used for diagnostics. Wavelengths are in [Å] and observed intensities and their errors are in [$\mathrm{erg\,cm^{-2}\,s^{-1}\,sr^{-1}\,\text{Å}^{-1}}$]. The self-blends are indicated.

Ion	λ	Intensity	Errors	Notes
Fe XI	182.17	795	114	
Fe XI	188.22	1637	232	
Fe XI	257.54+257.55	398	56	self-blend
Fe XI	257.77	178	27	
Fe XII	186.85+186.89	1405	198	self-blend
Fe XII	195.12+195.18	2254	317	self-blend
Fe XIII	196.53	261	38	
Fe XIII	202.04	1346	192	
Fe XIII	203.77+203.79+203.82+203.83	2590	363	self-blend

Table 5.2: The ratios of the line intensities I_1/I_2 sensitive to the density and diagnosed $\log(n_\mathrm{e}\ [\mathrm{cm^{-3}}])$ with their respective errors for the Maxwellian (Mxw.) and κ-distribution with $\kappa = 2$ of the coronal loop structure.

Ratio	I_1/I_2	$\log(n_\mathrm{e})$ for Mxw.	$\log(n_\mathrm{e})$ for $\kappa = 2$
Fe XI 182.17/188.22	0.49	$9.43^{+0.26}_{-0.19}$	$9.32^{+0.28}_{-0.14}$
Fe XIII 196.53/202.04	0.19	$9.37^{+0.09}_{-0.08}$	$9.28^{+0.11}_{-0.13}$
Fe XIII (203.77+203.79+203.82+203.83)/202.04	1.92	$9.35^{+0.19}_{-0.15}$	$9.27^{+0.15}_{-0.17}$
Mean		$9.38^{+0.19}_{-0.15}$	$9.29^{+0.19}_{-0.15}$

increase the sensitivity to κ, which can then be detected more readily.

The diagnosed distribution is unlikely to be Maxwellian and value of diagnosed κ-distribution is very close to $\kappa=2$ (Fig. 5.6). However, the observed line intensity ratios do not exactly match the predicted ratio-ratio diagrams. The predicted ratio-ratio diagrams were calculated for the diagnosed densities of $\log(n_e[\mathrm{cm^{-3}}]) = 9.0$–9.5 and values of $\kappa = 2, 3, 5, 10$, and Maxwellian. This mismatch can be a result of unknown blends or self-blends, lower values of κ in the observed plasmas, or unknown factors. Different ratios of Fe XII to Fe XI line intensities correspond to different temperatures for any distribution (Fig. 5.6) what suggested that plasma could be multithermal or there could be a problem with atomic data. We note that errors due to photon statistics, calibration errors and uncertainties of atomic data were taken into account in the

Table 5.3: Diagnosed values of κ and $\log(T[\mathrm{K}])$ with their respective errors of the coronal loop structure.

Ratio	κ	$\log(T[\mathrm{K}])$
Fe XI 182.17/257.77 – Fe XII (186.85+186.88)/Fe XI 257.77	< 2	$6.3 - 6.4$
Fe XI 182.17/257.77 – Fe XII (195.12+195.18)/Fe XI 257.77	≤ 2	$6.15 - 6.25$
Fe XI 182.17/(257.54+257.55) – Fe XII (186.85+186.88)/Fe XI (257.54+257.55)	< 2	$6.3 - 6.4$
Fe XI 182.17/(257.54+257.55) – Fe XII (195.12+195.18)/Fe XI (257.54+257.55)	≤ 2	$6.15 - 6.25$
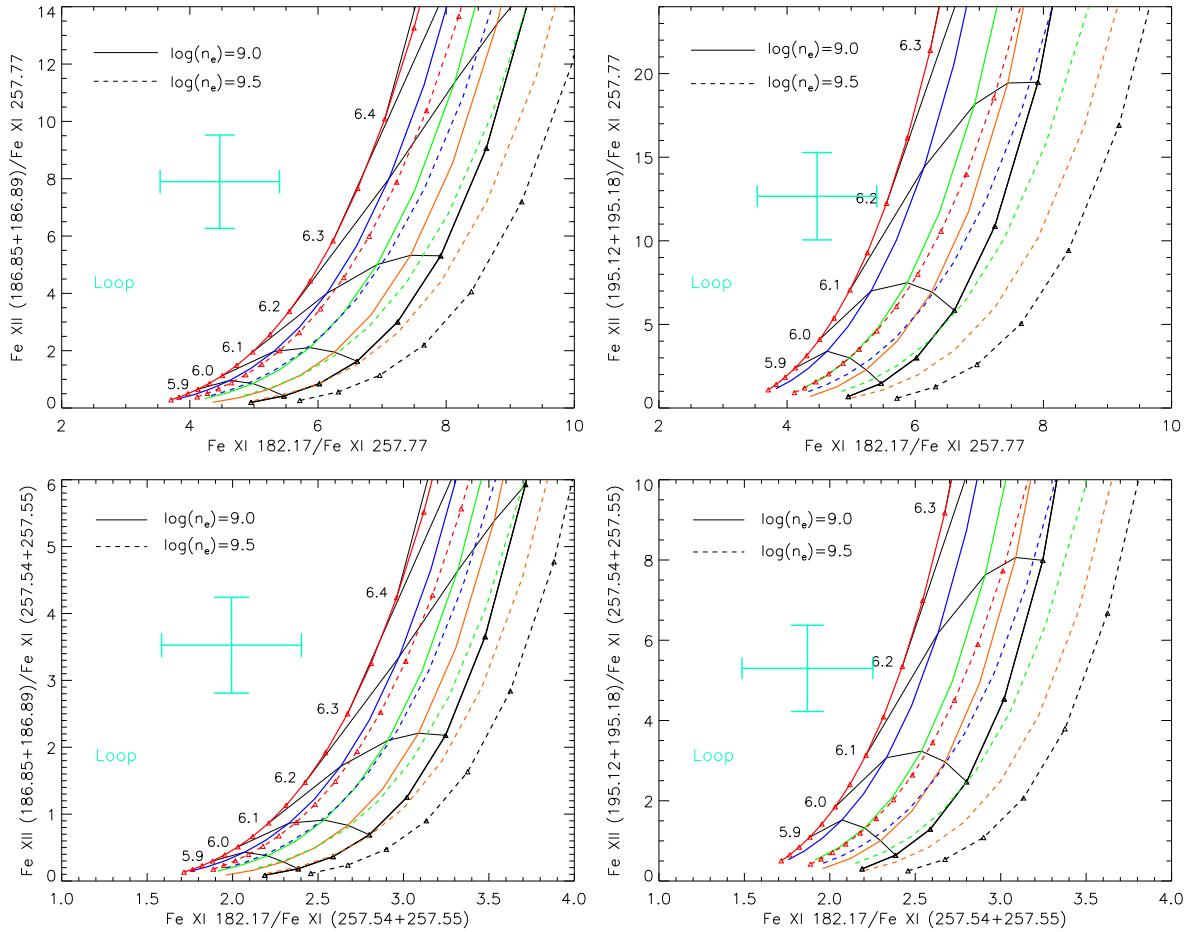
Figure 5.6: Ratio-ratio diagrams for determination of κ from iron lines. Line intensity ratios for the observed loop are indicated by the cross with its error bars. The color coding represents the value of κ: $\kappa = 2$ (red lines), $\kappa = 3$ (blue), $\kappa = 5$ (green), $\kappa = 10$ (yellow), and Maxwellian distribution (black). Points with constant value of $\log(T[\mathrm{K}])$ are connected with thin black lines. Different line styles representing different densities are indicated.
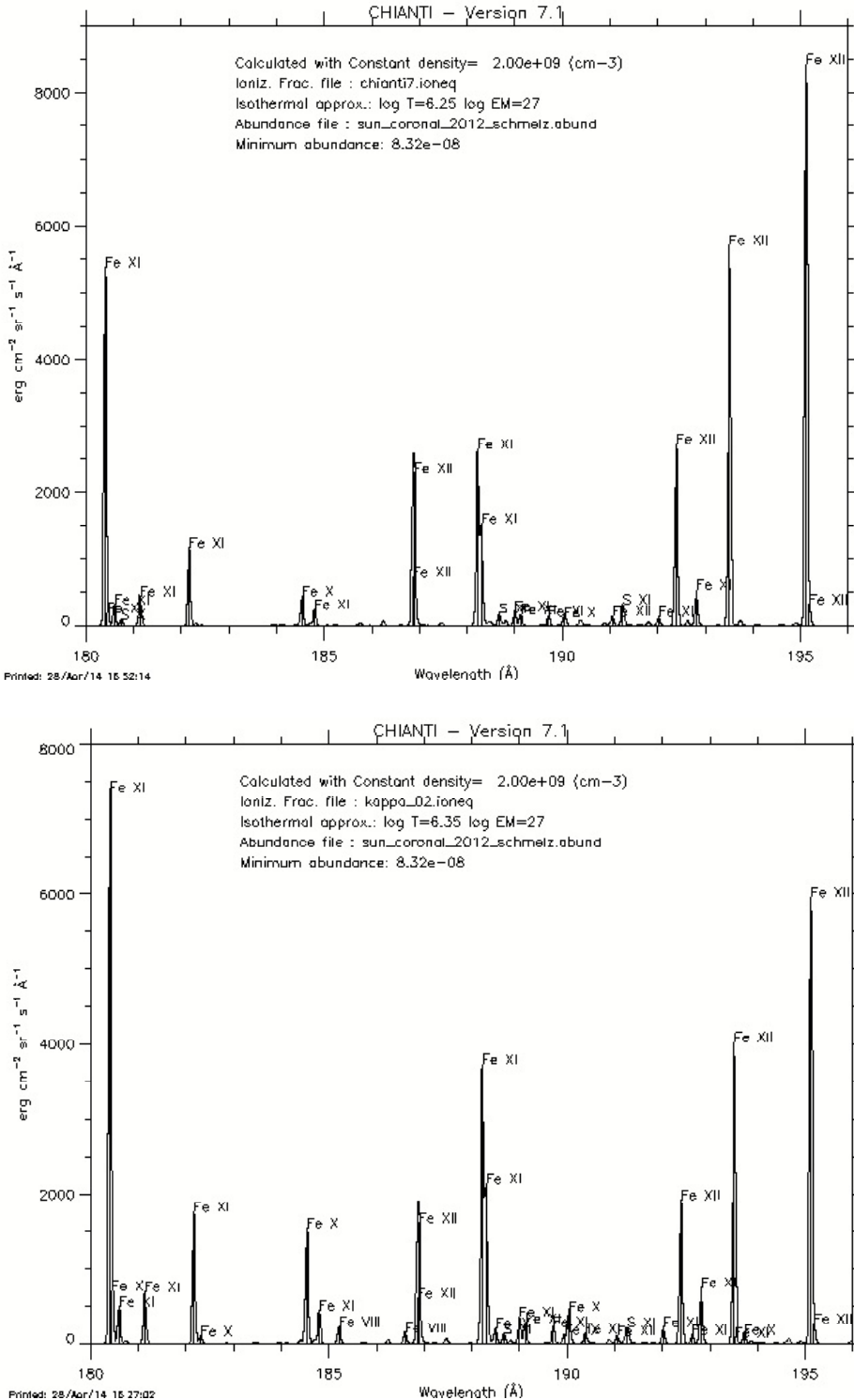
Figure 5.7: Synthetic spectra from 180–196 Å calculated by CHIANTI 7.1 and its modification for the κ-distribution using diagnosed parameters as input. The spectrum calculated assuming Maxwellian distribution (*top*) in overview with spectrum calculated by κ- distribution with κ=2 (*button*).
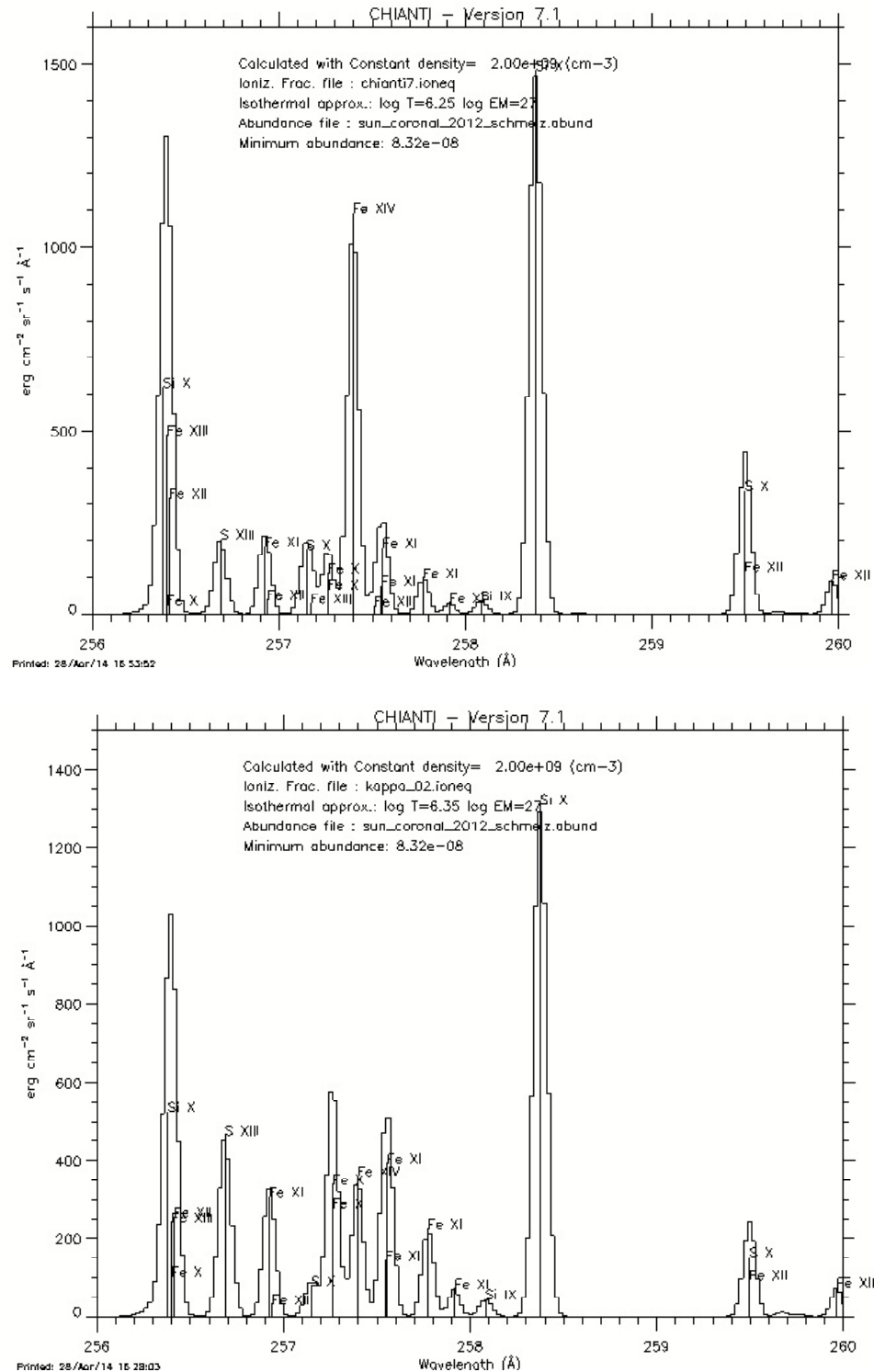
Figure 5.8: Synthetic spectra from 256–260 Å calculated by CHIANTI 7.1 and its modification for the κ-distribution using diagnosed parameters as input. The spectrum calculated assuming Maxwellian distribution (*top*) in overview with spectrum calculated by κ- distribution with κ=2 (*button*).

estimation of error bars in Fig. 5.6. The temperatures diagnosed using individual ratio-ratio diagrams, ≈ 6.1–6.3 are however consistent with typical temperatures detected in coronal loops. Note also that all four ratio-ratio diagrams show consistently that $\kappa < 2$, which may not be a coincidence.

We conclude that the diagnostics presented here do not provide conclusive and unambiguous evidence for the presence of the κ-distributions in the solar corona. However, these results are suggestive, and can represent only one piece of the puzzle that can lead to a more complex picture of the existence of non-Maxwellian distributions in the solar corona (see also Chapter 6).

Figs. 5.7 and 5.8 illustrate the changes in the spectra with κ. It is seen that the spectra are very similar for different distributions. The ratios of the line intensities belonging to a single ion are very similar in both cases. Spectra differ mainly in the relative intensities of lines for different ions. We note, that our EIS observation covers only several narrow spectral windows within displayed wavelength ranges. Therefore, we can not find all these changes in observed spectra.

Our observation proposed for EIS instrument offered us possibility to test data processing, our diagnostic methods, and the complexities behind the determination of the uncertainty. It also shows the need for future observations with lower calibration errors and better spectral resolution.

Chapter 6

DEM analysis and the κ-distributions

6.1 DEM reconstructing methods

In optically thin plasmas, the resulting observed emission along a given line of sight can consist of contributions from many individual plasma elements often with different temperatures and densities. Especially in the case of the solar corona, inadequate spatial resolution of the instruments can prevent the resolution of individual small-scale structures present within a given detector pixel (see DeForest, 2007; Cirtain et al., 2013; Peter et al., 2013). Overlapping structures are also commonly observed. The situation is, furthermore, complicated by presence of a diffuse background (e.g., Aschwanden et al., 2008) that is ubiquitous and of unknown origin. This means that the plasma observed by a given instrument within one of its detector elements will often be multithermal, even if careful background removal were performed. Such observational data are typically analyzed with the help of the differential emission measure techniques. The differential emission measure (DEM) indicates the amount of emission from plasmas at a specific temperature (see definition: Chapter 3 Eq. 3.19). It can reflect the properties, such as the coronal heating mechanism, and was intensively investigated for variety of solar structures and events for several decades (e.g., Craig and Brown, 1976; Craig, 1977; Sylwester et al., 1980; Fludra and Sylwester, 1986; Thompson, 1990; Judge et al., 1997; Lanzafame et al., 2002, 2005; Schmelz and Martens, 2006; Parenti and Vial, 2007; Siarkowski et al., 2008; Reale et al., 2009; Brooks et al., 2011, 2012; O'Dwyer et al., 2011; Winebarger et al., 2012; Hannah and Kontar, 2012; Schmelz et al., 2009; Schmelz, Worley, Anderson, Pathak, Kimble, Jenkins and Saar, 2011;

Schmelz et al., 2013; Del Zanna et al., 2011; Del Zanna, 2013*b*).

The calculation of DEM for a set of observed intensities of spectral lines consists of inverting Eq. 3.20 where the contribution function for each line is known. The inversion has two sources of uncertainties: errors of the observed intensities and uncertainties in the atomic data that are reflected in calculation of the contribution function. Moreover, the mathematical calculation of the inversion process itself poses some additional problems. These mathematical difficulties are reviewed in Jefferies et al. (1972); Craig and Brown (1976, 1986), and references therein. Phillips et al. (2008) provide review of the main DEM reconstructing methods. They can be grouped into three main categories: iterative techniques, integral inversion techniques, and Monte Carlo techniques.

The determination of $DEM(T)$ without formally inverting Eq. 3.20 consists of an iterative technique that starts from a known, initial $DEM^{(0)}(T)$. This method was evolved and it is known as Withbroe-Sylwester method (Withbroe, 1975; Sylwester et al., 1980). A slightly different version of iterative technique was developed by Landi and Landini (1997). This method has the advantage of providing a self-consistent definition of the temperature associated to each line's correction, which takes into account both the contribution function of the line and the shape of the DEM. However, it poses several problems when a few lines with similar formation temperature are considered. Some additional corrections are required to avoid instabilities and sharp oscillations of the solution.

Inversion methods are applicable if some addition conditions are established. Otherwise, they provide non-unique and oscillatory solutions, which may also be negative and therefore unphysical. McIntosh (2000) devised a maximum entropy method to optimize the solution. The advantage is fast convergence of $DEM(T)$ and consistent results. But it is important to take care on errors in the atomic data and optimum subset of spectral lines has to be selected. Several regularized inversion methods and maximum entropy regularization method have also been tested on the simulated EUV data (Monsignori Fossi and Landini, 1991; Judge et al., 1997). The regularization method by Hannah and Kontar (2012) robustly and quickly recovers the DEM.

Kashyap and Drake (1998) developed a method for the reconstruction of DEM based on Metropolis Markov-chain Monte Carlo (MCMC) method. This method is suitable for problems involving a large number of unknown parameters, such as elemental abundances, and enables realistic estimation of the final uncertainties on the derived results. This technique also consider

the smoothness assumption, which is generally adopted by inversion or iterative techniques. The smoothing is confined only to local scales that depend on widths of the contribution functions. Disadvantage of this method is that it can be computationally intensive because the convergence is slow. MCMC method is part of PINTofALE spectral analysis package.

One of the first used methods, the Withbroe-Sylwester (W-S) method (Withbroe, 1975; Sylwester et al., 1980), and one of the most robust methods, the regularization method (RIM, Hannah and Kontar, 2012), have been employed in this work to independently verify results. The W-S method for DEM reconstruction was introduced by Withbroe (1975) and improved and tested by Sylwester et al. (1980). It was compared to other methods for the calculation of DEM (e.g., Fludra and Sylwester, 1986; Siarkowski et al., 2008) and applied on solar data (e.g., Sylwester et al., 2010). The $(n + 1)$ th approximation of a DEM model is given by

$$DEM^{(n+1)}(T) = DEM^{(n)}(T) \frac{\sum\limits_{ji} I_{ji}^{\mathrm{obs}} W_{ji}(T)/I_{ji}^{(n)}}{\sum\limits_{ji} W_{ji}(T)} \ , \tag{6.1}$$

where I_{ji}^{obs} is the observed intensity in the line λ_{ji} and $I_{ji}^{(n)}$ is the intensity predicted in the nth iteration. The weight function $W_{ji}(T)$ is defined as

$$W_{ji}(T) = G_{ji}(T, N_e, \kappa) DEM^{(n)}(T) \frac{\int_T G_{ji}(T, N_e, \kappa) DEM^{(n)}(T) dT}{\int_T [G_{ji}(T, N_e, \kappa) DEM^{(n)}(T)]^2 dT} \ . \tag{6.2}$$

The weight functions $W_{ji}(T)$ are chosen semi-empirically to improve the model most efficiently at temperatures where the line λ_{ji} is formed. In the calculation, the initial approximation is $DEM^{(0)}(T) = \mathrm{const.}$, which seems reasonable when no other a priori information exists. Than can be calculated $DEM^{(n+1)}(T)$ and it can be used as an initial DEM function in equation:

$$I_{ji}^{(n+1)} = \frac{1}{4\pi} \int_T G_{ji}(T, N_e, \kappa) DEM^{(n+1)}(T) dT \tag{6.3}$$

Then $I_{ji}^{(n+1)}$ and $I_{ji}^{\mathrm{obs}}/I_{ji}^{(n+1)}$ can be calculated and the procedure can be repeated in definite number of iterations or until the ratios $I_{ji}^{\mathrm{obs}}/I_{ji}^{(n+1)}$ are unity within uncertainties. This method fulfills the requirement that the emission measure should always be positive, because the operations for calculation of next approximation of $DEM^{(n)}(T)$ do not change the sign. The Eq. 6.1 ensure that the correction provided by each line contributes just to these temperatures where the line is formed, what is the advantage of this method.

The example of calculated DEM using W-S method is shown in Fig. 6.1 (*left*) for active region core. The convergence of iteration process for this example of DEM calculation and for
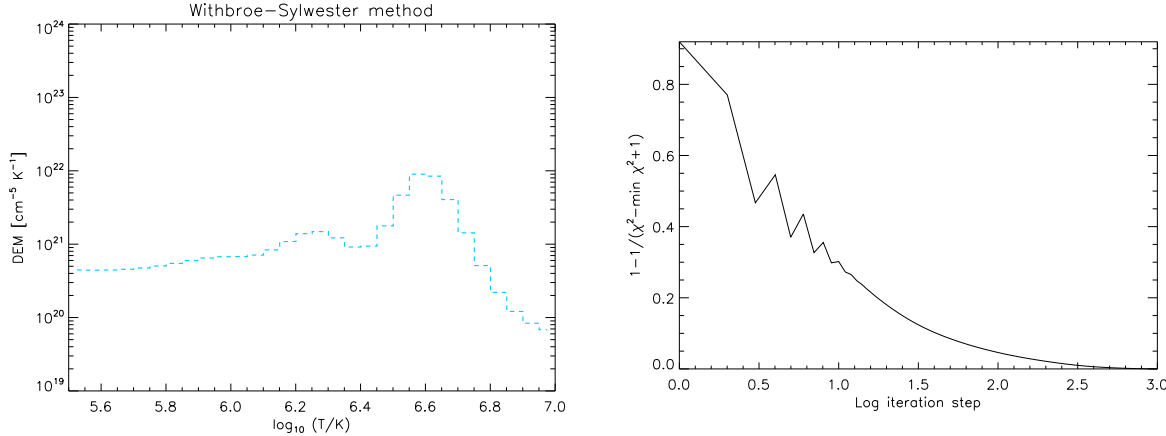
Figure 6.1: The DEM calculated by W-S method. The temperature step is $\log(T/\mathrm{K}) \sim 0.05$ (*left*). The convergence of this iterative method (*right*). The χ^2 in sufficient form is plotted for each iteration step. The input data is the same as in Fig. 6.4 and Table 6.1 for Maxwellian distribution.

10,000 iterations with limiting step 10 is shown in Fig. 6.1 (*right*). The set of programs written in IDL requiring SSW was used (Sylwester, private communication).

Hannah and Kontar (2012) present RIM that uses Tikhonov regularized inversion (Tikhonov, 1963; Craig, 1977; Prato et al., 2006) and generalized singular value decomposition (GSVD) (Hansen, 1992). The $DEM(T_j)$ [cm^{-5} K^{-1}], where $j = 1, ..., M$, is the solution of inversion of linear equations system:

$$g_i = \mathbf{K}_{i,j}\, DEM(T_j)\,, \tag{6.4}$$

which is generally ill-posed inverse problem and hence the last-square problem

$$\left\| \frac{\mathbf{K}\, DEM(T) - \mathbf{g}}{\delta \mathbf{g}} \right\|^2 = min\,, \tag{6.5}$$

does not have a unique solution. The integrated line intensity g_i for the specific wavelength i ($i = 1, ..., N$), spectral line contribution function $\boldsymbol{K}_{i,j}$ and error $\delta\mathbf{g}$ must be known. In the case $M = N$, a formal solution of Eq. 6.4 is $DEM(T_j) = \mathbf{K}_{i,j}^{-1} g_i$, where $\boldsymbol{K}^{-1}$ is the inverse of matrix $\boldsymbol{K}$. However, this solution is meaningless in all practical cases due to substantial noise amplification (Craig, 1977). The regularization approach is to add linear constraints to the DEM solution resulting in the specific problem being recast as

$$\|\tilde{\mathbf{K}}\, \xi(T) - \tilde{\mathbf{g}}\|^2 + \lambda \|\mathbf{L}(\xi(T) - \xi_0(T))\|^2 = min\,, \tag{6.6}$$
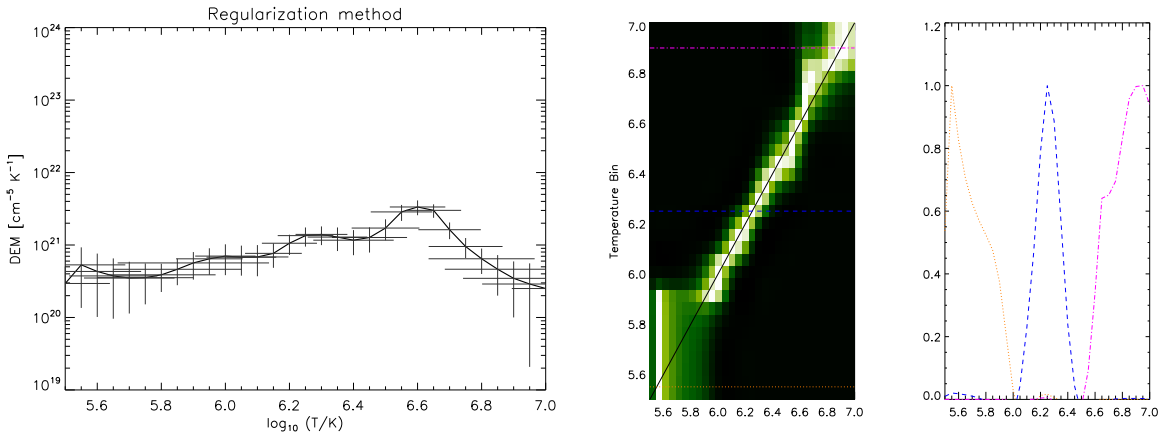
Figure 6.2: The DEM calculated by RIM. The temperature step is $\log(T/\mathrm{K}) \sim 0.05$ (*left*). The regularized solution matrix is almost diagonal over $\log(T/\mathrm{K}) \sim 5.9\text{-}6.9$ (*middle and right*). The input data is the same as in Fig. 6.4 and Table 6.1 for Maxwellian distribution.

where $\mathbf{L}$ is the constraint matrix, λ is the regularization parameter (related to the χ^2 of the solution), $\xi_0(T)$ is the initial guess solution, $\tilde{\mathbf{K}} = (\delta \mathbf{g})^{-1}\mathbf{K}$, and $\tilde{\mathbf{g}} = (\delta \mathbf{g})^{-1}\mathbf{g}$. The formal solution of Eq. 6.6 can be expressed in matrix form as a function of regularized parameter λ and GSVD is used to avoid time consuming matrix manipulations. Such solution is unique and well-behaved. The detailed explanation of RIM is presented in Hannah and Kontar (2012) and references therein.

These authors also compared their RIM with commonly used MCMC method (Kashyap and Drake, 1998) and showed a good match of these two methods using data of an active region core from Warren et al. (2011). However, the RIM is computationally faster, provides error bars also in temperature, and the regularized solution matrix allows us to easily determine the accuracy and robustness of the regularized DEM.

The example of calculated DEM using regularized method is shown in Fig. 6.2 (*left*) for active region core. The vertical (uncertainties in the data and contribution functions) and horizontal (temperature resolution) error bars are indicated. The regularized solution matrix, with each row, providing the temperature resolution information for each temperature T_j. It is also shown with the highlighted rows and FWHM estimation used for calculation of the temperature resolution (Fig. 6.2, *middle and right*). The online available IDL code of RIM requiring SSW was used (*http://www.astro.gla.ac.uk/ iain/demreg/*).

6.2   DEM analysis of active region cores and quiet Sun

Understanding of the temperature structure in the solar atmosphere is essential for the solution of the coronal heating problem. Different theories describing the origin of high-temperature plasma have to come hand-in-hand with the interpretation of the observed solar plasma emission. Thanks to recent space missions (see Chapter 1.2) we are able to diagnose plasma parameters in wide temperature range. Assumption, that distribution of electron energies should be different from generally used Maxwellian one, could lead to reinterpretation of some observation and specification of theories. The investigation of the influence of κ-distributions on the DEM is therefore an important step in understanding the temperature distribution in the solar corona if the plasma is non-Maxwellian.

Warren et al. (2012) selected 15 observations of inter-moss regions in active regions cores. The distribution of temperatures in such locations can constrain the properties of the coronal heating mechanism. For example, the slope of the DEM at temperatures lower than the DEM peak indicates whether the impulsive heating recurs on timescales longer or shorter than the typical plasma cooling time (see Viall and Klimchuk, 2011; Mulu-Moore et al., 2011; Tripathi et al., 2011; Winebarger, 2012). If the heating is high-frequency, in that it recurs often, the plasma cannot cool down. This is reflected on the DEM, which is strongly peaked, indicating plasma not far from equilibrium as was found by Warren et al. (2012): The emission measure (EM) distributions, defined as

$$EM(T) = DEM(T)\Delta T \equiv DEM(T)\frac{T\Delta(\log T)}{\log(\mathrm{e})} \; , \tag{6.7}$$

are indeed strongly peaked in the active region cores. The $EM(T)$ portions shortward of its peak were found to behave approximately as T^{α} with slopes $\alpha \gtrsim 2$. The high-temperature portions of the $EM(T)$ decrease as $T^{-\beta}$ with an even steeper $\beta \approx 5$–15. The properties of emission in the core of an active regions have been also studied by Warren et al. (2011), Winebarger et al. (2011), Tripathi et al. (2011), and Viall and Klimchuk (2011) under the assumption of Maxwellian distribution.

To study the influence of κ-distributions on the DEM reconstruction, we used the data of Warren et al. (2012) and Landi and Young (2010). These observations were obtained using EIS onboard the Hinode satellite and AIA onboard SDO (see Chapter 1.2). The EIS spectral range contains emission lines providing sufficient coverage of the 0.6 - 5 MK temperature range. The "cleaned" emission of Fe XVIII (Warren et al., 2012) observed by the AIA 94 Å channel is used

to constrain the DEM at high temperatures above 5 MK.

We reanalyzed three typical regions out of the 15 observed by Warren et al. (2012). These are regions 5, 8, and 14. We selected these regions because of their different low-temperature slopes α. Region 5 represents a region with one of the lowest α found, which is ≈ 2. Region 8 is a region with an intermediate α, and finally, region 14 has the highest $\alpha = 4.8 \pm 0.44$. The date and time of observation of these regions are displayed also with their position on the solar disk in Fig. 6.3. AIA 335 channel was chosen for these overview images since it highlights parts of the active regions with characteristic temperature $\log(T/\mathrm{K}) = 6.45$ (~ 2.8 MK). The images in Fig. 6.3 were processed with standard aia_prep software and a 500×500 arcsec regions were extracted with specified co-ordinates. The blue boxes represent the regions which were selected by Warren et al. (2012, Fig. 3) for the calculation of the emission measure distribution. The relevant EIS data were extracted from each spectral window and averaged together to create high signal-to-noise line profiles for each inter-moss region. The line profiles were fitted by single Gaussian. The selected EIS spectral lines and AIA 94 channel with observed intensities for region 5, 8, and 14 are listed in Tabs. 6.1 – 6.3. We estimate the typical uncertainties of observed intensities to be $\approx 30\%$ (Hannah and Kontar, 2012, Kontar, private communication). These contain the calibration error, which is at least 10% (Wang et al., 2011) or higher (Del Zanna, 2013b), atomic data errors, and errors arising from photon statistics. We note here that the RIM is still able to recover the DEM even if the calibration error is higher (Hannah and Kontar, 2012).

Landi and Young (2010) present a list of intensities of a quiet Sun (QS) region above the west limb observed by the Hinode/EIS instrument on 2007 April 13. We used these data to complement the analysis of the active region cores. The list of used spectral lines with their observed intensities is given in Table 6.4 for data by Landi and Young (2010). Note that these lines are formed in a rather narrow range of temperatures (Landi and Young, 2010).

Generally, in our analysis we use the fact, that the changes in synthetic intensities with κ are dominated by the ionization equilibrium, which exhibits wider and flatter ionization peaks, that can also be shifted to higher or lower temperatures (Dzifčáková, 2002; Dzifčáková and Dudík, 2013). Here, we have used the ionization equilibrium calculations of Dzifčáková and Dudík (2013) in conjunction with the atomic data from the CHIANTI database v7.1 (Landi et al., 2013). We have also assumed coronal abundances of Feldman et al. (1992) and constant pressure $N_{\mathrm{e}}T = 10^{15}$ cm^{-3} K for both Maxwellian and non-Maxwellian calculations. Coronal
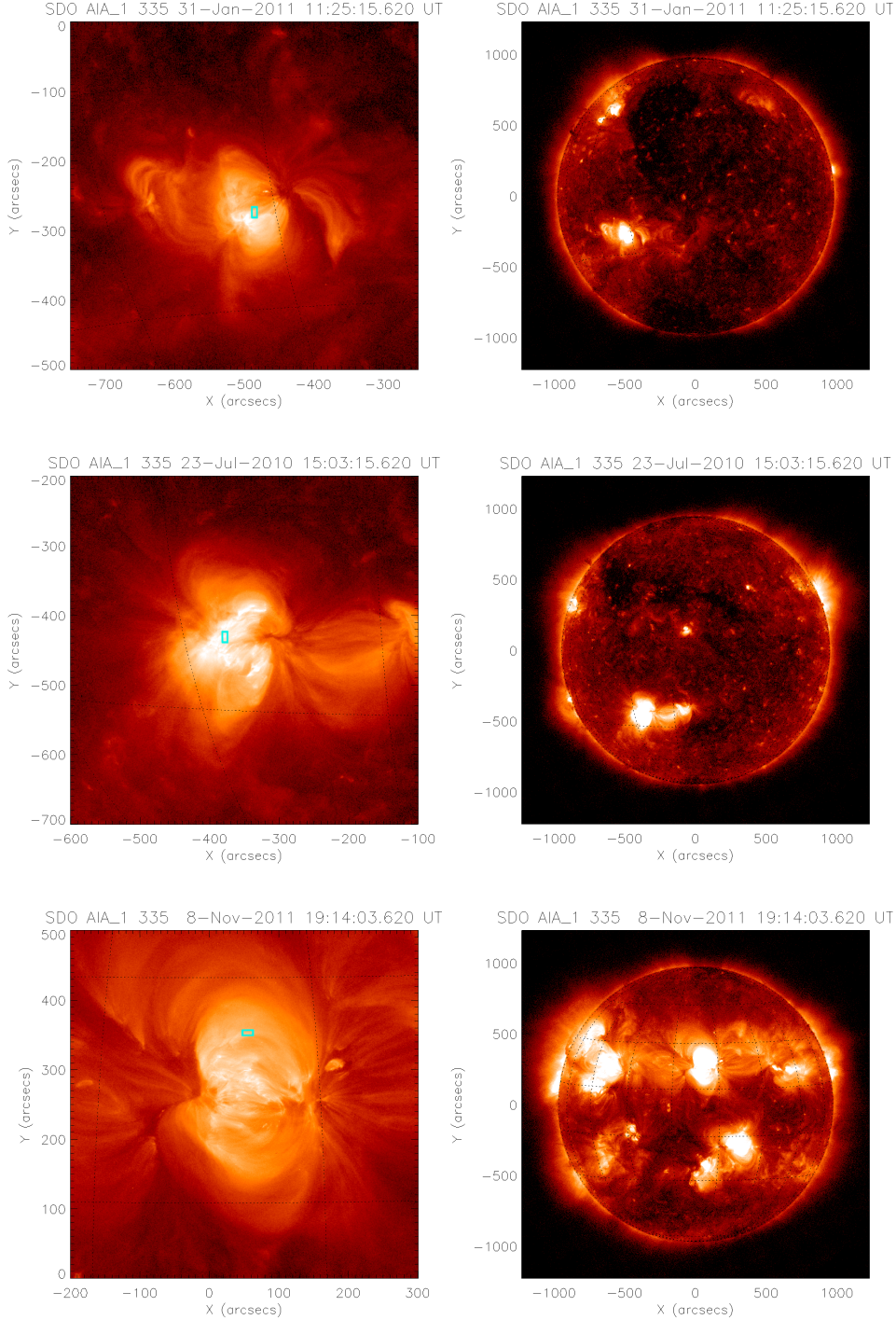
Figure 6.3: The overview of AIA full disc observations in 335 channel (right-hand panels) and extracted solar active regions (left-hand panels). The blue boxes indicate inter-moss regions which were investigated and correspond to region 5 (*top row*), region 8 (*middle row*), and 14 (*bottom row*). The input AIA data are available e.g. on *http://medoc-sdo.ias.u-psud.fr/*.

abundances are required for an adequate description of the active region cores, which exhibit enhancements of the low-FIP elements by about a factor of three (e.g., Del Zanna and Mason, 2003; Del Zanna, 2013b). The assumption of constant pressure is justified on grounds of the maximum height of the loops in the active region cores being much lower than the pressure scale-height for temperatures of $\log T\,(\mathrm{K}) \approx 6.6$ which are typical of active region cores. The lines used for the calculation of DEM are also typically not strongly sensitive to N_{e}, yielding little variation of the resulting DEM with the input value of pressure. We also note here that we have not been concerned in our work with the effects of finite density on the ionization equilibrium or the possible presence of the transient (time-dependent) ionization. The reasons are as follows. First, while the suppression of dielectronic recombination at high N_{e} (e.g., Summers et al., 2006; Nikolić et al., 2013) leads to shifts of the ionization peaks toward lower T, this effect is typically small at the temperatures corresponding to active region cores even for $\log N_{\mathrm{e}}\,(\mathrm{cm}^{-3}) = 10$ (Fig. 6 in Nikolić et al., 2013). The effect of κ-distributions on the ionization equilibrium can be much stronger. Second, active region cores typically exhibit only weak intensity fluctuations even on timescales of several hours (e.g., Antiochos et al., 2003; Brooks and Warren, 2009; Dudík et al., 2011a) indicating plasma near equilibrium. Therefore, we have believed that the presence of plasmas undergoing transient ionization (c.f., Doyle et al., 2013) can be neglected.

In general, it can be expected that the changes in the ionization equilibrium with κ-distributions (Fig. 3.2) could be reflected in the $G_{ji}(T, N_{\mathrm{e}}, \kappa)$ and reconstructed DEMs. However, it is by no means a priori clear whether the reconstructed DEMs should become broader with κ, as do the individual $G_{ji}(T, N_{\mathrm{e}}, \kappa)$ (see Chapter 3), or whether the DEMs may become more isothermal if the individual EM-loci curves shift toward a common crossing point. EM-loci(T) curve is defined as $I_{ji}^{\mathrm{obs}}/G_{ji}(T, N_{\mathrm{e}}, \kappa)$ and shows us the plasma multithermality. The EM-loci method was applied by Veck et al. (1984) for the first time.

To obtain an answer to this question, we have used the W-S method and RIM in conjunction with the calculated $G_{ji}(T, N_{\mathrm{e}}, \kappa)$ to reconstruct the DEMs for the selected datasets described in the previous section. To our knowledge, this is the first use of the DEM reconstruction methods for non-Maxwellian distributions (Mackovjak et al., 2014).

The reconstructed DEMs are converted to the $EM(T)$ using Eq. (6.7) and are shown in Fig. 6.4 for region 5, Fig. 6.6 for the region 8, and Fig. 6.8 for the region 14. In each one of these figures, the results are shown for the Maxwellian distribution with κ-distributions with

$\kappa = 5$, 3, and 2. Note that these figures also contain the EM-loci plots, which represent upper limits for the reconstructed $EM(T)$. The EM-loci plots are color-coded so that lines belonging to a particular element can be discerned at a glance. The results obtained from the RIM are plotted only for temperatures, where the DEMs were recovered reliably, specifically, where the resulting regularized solution matrix was almost diagonal. In contrast to that, the W-S method, which does not provide the errors in T, is plotted for the entire temperature range. The DEMs recovered for the Maxwellian distribution are similar to those of Warren et al. (2012), which are calculated by the MCMC method.

The DEMs recovered under the assumption of a κ-distribution indicate similar behavior of the DEM with κ for all three regions investigated. With decreasing κ or increasing departures from the Maxwellian distribution, the DEM peaks become more rotund (concave). Furthermore, while the Maxwellian DEMs peak near $\log T \,(\mathrm{K}) = 6.6 \,(\approx 4\,\mathrm{MK})$, the temperatures corresponding to DEM peaks for κ are shifted to a higher temperatures, reaching $\log T \,(\mathrm{K}) \sim 6.7\text{-}6.8$ for $\kappa = 2$. These temperatures are about $\approx 1\,\mathrm{MK}$ higher than for the Maxwellian distribution. The shift of the DEM peaks can be attributed to the behavior of ionization equilibrium with κ, where the ionization peaks of the coronal ions (ions formed at $\log T \,(\mathrm{K}) \gtrsim 6$) are typically shifted to higher T. This is also illustrated in Fig. 6.10, where we plot the product of the $G_{ji}(T, N_e \kappa)$ times $EM(T)$ for some of the observed lines. For low $\kappa = 2$, the lines are formed at higher T and in broader range of temperatures.

Note that it is not surprising that the DEM peaks are found at around $\log T \,(\mathrm{K}) = 6.6$ for the Maxwellian distribution (compare with Wood and Laming, 2013) and at slightly higher $\log T \,(\mathrm{K})$ for lower κ. Such temperatures correspond well to the minima of the radiative loss function for different κ (Dudík et al., 2011b). Even if the plasma is heated to higher T, radiative losses are least efficient at the temperatures corresponding to the minima of the radiative loss function.

Generally, we find a good agreement between the DEMs recovered using the RIM and W-S method. However, the RIM underestimates the peak emission and smooths it in comparison with the W-S method. This is due to several reasons. First, the errors of the input intensities I^{obs} are large, $\approx 30\%$, and the behavior of the RIM for such cases is known (Hannah and Kontar, 2012). In essence, large uncertainties in the EM-loci plots prevent the RIM from recovering sharply peaked DEMs, even if the plasma is truly isothermal. Second, the RIM tries to recover the DEM under the constraint of smallest total emission measure possible.
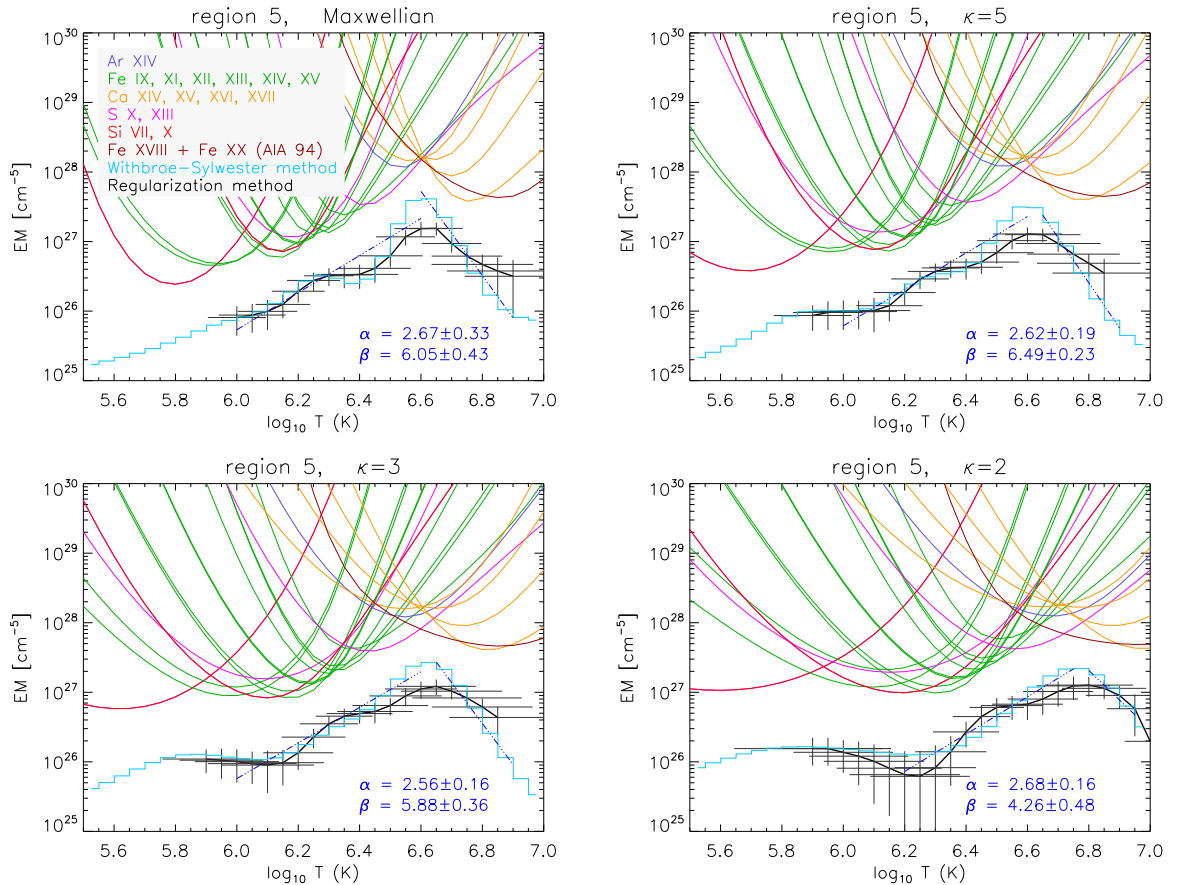
Figure 6.4: EM-loci plots (different colors stand for different ions) and the EM distributions for inter-moss region 5 using the W-S method (light blue line) and the RIM (thick black line). The RIM provide vertical and horizontal error bars. The EM(T) for Maxwellian distribution (*top left*) and κ-distribution with $\kappa = 5$ (*top right*), $\kappa = 3$ (*bottom left*), $\kappa = 2$ (*bottom right*) is shown. The slopes of EMs are indicated by dark blue linear fits. The power-law indexes α and β are listed.
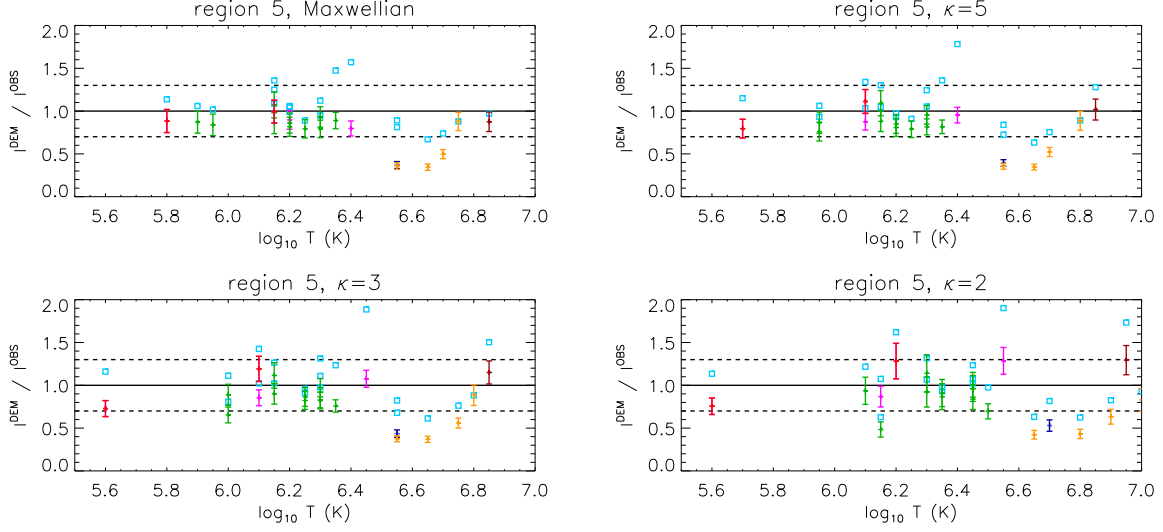
Figure 6.5: Calculated-to-observed intensities $I^{\mathrm{DEM}}/I^{\mathrm{obs}}$ for the DEM reconstructions of region 5 under the assumption of Maxwellian and $\kappa = 5$, 3, and 2 distributions. Light blue squares are for W-S method. Color points with error bars are for RIM. Color coding is the same as in the Fig 6.4. The horizontal dashed lines represent the 30% error of observed intensities.

As already noted, the Maxwellian DEM for region 5 is much more multithermal than the one for region 14. We perform fitting of both the low-temperature and high-temperature slopes of the recovered $EM(T)$. These fits are also shown in Figs. 6.4, 6.6, and 6.8, and the appropriate values of the slopes α and β are also listed in these figures. We find that the value of α does not change appreciably with κ, while the value of β is generally somewhat lower for lower κ. This is due to the rotundness of the EM peaks for low κ. We conclude that the assumption of a κ-distribution in DEM reconstruction does not significantly change the constraints on the coronal heating problem drawn from the steepness of the $EM(T)$ slopes.

The obtained consistent behavior of the reconstructed DEMs with κ for all three regions and two different DEM reconstruction methods establishes confidence in the reconstructed DEMs for the κ-distributions.

The ratios R of the observed and calculated intensities, $R = I^{\mathrm{DEM}}/I^{\mathrm{obs}}$, for the three regions, the Maxwellian and $\kappa = 2$ distributions are listed in Tables 6.1, 6.2, and 6.3. The I^{DEM} were calculated using W-S method and RIM. The ratios indicate the ability of the reconstructed DEMs to reproduce the observed intensities. Values of R within $0.7 < R < 1.3$ mean that I^{DEM} is within 30% of the estimated error of observed intensities. The relative error χ of reconstructed
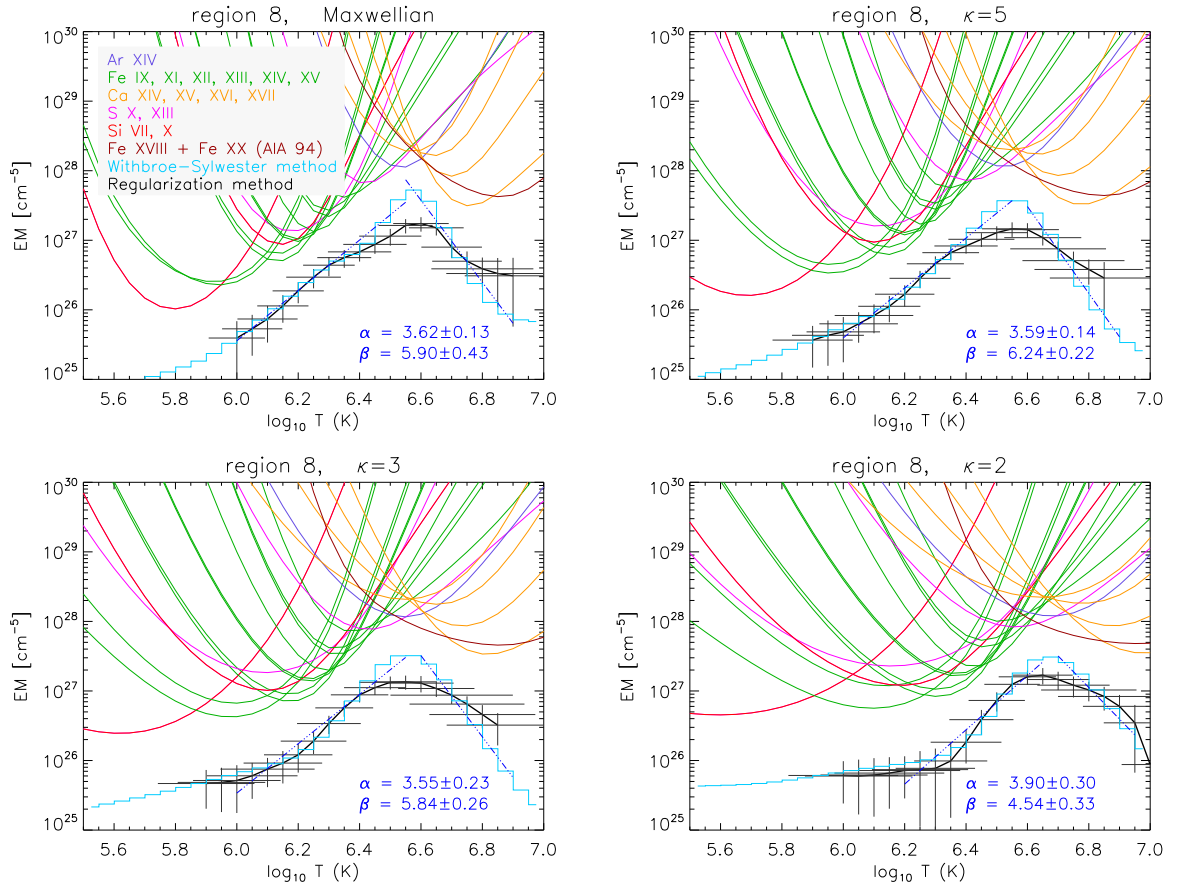
Figure 6.6: The same as Fig. 6.4 but for region 8.
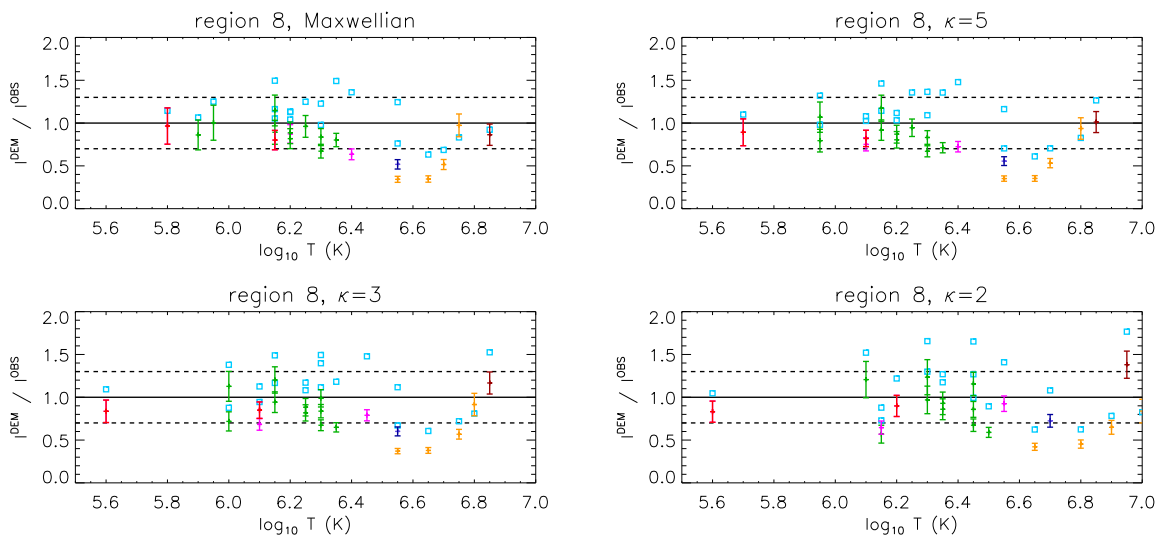
Figure 6.7: The same as Fig. 6.5 but for region 8.
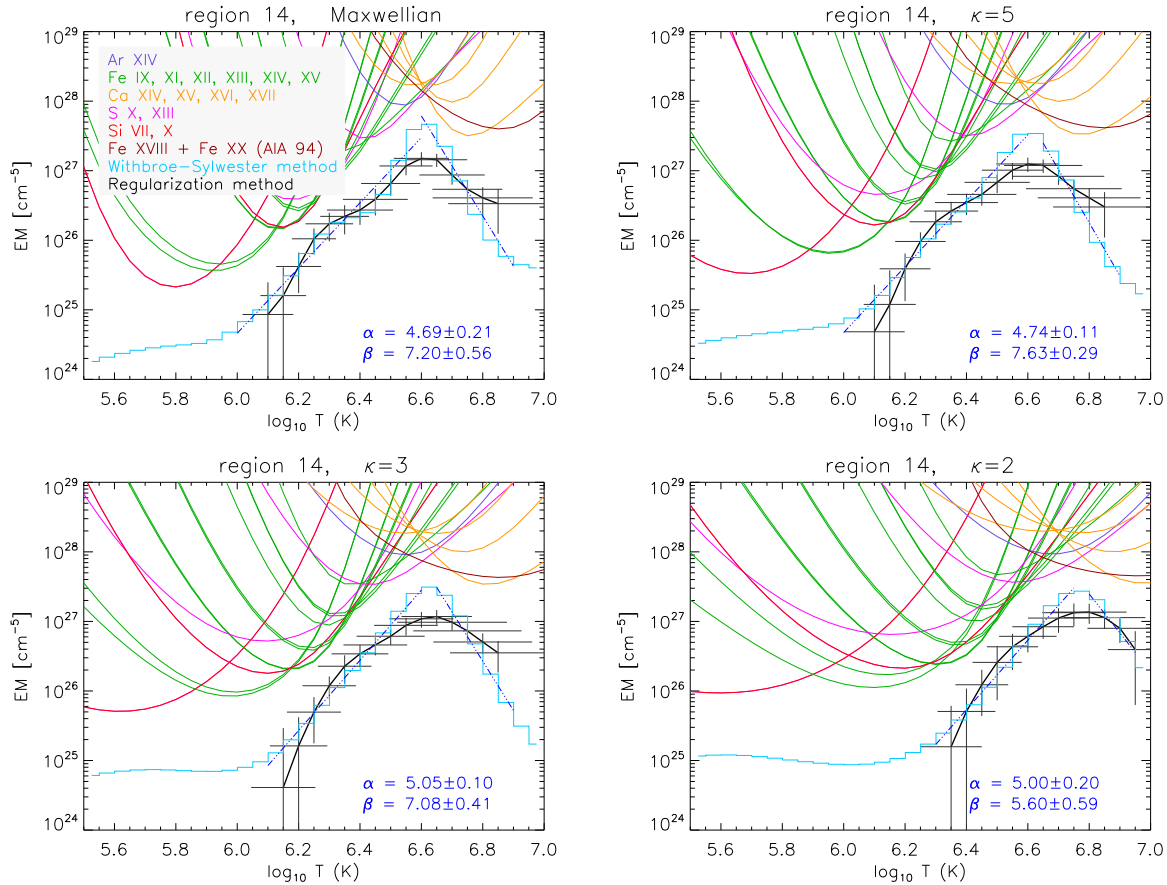
Figure 6.8: The same as Fig. 6.4 but for region 14.
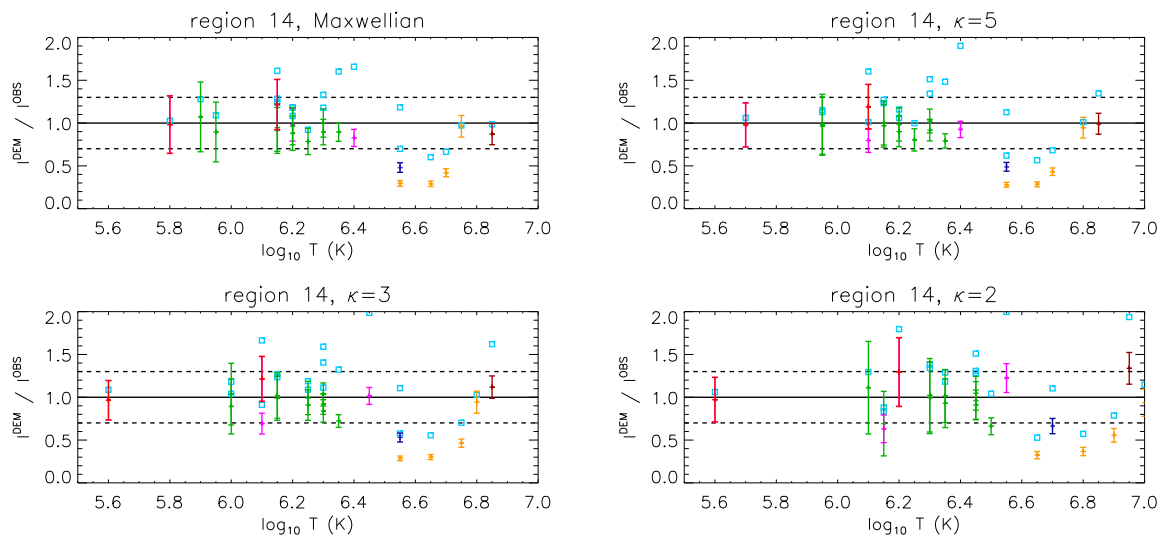

Figure 6.9: The same as Fig. 6.5 but for region 14.
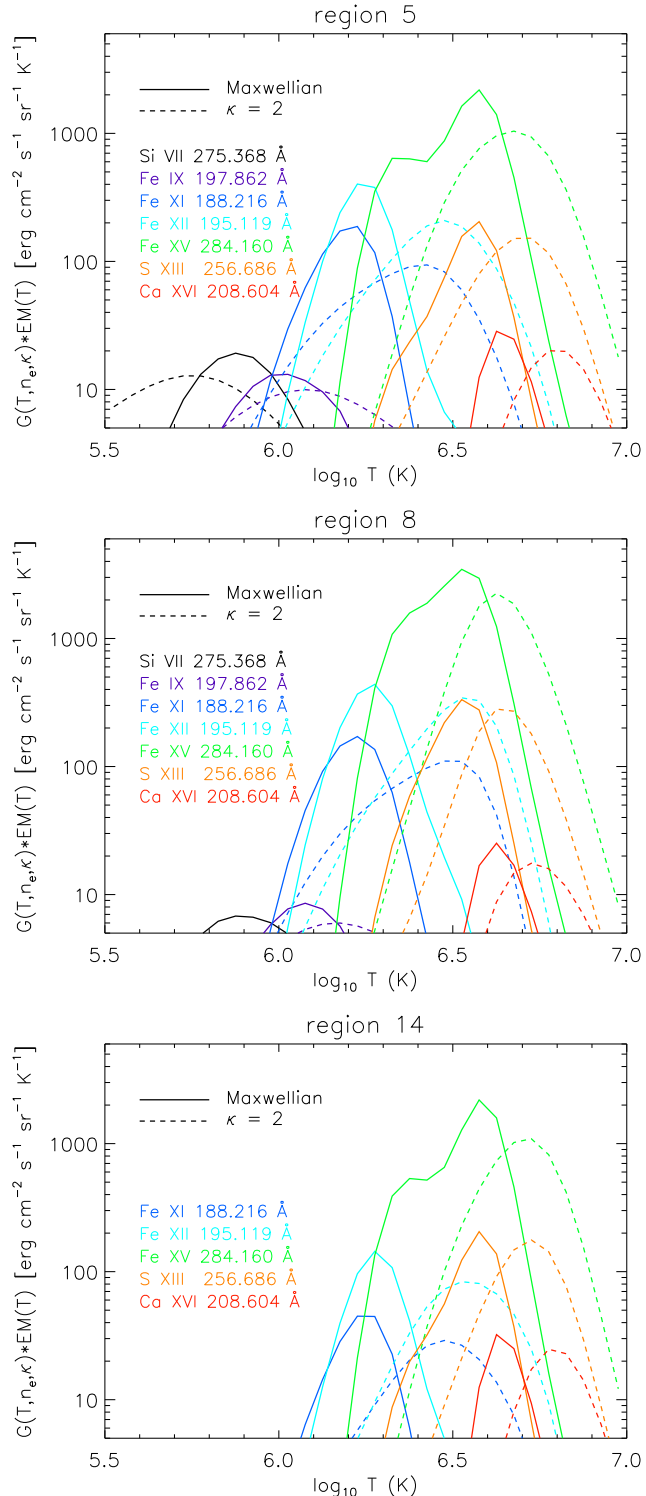
Figure 6.10: $G(T, n_e, \kappa) * EM(T)$ for the Maxwellian (solid lines) and for the κ-distributions with $\kappa = 2$ (dashed lines) for indicated lines formed in different temperature ranges for region 5 (*top*), region 8 (*middle*), and region 14 (*bottom*). The $EM(T)$ is calculated by W-S method.

Table 6.1: List of spectral lines used in reconstruction of DEM by W-S method and RIM with the values of I^{obs}, R_{Maxw}, and $R_{\kappa=2}$ are shown for inter-moss region 5. The EIS and AIA intensities have units erg cm^{-2} s^{-1} sr^{-1}.

Ion	$\lambda\,[\text{Å}]$	I^{obs}	W-S method		RIM	
			R_{Maxw}	$R_{\kappa=2}$	R_{Maxw}	$R_{\kappa=2}$
Si VII	275.37	99.8	1.14	1.13	0.88	0.76
Fe IX	188.50	129.	1.06	0.63	0.87	0.48
Fe IX	197.86	84.4	1.02	1.22	0.84	0.94
Fe XI	180.40	1135.	1.36	1.32	1.07	1.14
Fe XI	188.22	686.	1.09	1.07	0.86	0.92
S X	264.23	62.9	1.06	1.07	0.90	0.87
Si X	258.38	254.	1.25	1.62	0.99	1.28
Fe XII	192.39	439.	1.04	0.98	0.86	0.91
Fe XII	195.12	1431.	0.99	0.93	0.82	0.87
Fe XIII	202.04	1212.	0.89	1.07	0.79	0.96
Fe XIV	264.79	615.	0.95	1.02	0.79	0.84
Fe XIV	270.52	325.	1.12	1.24	0.93	1.01
Fe XV	284.16	6115.	1.47	0.98	0.89	0.70
S XIII	256.69	437.	1.57	1.90	0.80	1.29
Ar XIV	194.40	67.9	0.89	0.82	0.37	0.53
Ca XIV	193.87	242.	0.81	0.63	0.36	0.42
Ca XV	200.97	218.	0.67	0.62	0.35	0.43
Ca XVI	208.60	114.	0.74	0.83	0.50	0.63
Ca XVII	192.56	132.	0.88	0.93	0.88	0.83
Fe XVIII	AIA 94	628.	0.97	1.73	0.87	1.29
χ			0.23	0.35	0.30	0.30

DEM, as calculated from $\chi = \sqrt{\sum_i (1 - R_i)^2/N}$, are in the last row of Tables 6.1 - 6.3. For the W-S method, the χ is slightly better for Maxwellian distribution than for $\kappa = 2$. For RIM, they are 30% irrespective of the distribution.

The ratios R for both methods are also graphically presented in Figs. 6.5, 6.7, and 6.9. For RIM, errors of the $DEM(T)$ are propagated to obtain the errors $\sigma(I^{\text{DEM}})$ of the reconstructed intensities. These are shown as error bars for the corresponding R values. The ratios are typically within the interval $0.7 < R < 1.3$. Exceptions are ratios for lines formed at temperatures corresponding to the DEM peak. This is caused by the inability of the methods to exactly recover sharply peaked DEMs. Finally, we note that this type of error analysis is designed only

Table 6.2: The same as Table 6.1 but for region 8.

Ion	$\lambda\,[\text{Å}]$	I^{obs}	W-S method		RIM	
			R_{Maxw}	$R_{\kappa=2}$	R_{Maxw}	$R_{\kappa=2}$
Si VII	275.37	42.3	1.14	1.05	0.97	0.83
Fe IX	188.50	72.5	1.07	0.73	0.86	0.57
Fe IX	197.86	40.2	1.25	1.52	1.00	1.21
Fe XI	180.40	971.	1.49	1.66	1.15	1.23
Fe XI	188.22	602.	1.16	1.30	0.89	0.97
S X	264.23	74.2	1.13	0.88	0.87	0.65
Si X	258.38	312.	1.05	1.22	0.80	0.90
Fe XII	192.39	462.	1.13	1.27	0.89	0.93
Fe XII	195.12	1551.	1.04	1.18	0.82	0.86
Fe XIII	202.04	1294.	1.25	1.65	0.96	1.16
Fe XIV	264.79	1064.	0.98	0.99	0.67	0.67
Fe XIV	270.52	534.	1.23	1.27	0.84	0.86
Fe XV	284.16	10514.	1.49	0.89	0.80	0.59
S XIII	256.69	865.	1.36	1.41	0.63	0.92
Ar XIV	194.40	65.2	1.24	1.08	0.52	0.72
Ca XIV	193.87	317.	0.76	0.62	0.34	0.42
Ca XV	200.97	239.	0.63	0.62	0.35	0.45
Ca XVI	208.60	109.	0.69	0.78	0.52	0.65
Ca XVII	192.56	109.	0.83	0.82	0.97	0.84
Fe XVIII	AIA 94	620.	0.92	1.77	0.86	1.38
χ			0.25	0.36	0.30	0.30

to determine the goodness-of-fit for individual lines. It is not designed to determine which type of distribution and its corresponding DEM offer a better approximation for all of the observed intensities. These observed lines are not sufficient for diagnostics of κ either (see Chapter 4).

The DEM reconstruction is also performed on the quiet Sun data of Landi and Young (2010), and the results are presented in terms of $EM(T)$ in Fig. 6.11. For the Maxwellian distribution, the $EM(T)$ peaks at $\log T\,(\text{K}) = 6.15$ (1.4 MK). This is in good agreement with the results of Landi and Young (2010), although they used another iterative technique developed by Landi and Landini (1997) to determine the DEM. Note that outside of $\log T\,(\text{K}) \sim 6.0\text{-}6.3$ for the Maxwellian distribution, the regularized solution matrix was clearly not diagonal, producing

Table 6.3: The same as Table 6.1 but for region 14.

Ion	$\lambda\,[\text{Å}]$	I^{obs}	W-S method		RIM	
			R_{Maxw}	$R_{\kappa=2}$	R_{Maxw}	$R_{\kappa=2}$
Si VII	275.37	8.8	1.03	1.06	0.98	0.97
Fe IX	188.50	10.5	1.28	0.88	1.07	0.69
Fe IX	197.86	8.0	1.09	1.29	0.90	1.11
Fe XI	180.40	279.	1.28	1.38	0.95	1.02
Fe XI	188.22	139.	1.24	1.34	0.91	0.99
S X	264.23	21.1	1.18	0.83	0.98	0.63
Si X	258.38	55.0	1.61	1.80	1.22	1.29
Fe XII	192.39	128.	1.18	1.29	0.96	1.01
Fe XII	195.12	433.	1.08	1.18	0.88	0.93
Fe XIII	202.04	576.	0.92	1.28	0.79	0.96
Fe XIV	264.79	330.	1.18	1.31	0.89	0.91
Fe XIV	270.52	185.	1.33	1.51	1.00	1.05
Fe XV	284.16	4921.	1.60	1.04	0.89	0.66
S XIII	256.69	380.	1.66	2.00	0.83	1.22
Ar XIV	194.40	50.7	1.18	1.10	0.48	0.66
Ca XIV	193.87	282.	0.70	0.53	0.30	0.32
Ca XV	200.97	247.	0.60	0.57	0.29	0.37
Ca XVI	208.60	127.	0.66	0.79	0.42	0.56
Ca XVII	192.56	110.	0.97	1.15	0.96	0.94
Fe XVIII	AIA 94	583.	0.99	1.94	0.87	1.34
χ			0.32	0.44	0.30	0.30

large horizontal errors. This means that the DEM calculated by the RIM is not reliable at these temperatures and is again not displayed.

For κ-distributions, the $EM(T)$ peak is again shifted progressively to higher T, reaching $\log T\,(\text{K}) \approx 6.3$ (2 MK) for $\kappa=2$. Note that while the EM-loci plots indicate multithermal plasma for the Maxwellian distribution, they indicate progressively less multithermal plasma for lower κ. Especially for $\kappa=2$, the EM-loci curves nearly intersect at a common point (Fig. 6.11, *bottom right*). Consequently, it is possible to interpret the same observed spectrum either as emission from multithermal plasma with a narrow DEM and Maxwellian distribution, or as emission from near-isothermal plasma with $\kappa=2$. Indeed, upon fitting the EM slopes, we find that the value of α progressively increases from 3.66 ± 0.15 for the Maxwellian distribution to 5.77 ± 0.31 for $\kappa=2$. It is, however, not clear what coronal heating mechanism could produce
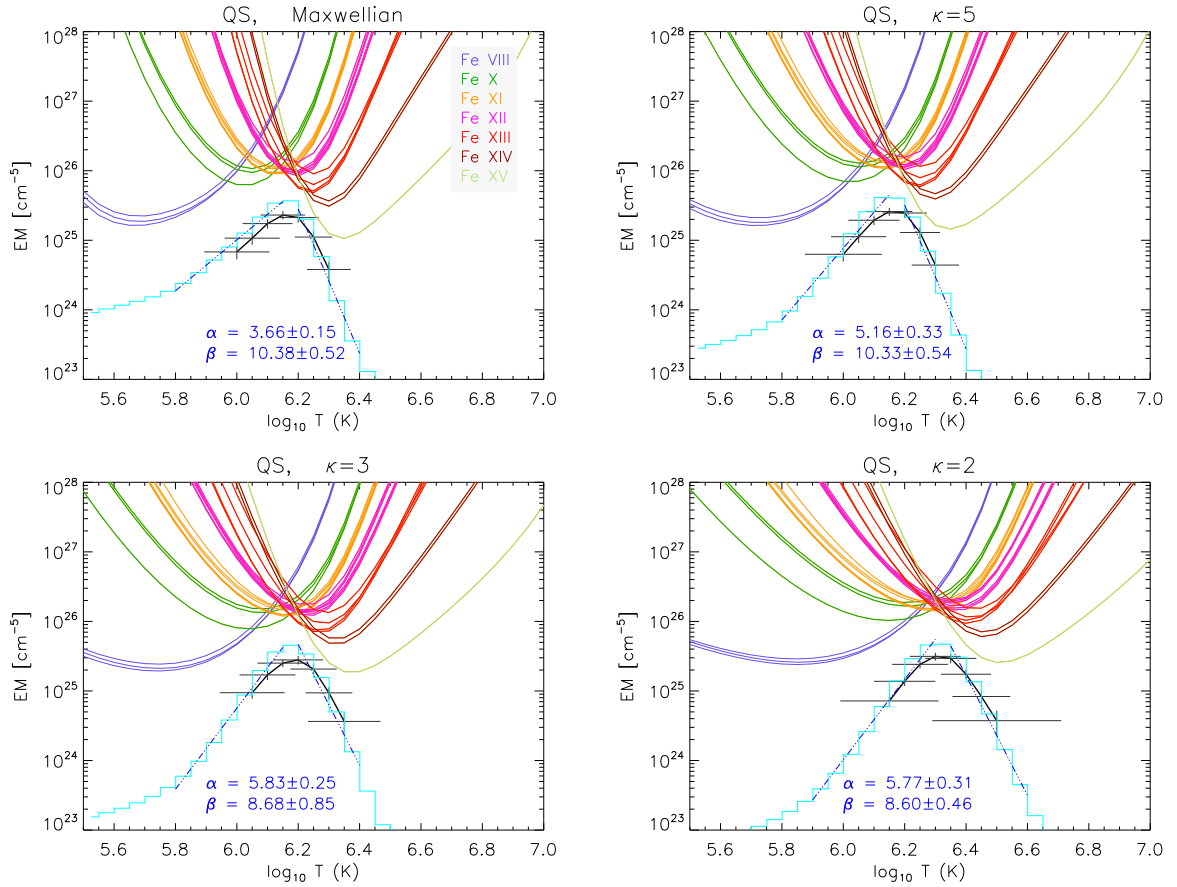
Figure 6.11: The same as Fig. 6.4 but for quiet Sun region.
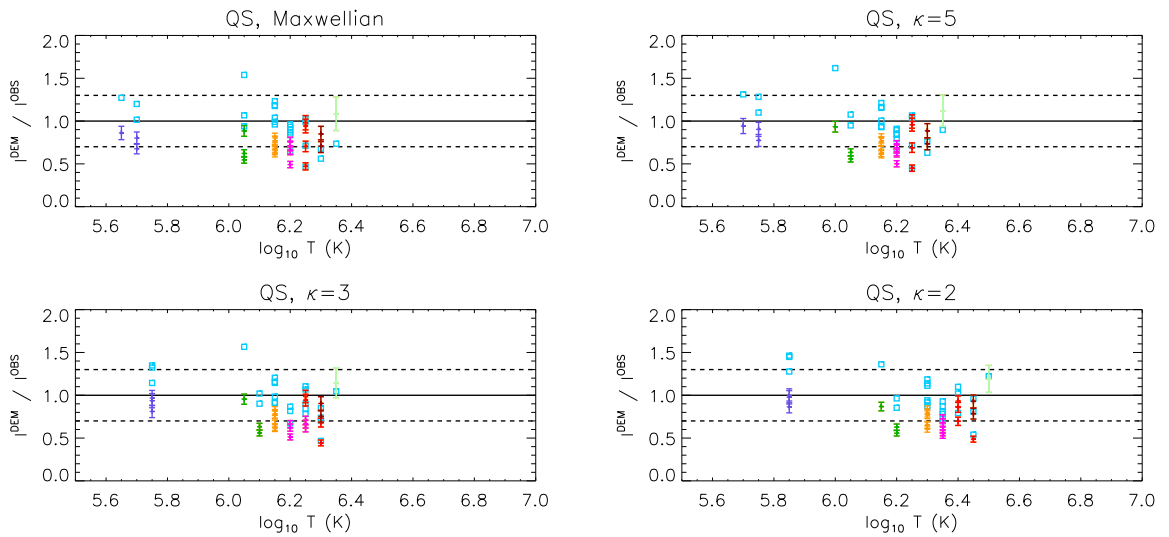
Figure 6.12: The same as Fig. 6.5 but for quiet Sun region.

Table 6.4: The list of spectral lines from Landi and Young (2010) used in the reconstruction of DEM by W-S method and RIM. The I^{obs}, R_{Maxw}, and $R_{\kappa=2}$ are shown. The Hinode/EIS intensities have units erg cm^{-2} s^{-1} sr^{-1}.

Ion	$\lambda\,[\text{Å}]$	I^{obs}	W-S method		RIM	
			R_{Maxw}	$R_{\kappa=2}$	R_{Maxw}	$R_{\kappa=2}$
Fe VIII	185.21	14.6	1.20	1.45	0.80	0.98
Fe VIII	186.60	11.0	1.01	1.28	0.68	0.86
Fe VIII	194.66	3.90	1.27	1.46	0.86	0.99
Fe X	174.53	244.	1.07	0.96	0.62	0.63
Fe X	175.26	18.0	1.54	1.36	0.88	0.87
Fe X	177.24	153.	0.94	0.85	0.55	0.56
Fe XI	178.06	9.10	1.04	0.94	0.68	0.65
Fe XI	180.40	208.	0.99	0.92	0.65	0.65
Fe XI	180.59	7.50	1.18	1.14	0.77	0.79
Fe XI	181.13	10.1	1.23	1.19	0.80	0.83
Fe XI	182.17	35.6	0.96	0.87	0.62	0.61
Fe XI	201.73	5.70	1.18	1.11	0.76	0.77
Fe XII	186.89	24.9	0.93	0.78	0.71	0.59
Fe XII	192.39	46.6	0.84	0.81	0.66	0.63
Fe XII	193.51	85.0	0.96	0.93	0.75	0.73
Fe XII	195.12	134.	0.90	0.87	0.71	0.68
Fe XII	196.12	8.50	0.87	0.74	0.66	0.56
Fe XII	249.39	5.70	0.64	0.70	0.49	0.53
Fe XIII	202.04	87.3	0.46	0.54	0.47	0.49
Fe XIII	203.16	3.20	1.02	1.10	0.98	0.93
Fe XIII	203.83	20.3	0.99	1.02	0.94	0.86
Fe XIII	204.94	5.80	0.71	0.79	0.70	0.70
Fe XIV	270.52	7.50	0.68	0.96	0.85	0.93
Fe XIV	274.20	19.4	0.56	0.81	0.71	0.79
Fe XV	284.16	26.8	0.73	1.22	1.09	1.19
χ			0.24	0.23	0.30	0.30

such extremely non-Maxwellian distributions in the quiet Sun.

The ratios R of the calculated-to-observed intensities, $R = I^{\mathrm{DEM}}/I^{\mathrm{obs}}$, are presented in Table 6.4. The I^{DEM} were calculated using W-S method and RIM. The plots of the calculated-to-observed intensities ratios are shown in Fig. 6.12.

6.3 Temperature structure of prominence-corona transition region

We also investigated the influence of the κ-distributions on the DEM of the prominence-corona transition region (PCTR), where the temperature range of line formation is wider than in previous cases. The observed line intensities from SOHO/SUMER spectrometer (see Chapter 1.2) listed in Parenti and Vial (2007) as A_1 were used. The ionization equilibria for κ-distributions were taken from Dzifčáková and Dudík (2013) and the excitation equilibrium was calculated for atomic data corresponding to the CHIANTI 6 (Dere et al., 2009). The contribution function for κ-distributions were calculated by modification (Dzifčáková, 2006b; Dzifčáková and Mason, 2008) of CHIANTI. We have used coronal abundances of Feldman et al. (1992) and constant pressure $N_{\mathrm{e}}T = 10^{14}$ cm^{-3} K. The DEM was calculated using the W-S method only. The differences between our reconstructed DEM for the Maxwellian distribution with original DEM by Parenti and Vial (2007) (Fig. 6.13, top left) should be a result of different calculation methods and different ionization equilibrium.

The DEM's calculated for the κ-distributions are again wider and flatter in comparison with DEM for the Maxwellian distribution (Fig. 6.13, top right; bottom left). This is also mainly the result of changes in the ionization equilibrium for the κ-distributions, where the ionization peaks are wider and shifted in comparison with the Maxwellian distribution (Dzifčáková and Dudík, 2013). For the κ-distributions, the spectral lines are formed in wider temperature ranges and the maxima of contribution to the line intensities can be substantially shifted to lower T, especially in transition region (Fig. 6.13, bottom right). These changes could affect the temperature region that is visible in SDO/AIA filters. For the AIA 171 and 193 filters, and Fe X - XII lines (Fig. 6.14), the maxima of contributions to the line intensity have similar positions for both Maxwellian and κ-distributions. However, the Fe IX and Fe VIII lines show enhanced low-temperature contributions and the contributions from O V and O VI lines, formed at even lower temperatures, are significantly widened. We can conclude that the κ-distributions allow to see wider temperature range in AIA filters than the Maxwellian one. This is an another example of the demand to diagnose the κ-distributions in the observed coronal and transition region plasma. The interpretation of emission observed by SDO/AIA in a such way could be dependent on the value of κ.
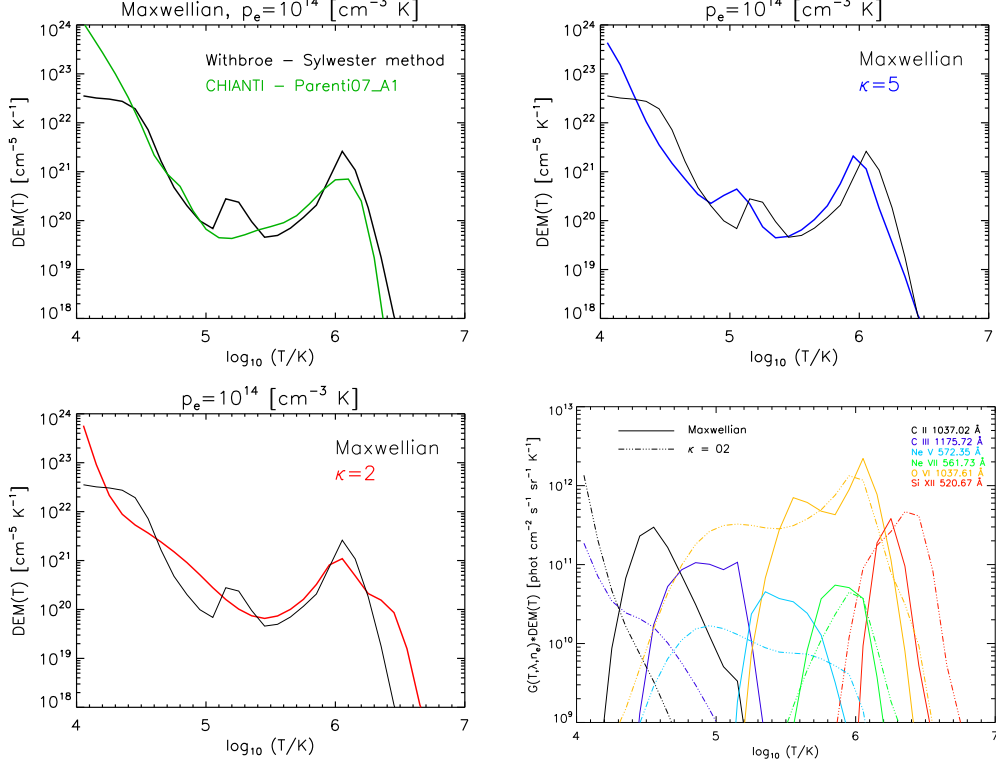
Figure 6.13: *Top left:* The PCTR DEM for the Maxwellian distribution by Parenti and Vial (2007) (green line) and by Withbroe-Sylwester method (black line). *Top right:* DEM for the κ-distribution with $\kappa = 5$ (blue line). *Bottom left:* DEM for the κ-distribution with $\kappa = 2$ (red line). *Bottom right:* $G(T, \lambda, n_e) * \text{DEM}$ for the Maxwellian (full lines) and for the κ-distributions with $\kappa = 2$ (dot-dot-dot dashed lines) for six lines formed in different temperature ranges.
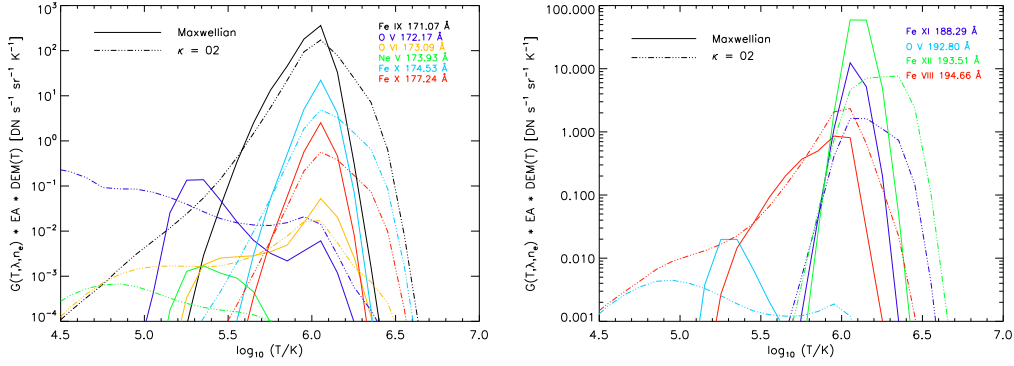

Figure 6.14: $G(T, \lambda, n_e) * \text{DEM}$ multiplied by the effective area (EA) of 171 (*left*) and 193 band (*right*) for the Maxwellian (full lines) and κ-distribution with $\kappa = 2$ (dot-dot-dot dashed lines).

Chapter 7

Summary and Conclusions

We have studied the effects of the non-Maxwellian κ-distributions on the intensities of the spectral lines originating in the solar transition region and the solar corona.

In chapters 1, 2 and 3 we introduced theoretical background for our investigation. In Chapter 1 we introduced basic information about solar upper atmosphere and its observations. Theory and detections of the κ-distributions are described in Chapter 2. The solar spectroscopy and effects of the κ-distributions on the ionization and excitation equilibrium are presented in Chapter 3.

In Chapter 4, we analyzed the possibilities to diagnose the non-Maxwellian κ-distributions using the Al, Ar, Ca, Mg, Ni, O, S, and Si lines observed by the Hinode/EIS spectrometer. From these lines, only Ca, Ni, S, and O lines provide opportunities to determine the value of κ. We discussed the dependence of these κ-sensitive line ratios on the electron density and assessed the presence of possible blends and their elimination. Generally, the line ratios belonging to ions in different ionization stages offer greater diagnostic capabilities. The line ratios of O IV ion are a notable exception. This is the only ion whose lines are density-insensitive and thus also offers diagnostics of κ independent of the electron density. However, simultaneous diagnostics of both temperature and κ is not unique for the entire temperature range. To test the proposed diagnostic methods, the predicted line ratios were compared with the observed line ratios by Brown et al. (2008) in different solar regions. The observed line ratio O IV $(207.18 + 207.24\,\text{Å}) \, / \,$ O IV $279.93\,\text{Å}$ does not correspond to the Maxwellian distribution. However, these lines are blended by Mg IX lines. These blends cannot be removed using EIS observations alone. The observed S X ratios for the limb region suggests $\kappa \leq 3$. However, the limb region is also likely to be multithermal and the error due to photon statistics is large. The data of Brown et al. (2008)

are not really appropriate for determination of the value of κ.

We also investigated the influence of κ on the density diagnostics using the line ratios of S x, S xi, Si x, Ar xiv, and Ni xvi proposed by Young (2007). We have found that S x 196.81 Å / 264.23 Å and Si x 261.06 Å / 258.37 Å are not suitable for density diagnostics if the electrons are described by a κ-distribution. We failed to diagnose density from the remaining S x and Ar xiv lines since the observed ratios were higher than the theoretical ranges. This indicates the presence of blends, that are either unknown or cannot be removed due to missing data. Therefore, we used Fe line ratios for this purpose. Typically, the diagnosed densities are lower by ≈ 0.1 dex for the κ-distribution than the densities diagnosed for the Maxwellian distribution. This is due to changes in the ionization and excitation equilibria with κ. The total errors in the determination of density can be up to ≈ 0.3 dex if the temperature of the emitting plasma is unknown.

The suggested diagnostics methods were tested in Chapter 5 on dataset from own observation proposed for Hinode/EIS. Data reduction was performed and individual steps therein were described. We selected coronal loop and provided diagnostics of its plasma parameters. We found that all plasma parameters diagnosed using different line ratios were almost consistent. The uncertainties in the precision indicate the presence of unknown blends or multithermality of selected structure or unpredicted errors in atomic data. Our study also shown that the observations with higher precision and better spectral resolution, than Hinode/EIS could offer in present time, are needed for a such analysis. Nevertheless, the diagnosed results shown that the investigated plasma is unlikely to be Maxwellian and this is an important result and motivation for future research.

In Chapter 5 we investigated the temperature structure of several active region cores and a quiet Sun region under the assumption of the non-Maxwellian κ-distributions. To recover the differential emission measure, we used two methods, namely the Withbroe-Sylwester method and the regularization method. We demonstrated that both DEM reconstruction methods give similar solutions. This gives confidence in the validity of the reconstructed DEMs. The reconstructed Maxwellian DEMs for three active region cores and quiet Sun region are in good qualitative agreement with results published by other authors, who use different DEM reconstruction techniques. We shown that the influence of κ-distributions on the DEMs is similar for each of the three active region cores studied. With decreasing κ, the DEMs become more rotund and their peaks are shifted to higher temperatures. This is chiefly a consequence of changes

in ionization equilibrium, which also lead to individual lines being formed at wider range of temperatures. The slopes of the EM distributions leftward of its peak do not change appreciably with κ. This suggests that different assumptions on the shape of the electron distribution function do not change the constraints on the coronal heating mechanism. Interpretation of quiet Sun plasma emission may differ for different types of electron distribution assumed. The DEM is found to be multithermal for Maxwellian distribution, but is much less multithermal for $\kappa \approx 2$.

Our results show that the multithermality of plasma can be a robust result, although the degree of the multithermality is dependent on the region observed and assumed particle distribution. Especially in the active region cores, some constraints on the coronal heating can be derived from DEM reconstruction regardless of the particle microphysics. For example, the relative number of high-energy electrons produced by the coronal heating. This is a somewhat surprising result, since the contribution functions of the individual spectral lines are highly dependent on the assumed distribution function.

This dependency of the line intensities on the shape of the energy distribution calls for a closer scrutiny of the spectroscopic observations. A positive diagnostics of the non-Maxwellian distributions in the solar corona would be a "smoking gun" for the coronal heating process involved and could possibly help explain the source of the solar wind. Unfortunately, the present spectroscopic observations have limited wavelength coverages and often suffer from instrument and calibration issues preventing the diagnostics, as well as atomic data uncertainties. A comprehensive search for lines suitable for diagnostics of non-Maxwellian distributions in the entire wavelength range is planned. This is important for the interpretation of current and future observations and could also result in improved instrument design.

Resumé

Vo vedeckej praxi sa bežne používa predpoklad, že v slnečnej atmosfére sú prítomné Maxwellove distribúcie energií častíc. Za posledných 40 rokov však bolo publikovaných množstvo prác, ktoré priamo poukazujú na prítomnosť ne-maxwellovských κ-distribúcií v rozličných formách vesmírnej plazmy. Na to, aby boli κ-distribúcie uvažované aj pri analýze dát z pozorovaní slnečnej koróny, musia byť najprv jednoznačne diagnostikované v tomto prostredí.

Predkladaná dizertačná práca sa venuje diagnostike κ-distribúcií v slnečnej koróne a prechodovej oblasti. V práci sme rozšírili diagnostické metódy, ktoré boli navrhnuté v článku Dzifčáková and Kulinová (2010), pre ióny Fe. Venovali sme sa možnostiam diagnostiky z pomerov intenzít spektrálnych čiar ostatných prvkov. Tiež sme navrhli špecifické pozorovanie na satelite Hinode/EIS, ktorého výsledky ukázali, že distribúcia skúmanej plazmy nezodpovedá Maxwellovej distribúcii elektrónov. Zaoberali sme sa aj štúdiom diferenciálnej emisnej miery (DEM) a jej zmenám, ktoré by boli vyvolané prítomnosťou κ-distribúcií. Ukázali sme, že s klesajúcou hodnotou κ sa DEM pík posúva k vyšším teplotám a stáva sa širším. Tento poznatok je veľmi potrebný pri analýze teplotnej štruktúry skúmanej plazmy.

Práca je rozdelená do siedmych kapitol. V 1. kapitole sú uvedené základné informácie o hornej slnečnej atmosfére. Predstavené sú aj prístroje na jej pozorovanie, ktoré využívame v našej práci. V 2. kapitole ponúkame prehľad úspešných detekcií κ-distribúcií v kozmickej plazme a tiež uvádzame hlavné vlastnosti κ-distribúcií. V 3. kapitole definujeme základné vzťahy a procesy na výpočet EUV spektra za predpokladu κ-distribúcií. V ďalších kapitolách sa už venujeme nášmu originálnemu výskumu. V 4. kapitole predstavujeme metódy na diagnostiku hustoty, typu distribúcie a teploty z intenzít spektrálnych čiar, ktoré patria iónom Al, Ar, Ca, Mg, Ni, O, S a Si. Uvádzame pomery vhodné na diagnostiku a detailne diskutujeme ich použiteľnosť. Keďže ide o málo intenzívne čiary, navrhli sme špecifické pozorovanie na satelite Hinode/EIS. Výsledky z tohoto pozorovania sú prezentované v 5. kapitole. Z dôvodu

poškodenia detektora sme však boli schopní použiť na diagnostiku iba dostatočne intenzívne Fe čiary. Výsledky ukázali, že diagnostikovaná distribúcia nie je maxwellovská. V 6. kapitole študujeme vplyv κ-distribúcií na výpočítanú DEM. Zaoberali sme sa štúdiom emisie troch aktívnych oblastí, oblasti pokojného Slnka a štúdiom plazmy protumberančnej koróny a prechodovej oblasti. Všetky závery sú zhrnuté v poslednej kapitole.

Najdôležitejšie výsledky práce boli počas doktorandského štúdia prezentované na viacerých medzinárodných konferenciách a tiež boli publikované ako dva samostatné články v zahraničných karentovaných časopisoch (Mackovjak et al., 2013, 2014).

Bibliography

Antiochos, S. K., Karpen, J. T., DeLuca, E. E., Golub, L. and Hamilton, P. (2003), 'Constraints on Active Region Coronal Heating', *Astrophys. J.* **590**, 547–553.

Aschwanden, M. J., Nitta, N. V., Wuelser, J.-P. and Lemen, J. R. (2008), 'First 3D Reconstructions of Coronal Loops with the STEREO A+B Spacecraft. II. Electron Density and Temperature Measurements', *Astrophys. J.* **680**, 1477–1495.

Badnell, N. R., O'Mullane, M. G., Summers, H. P., Altun, Z., Bautista, M. A., Colgan, J., Gorczyca, T. W., Mitnik, D. M., Pindzola, M. S. and Zatsarinny, O. (2003), 'Dielectronic recombination data for dynamic finite-density plasmas. I. Goals and methodology', *Astron. Astrophys.* **406**, 1151–1165.

Brooks, D. H. and Warren, H. P. (2009), 'Flows and Motions in Moss in the Core of a Flaring Active Region: Evidence for Steady Heating', *Astrophys. J. Lett.* **703**, L10–L13.

Brooks, D. H., Warren, H. P. and Ugarte-Urra, I. (2012), 'Solar Coronal Loops Resolved by Hinode and the Solar Dynamics Observatory', *Astrophys. J. Lett.* **755**, L33.

Brooks, D. H., Warren, H. P. and Young, P. R. (2011), 'EUV Spectral Line Formation and the Temperature Structure of Active Region Fan Loops: Observations with Hinode/EIS and SDO/AIA', *Astrophys. J.* **730**, 85.

Brown, C. M., Feldman, U., Seely, J. F., Korendyke, C. M. and Hara, H. (2008), 'Wavelengths and Intensities of Spectral Lines in the 171-211 and 245-291 Å Ranges from Five Solar Regions Recorded by the Extreme-Ultraviolet Imaging Spectrometer (EIS) on Hinode', *Astrophys. J. Suppl. Ser.* **176**, 511–535.

Brown, J. C. (1971), 'The Deduction of Energy Spectra of Non-Thermal Electrons in Flares from the Observed Dynamic Spectra of Hard X-Ray Bursts', *Solar Phys.* **18**, 489–502.

Cirtain, J. W., Golub, L., Winebarger, A. R., de Pontieu, B., Kobayashi, K., Moore, R. L., Walsh, R. W., Korreck, K. E., Weber, M., McCauley, P., Title, A., Kuzin, S. and Deforest, C. E. (2013), 'Energy release in the solar corona from spatially resolved magnetic braids', *Nature* **493**, 501–503.

Collier, M. R. and Hamilton, D. C. (1995), 'The relationship between kappa and temperature in energetic ion spectra at Jupiter', *Geophys. Res. Lett.* **22**, 303–306.

Collier, M. R., Hamilton, D. C., Gloeckler, G., Bochsler, P. and Sheldon, R. B. (1996), 'Neon-20, Oxygen-16, and Helium-4 densities, temperatures, and suprathermal tails in the solar wind determined with WIND/MASS', *Geophys. Res. Lett.* **23**, 1191–1194.

Craig, I. J. D. (1977), 'The use of a-priori information in the derivation of temperature structures from X-ray spectra', *Astron. Astrophys.* **61**, 575–590.

Craig, I. J. D. and Brown, J. C. (1976), 'Fundamental limitations of X-ray spectra as diagnostics of plasma temperature structure', *Astron. Astrophys.* **49**, 239–250.

Craig, I. J. D. and Brown, J. C. (1986), *Inverse problems in astronomy: A guide to inversion strategies for remotely sensed data.*

Culhane, J. L., Harra, L. K., James, A. M., Al-Janabi, K., Bradley, L. J., Chaudry, R. A., Rees, K., Tandy, J. A., Thomas, P., Whillock, M. C. R., Winter, B., Doschek, G. A., Korendyke, C. M., Brown, C. M., Myers, S., Mariska, J., Seely, J., Lang, J., Kent, B. J., Shaughnessy, B. M., Young, P. R., Simnett, G. M., Castelli, C. M., Mahmoud, S., Mapson-Menard, H., Probyn, B. J., Thomas, R. J., Davila, J., Dere, K., Windt, D., Shea, J., Hagood, R., Moye, R., Hara, H., Watanabe, T., Matsuzaki, K., Kosugi, T., Hansteen, V. and Wikstol, Ø. (2007), 'The EUV Imaging Spectrometer for Hinode', *Solar Phys.* **243**, 19–61.

Decker, R. B. and Krimigis, S. M. (2003), 'Voyager observations of low-energy ions during solar cycle 23', *Advances in Space Research* **32**, 597–602.

Decker, R. B., Krimigis, S. M., Roelof, E. C., Hill, M. E., Armstrong, T. P., Gloeckler, G., Hamilton, D. C. and Lanzerotti, L. J. (2005), 'Voyager 1 in the Foreshock, Termination Shock, and Heliosheath', *Science* **309**, 2020–2024.

DeForest, C. E. (2007), 'On the Size of Structures in the Solar Corona', *Astrophys. J.* **661**, 532–542.

Del Zanna, G. (2013*a*), 'A revised radiometric calibration for the Hinode/EIS instrument', *Astron. Astrophys.* **555**, A47.

Del Zanna, G. (2013*b*), 'The multi-thermal emission in solar active regions', *Astron. Astrophys.* **558**, A73.

Del Zanna, G. and Mason, H. E. (2003), 'Solar active regions: SOHO/CDS and TRACE observations of quiescent coronal loops', *Astron. Astrophys.* **406**, 1089–1103.

Del Zanna, G., O'Dwyer, B. and Mason, H. E. (2011), 'SDO AIA and Hinode EIS observations of "warm" loops', *Astron. Astrophys.* **535**, A46.

Dere, K. P. (2007), 'Ionization rate coefficients for the elements hydrogen through zinc', *Astron. Astrophys.* **466**, 771–792.

Dere, K. P. and Cook, J. W. (1979), 'The decay of the 1973 August 9 flare', *Astrophys. J.* **229**, 772–787.

Dere, K. P., Landi, E., Mason, H. E., Monsignori Fossi, B. C. and Young, P. R. (1997), 'CHIANTI - an atomic database for emission lines', *Astron. Astrophys. Suppl.* **125**, 149–173.

Dere, K. P., Landi, E., Young, P. R., Del Zanna, G., Landini, M. and Mason, H. E. (2009), 'CHIANTI - an atomic database for emission lines. IX. Ionization rates, recombination rates, ionization equilibria for the elements hydrogen through zinc and updated atomic data', *Astron. Astrophys.* **498**, 915–929.

Dialynas, K., Krimigis, S. M., Mitchell, D. G., Hamilton, D. C., Krupp, N. and Brandt, P. C. (2009), 'Energetic ion spectral characteristics in the Saturnian magnetosphere using Cassini/MIMI measurements', *Journal of Geophysical Research (Space Physics)* **114**, 1212.

Domingo, V., Fleck, B. and Poland, A. I. (1995), 'The SOHO Mission: an Overview', *Solar Phys.* **162**, 1–37.

Doyle, J. G., Giunta, A., Madjarska, M. S., Summers, H., O'Mullane, M. and Singh, A. (2013), 'Diagnosing transient ionization in dynamic events', *Astron. Astrophys.* **557**, L9.

Dudík, J., Del Zanna, G., Dzifčáková, E., Mason, H. E. and Golub, L. (2014), 'Solar Transition Region Lines Observed by the Interface Region Imaging Spectrograph: Diagnostics for the O IV and Si IV Lines', *Astrophys. J. Lett.* **780**, L12.

Dudík, J., Dzifčáková, E., Karlický, M. and Kulinová, A. (2011*a*), 'Is it possible to model observed active region coronal emission simultaneously in EUV and X-ray filters?', *Astron. Astrophys.* **531**, A115.

Dudík, J., Dzifčáková, E., Karlický, M. and Kulinová, A. (2011*b*), 'The bound-bound and free-free radiative losses for the nonthermal distributions in solar and stellar coronae', *Astron. Astrophys.* **529**, A103.

Dudík, J., Kašparová, J., Dzifčáková, E., Karlický, M. and Mackovjak, Š. (2012), 'The non-Maxwellian continuum in the X-ray, UV, and radio range', *Astron. Astrophys.* **539**, A107.

Dudík, J., Kulinová, A., Dzifčáková, E. and Karlický, M. (2009), 'EUV filter responses to plasma emission for the nonthermal κ-distributions', *Astron. Astrophys.* **505**, 1255–1264.

Dufton, P. L., Keenan, F. P. and Kingston, A. E. (1984), 'SI III emission line strengths in low density plasmas', *Mon. Not. Roy. Astron. Soc.* **209**, 1P–4P.

Dzifčáková, E. (1992), 'The ionization balance of the Fe in the solar corona for a non-Maxwellian electron distribution function', *Solar Phys.* **140**, 247–267.

Dzifčáková, E. (2002), 'The Updated fe Ionization Equilibrium for the Electron K-Distributions', *Solar Phys.* **208**, 91–111.

Dzifčáková, E. (2006*a*), 'The Influence of the Electron κ-Distribution in the Solar Corona on the Fe VIII / Fe XV Line Intensities', *Solar Phys.* **234**, 243–256.

Dzifčáková, E. (2006*b*), The Modification of Chianti for the Computation of Synthetic Emission Spectra for the Electron Non-Thermal Distributions, *in* 'SOHO-17. 10 Years of SOHO and Beyond', Vol. 617 of *ESA Special Publication*.

Dzifčáková, E. and Dudík, J. (2013), 'H to Zn Ionization Equilibrium for the Non-Maxwellian Electron κ-distributions: Updated Calculations', *Astrophys. J. Suppl. Ser.* **206**, 6.

Dzifčáková, E. and Kulinová, A. (2010), 'The Diagnostics of the κ-Distributions from EUV Spectra', *Solar Phys.* **263**, 25–41.

Dzifčáková, E. and Kulinová, A. (2011), 'Diagnostics of the κ-distribution using Si III lines in the solar transition region', *Astron. Astrophys.* **531**, A122.

Dzifčáková, E., Mackovjak, Š. and Heinzel, P. (2013), 'Kappa-distributions and Temperature Structure of the Prominence-Corona Transition Region', *Proceedings of the International Astronomical Union* **8**, 408–409.
URL: *http://journals.cambridge.org/article_S1743921313011307*

Dzifčáková, E. and Mason, H. (2008), 'Computation of Non-Maxwellian Electron Excitation Rates for Ions of Astrophysical Interest: Fe xv A Test Case', *Solar Phys.* **247**, 301–320.

Dzifčáková, E. and Tóthová, D. (2007), 'Synthetic Spectra of the Fe VIII Fe XVI Emission Lines for Electron Non-Thermal Distributions', *Solar Phys.* **240**, 211–226.

Feldman, U., Landi, E. and Doschek, G. A. (2007), 'Diagnostics of Suprathermal Electrons in Active-Region Plasmas Using He-like UV Lines', *Astrophys. J.* **660**, 1674–1682.

Feldman, U., Mandelbaum, P., Seely, J. F., Doschek, G. A. and Gursky, H. (1992), 'The potential for plasma diagnostics from stellar extreme-ultraviolet observations', *Astrophys. J. Suppl. Ser.* **81**, 387–408.

Feldman, W. C., Asbridge, J. R., Bame, S. J., Montgomery, M. D. and Gary, S. P. (1975), 'Solar wind electrons', *J. Geophys. Res.* **80**, 4181–4196.

Fletcher, L., Dennis, B. R., Hudson, H. S., Krucker, S., Phillips, K., Veronig, A., Battaglia, M., Bone, L., Caspi, A., Chen, Q., Gallagher, P., Grigis, P. T., Ji, H., Liu, W., Milligan, R. O. and Temmer, M. (2011), 'An Observational Overview of Solar Flares', *Space Sci. Rev.* **159**, 19–106.

Fludra, A. and Sylwester, J. (1986), 'Comparison of three methods used for calculation of the differential emission measure', *Solar Phys.* **105**, 323–337.

Fontenla, J., Reichmann, E. J. and Tandberg-Hanssen, E. (1988), 'The Lyman-alpha line in various solar features. I - Observations', *Astrophys. J.* **329**, 464–481.

Freeland, S. L. and Handy, B. N. (1998), 'Data Analysis with the SolarSoft System', *Solar Phys.* **182**, 497–500.

Gabriel, A. H. (1976), 'A magnetic model of the solar transition region', *Royal Society of London Philosophical Transactions Series A* **281**, 339–352.

Gloeckler, G. and Hamilton, D. C. (1987), 'AMPTE ion composition results', *Physica Scripta Volume T* **18**, 73–84.

Hannah, I. G. and Kontar, E. P. (2012), 'Differential emission measures from the regularized inversion of Hinode and SDO data', *Astron. Astrophys.* **539**, A146.

Hansen, P. C. (1992), 'Numerical tools for analysis and solution of fredholm integral equations of the first kind', *Inverse Problems* **8**(6), 849.
URL: *http://stacks.iop.org/0266-5611/8/i=6/a=005*

Holman, G. D., Sui, L., Schwartz, R. A. and Emslie, A. G. (2003), 'Electron Bremsstrahlung Hard X-Ray Spectra, Electron Distributions, and Energetics in the 2002 July 23 Solar Flare', *Astrophys. J. Lett.* **595**, L97–L101.

Jefferies, J. T., Orrall, F. Q. and Zirker, J. B. (1972), 'The Interpretation of Total Line Intensities from Optically Thin Gases. I: A General Method', *Solar Phys.* **22**, 307–316.

Judge, P. G., Hubeny, V. and Brown, J. C. (1997), 'Fundamental Limitations of Emission-Line Spectra as Diagnostics of Plasma Temperature and Density Structure', *Astrophys. J.* **475**, 275.

Kashyap, V. and Drake, J. J. (1998), 'Markov-Chain Monte Carlo Reconstruction of Emission Measure Distributions: Application to Solar Extreme-Ultraviolet Spectra', *Astrophys. J.* **503**, 450.

Kašparová, J. and Karlický, M. (2009), 'Kappa distribution and hard X-ray emission of solar flares', *Astron. Astrophys.* **497**, L13–L16.

Kletzing, C. A., Scudder, J. D., Dors, E. E. and Curto, C. (2003), 'Auroral source region: Plasma properties of the high-latitude plasma sheet', *Journal of Geophysical Research (Space Physics)* **108**, 1360.

Kosugi, T., Matsuzaki, K., Sakao, T., Shimizu, T., Sone, Y., Tachikawa, S., Hashimoto, T., Minesugi, K., Ohnishi, A., Yamada, T., Tsuneta, S., Hara, H., Ichimoto, K., Suematsu, Y., Shimojo, M., Watanabe, T., Shimada, S., Davis, J. M., Hill, L. D., Owens, J. K., Title, A. M., Culhane, J. L., Harra, L. K., Doschek, G. A. and Golub, L. (2007), 'The Hinode (Solar-B) Mission: An Overview', *Solar Phys.* **243**, 3–17.

Landi, E., Del Zanna, G., Young, P. R., Dere, K. P. and Mason, H. E. (2012), 'CHIANTI - An Atomic Database for Emission Lines. XII. Version 7 of the Database', *Astrophys. J.* **744**, 99.

Landi, E. and Landini, M. (1997), 'Simultaneous temperature and density diagnostics of optically thin plasmas', *Astron. Astrophys.* **327**, 1230–1241.

Landi, E. and Young, P. R. (2010), 'The Relative Intensity Calibration of Hinode/EIS and SOHO/SUMER', *Astrophys. J.* **714**, 636–643.

Landi, E., Young, P. R., Dere, K. P., Del Zanna, G. and Mason, H. E. (2013), 'CHIANTI - An Atomic Database for Emission Lines. XIII. Soft X-Ray Improvements and Other Changes', *Astrophys. J.* **763**, 86.

Lanzafame, A. C., Brooks, D. H. and Lang, J. (2005), 'ADAS analysis of the differential emission measure structure of the inner solar corona. II. A study of the "quiet Sun" inhomogeneities from SOHO CDS-NIS spectra', *Astron. Astrophys.* **432**, 1063–1079.

Lanzafame, A. C., Brooks, D. H., Lang, J., Summers, H. P., Thomas, R. J. and Thompson, A. M. (2002), 'ADAS analysis of the differential emission measure structure of the inner solar corona . Application of the data adaptive smoothing approach to the SERTS-89 active region spectrum', *Astron. Astrophys.* **384**, 242–272.

Le Chat, G., Issautier, K., Meyer-Vernet, N. and Hoang, S. (2011), 'Large-Scale Variation of Solar Wind Electron Properties from Quasi-Thermal Noise Spectroscopy - Ulysses Measurements', *Solar Phys.* **271**, 141–148.

Le Chat, G., Issautier, K., Meyer-Vernet, N., Zouganelis, I., Maksimovic, M. and Moncuquet, M. (2009), 'Quasi-thermal noise in space plasma: "kappa" distributions', *Physics of Plasmas* **16**(10), 102903–+.

Lee, E., Williams, D. R. and Lapenta, G. (2013), 'Spectroscopic indication of suprathermal ions in the solar corona', *ArXiv e-prints* .

Lemaire, J. and Scherer, M. (1971), 'Kinetic models of the solar wind.', *J. Geophys. Res.* **76**, 7479–7490.

Lemen, J. R., Title, A. M., Akin, D. J., Boerner, P. F., Chou, C., Drake, J. F., Duncan, D. W., Edwards, C. G., Friedlaender, F. M., Heyman, G. F., Hurlburt, N. E., Katz, N. L., Kushner,

G. D., Levay, M., Lindgren, R. W., Mathur, D. P., McFeaters, E. L., Mitchell, S., Rehse, R. A., Schrijver, C. J., Springer, L. A., Stern, R. A., Tarbell, T. D., Wuelser, J.-P., Wolfson, C. J., Yanari, C., Bookbinder, J. A., Cheimets, P. N., Caldwell, D., Deluca, E. E., Gates, R., Golub, L., Park, S., Podgorski, W. A., Bush, R. I., Scherrer, P. H., Gummin, M. A., Smith, P., Auker, G., Jerram, P., Pool, P., Soufli, R., Windt, D. L., Beardsley, S., Clapp, M., Lang, J. and Waltham, N. (2012), 'The Atmospheric Imaging Assembly (AIA) on the Solar Dynamics Observatory (SDO)', *Solar Phys.* **275**, 17–40.

Leubner, M. P. (2002), 'A Nonextensive Entropy Approach to Kappa-Distributions', *Astrophys. Space Sci.* **282**, 573–579.

Leubner, M. P. (2004), 'Fundamental issues on kappa-distributions in space plasmas and interplanetary proton distributions', *Physics of Plasmas* **11**, 1308–1316.

Leubner, M. P. (2008), 'Consequences of entropy bifurcation in non-Maxwellian astrophysical environments', *Nonlinear Processes in Geophysics* **15**, 531–540.

Leubner, M. P. and Vörös, Z. (2005), 'A Nonextensive Entropy Approach to Solar Wind Intermittency', *Astrophys. J.* **618**, 547–555.

Livadiotis, G. and McComas, D. J. (2009), 'Beyond kappa distributions: Exploiting Tsallis statistical mechanics in space plasmas', *Journal of Geophysical Research (Space Physics)* **114**, 11105.

Livadiotis, G. and McComas, D. J. (2012), 'Non-equilibrium Thermodynamic Processes: Space Plasmas and the Inner Heliosheath', *Astrophys. J.* **749**, 11.

Livadiotis, G. and McComas, D. J. (2013), 'Understanding Kappa Distributions: A Toolbox for Space Science and Astrophysics', *Space Sci. Rev.* **175**, 183–214.

Livadiotis, G., McComas, D. J., Dayeh, M. A., Funsten, H. O. and Schwadron, N. A. (2011), 'First Sky Map of the Inner Heliosheath Temperature Using IBEX Spectra', *Astrophys. J.* **734**, 1.

Mackovjak, Š. (2013), 'Temperature structure and the non-Maxwellian distributions in the solar corona', *Rigorous Thesis* **1**, 1–50.

Mackovjak, Š., Dzifčáková, E. and Dudík, J. (2013), 'On the Possibility to Diagnose the Non-Maxwellian κ-Distributions from the Hinode/EIS EUV Spectra', *Solar Phys.* **282**, 263–281.

Mackovjak, Š., Dzifčáková, E. and Dudík, J. (2014), 'Differential emission measure analysis of active region cores and quiet Sun for the non-Maxwellian κ-distributions', *Astron. Astrophys.* **564**, A130.

Maksimovic, M., Pierrard, V. and Lemaire, J. F. (1997), 'A kinetic model of the solar wind with Kappa distribution functions in the corona.', *Astron. Astrophys.* **324**, 725–734.

Maksimovic, M., Pierrard, V. and Riley, P. (1997), 'Ulysses electron distributions fitted with Kappa functions', *Geophys. Res. Lett.* **24**, 1151–1154.

Mazzotta, P., Mazzitelli, G., Colafrancesco, S. and Vittorio, N. (1998), 'Ionization balance for optically thin plasmas: Rate coefficients for all atoms and ions of the elements H to NI', *Astron. Astrophys. Suppl.* **133**, 403–409.

McIntosh, S. W. (2000), 'On the Inference of Differential Emission Measures Using Diagnostic Line Ratios', *Astrophys. J.* **533**, 1043–1052.

Meyer-Vernet, N. and Perche, C. (1989), 'Tool kit for antennae and thermal noise near the plasma frequency', *J. Geophys. Res.* **94**, 2405–2415.

Monsignori Fossi, B. C. and Landini, M. (1991), 'Models for inner corona parameters', *Advances in Space Research* **11**, 281–292.

Mulu-Moore, F. M., Winebarger, A. R. and Warren, H. P. (2011), 'Can a Long Nanoflare Storm Explain the Observed Emission Measure Distributions in Active Region Cores?', *Astrophys. J. Lett.* **742**, L6.

Nicholls, D. C., Dopita, M. A. and Sutherland, R. S. (2012), 'Resolving the Electron Temperature Discrepancies in H II Regions and Planetary Nebulae: κ-distributed Electrons', *Astrophys. J.* **752**, 148.

Nikolić, D., Gorczyca, T. W., Korista, K. T., Ferland, G. J. and Badnell, N. R. (2013), 'Suppression of Dielectronic Recombination due to Finite Density Effects', *Astrophys. J.* **768**, 82.

O'Dwyer, B., Del Zanna, G., Mason, H. E., Sterling, A. C., Tripathi, D. and Young, P. R. (2011), 'Hinode extreme-ultraviolet imaging spectrometer observations of a limb active region', *Astron. Astrophys.* **525**, A137.

Oka, M., Ishikawa, S., Saint-Hilaire, P., Krucker, S. and Lin, R. P. (2013), 'Kappa Distribution Model for Hard X-Ray Coronal Sources of Solar Flares', *Astrophys. J.* **764**, 6.

Owocki, S. P. and Scudder, J. D. (1983), 'The effect of a non-Maxwellian electron distribution on oxygen and iron ionization balances in the solar corona', *Astrophys. J.* **270**, 758–768.

Parenti, S. and Vial, J.-C. (2007), 'Prominence and quiet-Sun plasma parameters derived from FUV spectral emission', *Astron. Astrophys.* **469**, 1109–1115.

Pesnell, W. D., Thompson, B. J. and Chamberlin, P. C. (2012), 'The Solar Dynamics Observatory (SDO)', *Solar Phys.* **275**, 3–15.

Peter, H., Bingert, S., Klimchuk, J. A., de Forest, C., Cirtain, J. W., Golub, L., Winebarger, A. R., Kobayashi, K. and Korreck, K. E. (2013), 'Structure of solar coronal loops: from miniature to large-scale', *Astron. Astrophys.* **556**, A104.

Phillips, K. J. H., Feldman, U. and Landi, E. (2008), Cambridge University Press.
URL: *http://dx.doi.org/10.1017/CBO9780511585968.017*

Pierrard, V. and Lazar, M. (2010), 'Kappa Distributions: Theory and Applications in Space Plasmas', *Solar Phys.* **267**, 153–174.

Pierrard, V. and Lemaire, J. (1996), 'Lorentzian ion exosphere model', *J. Geophys. Res.* **101**, 7923–7934.

Pierrard, V., Maksimovic, M. and Lemaire, J. (1999), 'Electron velocity distribution functions from the solar wind to the corona', *J. Geophys. Res.* **104**, 17021–17032.

Pilipp, W. G., Muehlhaeuser, K.-H., Miggenrieder, H., Montgomery, M. D. and Rosenbauer, H. (1987), 'Characteristics of electron velocity distribution functions in the solar wind derived from the HELIOS plasma experiment', *J. Geophys. Res.* **92**, 1075–1092.

Pinfield, D. J., Keenan, F. P., Mathioudakis, M., Phillips, K. J. H., Curdt, W. and Wilhelm, K. (1999), 'Evidence for Non-Maxwellian Electron Energy Distributions in the Solar Transition Region: Si III Line Ratios from SUMER', *Astrophys. J.* **527**, 1000–1008.

Prato, M., Piana, M., Brown, J. C., Emslie, A. G., Kontar, E. P. and Massone, A. M. (2006), 'Regularized Reconstruction of the Differential Emission Measure from Solar Flare Hard X-Ray Spectra', *Solar Phys.* **237**, 61–83.

Qureshi, M. N. S., Pallocchia, G., Bruno, R., Cattaneo, M. B., Formisano, V., Reme, H., Bosqued, J. M., Dandouras, I., Sauvaud, J. A., Kistler, L. M., Möbius, E., Klecker, B., Carlson, C. W., McFadden, J. P., Parks, G. K., McCarthy, M., Korth, A., Lundin, R., Balogh, A. and Shah, H. A. (2003), Solar Wind Particle Distribution Function Fitted via the Generalized Kappa Distribution Function: Cluster Observations, *in* M. Velli, R. Bruno, F. Malara, & B. Bucci, ed., 'Solar Wind Ten', Vol. 679 of *American Institute of Physics Conference Series*, pp. 489–492.

Reale, F., Testa, P., Klimchuk, J. A. and Parenti, S. (2009), 'Evidence of Widespread Hot Plasma in a Nonflaring Coronal Active Region from Hinode/X-Ray Telescope', *Astrophys. J.* **698**, 756–765.

Schippers, P., Blanc, M., André, N., Dandouras, I., Lewis, G. R., Gilbert, L. K., Persoon, A. M., Krupp, N., Gurnett, D. A., Coates, A. J., Krimigis, S. M., Young, D. T. and Dougherty, M. K. (2008), 'Multi-instrument analysis of electron populations in Saturn's magnetosphere', *Journal of Geophysical Research (Space Physics)* **113**, 7208.

Schmelz, J. T., Jenkins, B. S. and Pathak, S. (2013), 'Atmospheric Imaging Assembly Observations of Coronal Loops: Cross-field Temperature Distributions', *Astrophys. J.* **770**, 14.

Schmelz, J. T. and Martens, P. C. H. (2006), 'Multithermal Analysis of a SOHO/CDS Coronal Loop', *Astrophys. J. Lett.* **636**, L49–L52.

Schmelz, J. T., Nasraoui, K., Rightmire, L. A., Kimble, J. A., del Zanna, G., Cirtain, J. W., DeLuca, E. E. and Mason, H. E. (2009), 'Are Coronal Loops Isothermal or Multithermal?', *Astrophys. J.* **691**, 503–515.

Schmelz, J. T., Rightmire, L. A., Saar, S. H., Kimble, J. A., Worley, B. T. and Pathak, S. (2011), 'Warm and Fuzzy: Temperature and Density Analysis of an Fe XV EUV Imaging Spectrometer Loop', *Astrophys. J.* **738**, 146.

Schmelz, J. T., Worley, B. T., Anderson, D. J., Pathak, S., Kimble, J. A., Jenkins, B. S. and Saar, S. H. (2011), 'Isothermal and Multithermal Analysis of Coronal Loops Observed with Atmospheric Imaging Assembly. II. 211 Å Selected Loops', *Astrophys. J.* **739**, 33.

Scudder, J. D. (1992), 'Why all stars should possess circumstellar temperature inversions', *Astrophys. J.* **398**, 319–349.

Scudder, J. D. and Karimabadi, H. (2013), 'Ubiquitous Non-thermals in Astrophysical Plasmas: Restating the Difficulty of Maintaining Maxwellians', *Astrophys. J.* **770**, 26.

Shoub, E. C. (1983), 'Invalidity of local thermodynamic equilibrium for electrons in the solar transition region. I - Fokker-Planck results', *Astrophys. J.* **266**, 339–369.

Siarkowski, M., Falewicz, R., Kepa, A. and Rudawy, P. (2008), 'Diagnostic of the temperature and differential emission measure (DEM) based on Hinode/XRT data', *Annales Geophysicae* **26**, 2999–3005.

Sturrock, P. A. and Hartle, R. E. (1966), 'Two-Fluid Model of the Solar Wind', *Physical Review Letters* **16**, 628–631.

Summers, H. P., Dickson, W. J., O'Mullane, M. G., Badnell, N. R., Whiteford, A. D., Brooks, D. H., Lang, J., Loch, S. D. and Griffin, D. C. (2006), 'Ionization state, excited populations and emission of impurities in dynamic finite density plasmas: I. The generalized collisional radiative model for light elements', *Plasma Physics and Controlled Fusion* **48**, 263–293.

Sylwester, B., Sylwester, J. and Phillips, K. J. H. (2010), 'Soft X-ray coronal spectra at low activity levels observed by RESIK', *Astron. Astrophys.* **514**, A82.

Sylwester, J., Schrijver, J. and Mewe, R. (1980), 'Multitemperature analysis of solar X-ray line emission', *Solar Phys.* **67**, 285–309.

Thompson, A. M. (1990), 'Adaptive smoothing and its application to the inversion of the Crab synchrotron spectrum', *Astron. Astrophys.* **240**, 209–215.

Tikhonov, A. N. (1963), 'Solution of incorrectly formulated problems and the regularization method', *Soviet Math. Dokl.* **4**, 1035–1038.

Treumann, R. A. and Jaroschek, C. H. (2008), 'Gibbsian Theory of Power-Law Distributions', *Physical Review Letters* **100**(15), 155005.

Tripathi, D., Klimchuk, J. A. and Mason, H. E. (2011), 'Emission Measure Distribution and Heating of Two Active Region Cores', *Astrophys. J.* **740**, 111.

Tripathi, D., Mason, H. E., Dwivedi, B. N., del Zanna, G. and Young, P. R. (2009), 'Active Region Loops: Hinode/Extreme-Ultraviolet Imaging Spectrometer Observations', *Astrophys. J.* **694**, 1256–1265.

Tsallis, C. (1995), 'Non-extensive thermostatistics: brief review and comments', *Physica A Statistical Mechanics and its Applications* **221**, 277–290.

Tsallis, C. (2009), *Introduction to Nonextensive Statistical Mechanics*, Springer New York.

Vasyliunas, V. M. (1968), 'A Survey of Low-Energy Electrons in the Evening Sector of the Magnetosphere with OGO 1 and OGO 3', *J. Geophys. Res.* **73**, 2839.

Veck, N. J., Strong, K. T., Jordan, C., Simnett, G. M., Cargill, P. J. and Priest, E. R. (1984), 'The development and cooling of a solar limb-flare', *Mon. Not. Roy. Astron. Soc.* **210**, 443–462.

Vernazza, J. E., Avrett, E. H. and Loeser, R. (1981), 'Structure of the solar chromosphere. III - Models of the EUV brightness components of the quiet-sun', *Astrophys. J. Suppl. Ser.* **45**, 635–725.

Vernazza, J. E. and Reeves, E. M. (1978), 'Extreme ultraviolet composite spectra of representative solar features', *Astrophys. J. Suppl. Ser.* **37**, 485–513.

Viall, N. M. and Klimchuk, J. A. (2011), 'Patterns of Nanoflare Storm Heating Exhibited by an Active Region Observed with Solar Dynamics Observatory/Atmospheric Imaging Assembly', *Astrophys. J.* **738**, 24.

Vocks, C. and Mann, G. (2003), 'Generation of Suprathermal Electrons by Resonant Wave-Particle Interaction in the Solar Corona and Wind', *Astrophys. J.* **593**, 1134–1145.

Wang, T., Thomas, R. J., Brosius, J. W., Young, P. R., Rabin, D. M., Davila, J. M. and Del Zanna, G. (2011), 'Underflight Calibration of SOHO/CDS and Hinode/EIS with EUNIS-07', *Astrophys. J. Suppl. Ser.* **197**, 32.

Wannawichian, S., Ruffolo, D. and Kartavykh, Y. Y. (2003), 'Ionization Fractions of Slow Ions in a Plasma with Kappa Distributions for the Electron Velocity', *Astrophys. J. Suppl. Ser.* **146**, 443–457.

Warren, H. P., Brooks, D. H. and Winebarger, A. R. (2011), 'Constraints on the Heating of High-temperature Active Region Loops: Observations from Hinode and the Solar Dynamics Observatory', *Astrophys. J.* **734**, 90.

Warren, H. P., Winebarger, A. R. and Brooks, D. H. (2010), 'Evidence for Steady Heating: Observations of an Active Region Core with Hinode and TRACE', *Astrophys. J.* **711**, 228–238.

Warren, H. P., Winebarger, A. R. and Brooks, D. H. (2012), 'A Systematic Survey of High-temperature Emission in Solar Active Regions', *Astrophys. J.* **759**, 141.

Wenzel, K.-P., Marsden, R. G., Page, D. E. and Smith, E. J. (1989), 'Ulysses: The first high-latitude heliospheric mission', *Advances in Space Research* **9**, 25–29.

Wilhelm, K., Curdt, W., Marsch, E., Schühle, U., Lemaire, P., Gabriel, A., Vial, J.-C., Grewing, M., Huber, M. C. E., Jordan, S. D., Poland, A. I., Thomas, R. J., Kühne, M., Timothy, J. G., Hassler, D. M. and Siegmund, O. H. W. (1995), 'SUMER - Solar Ultraviolet Measurements of Emitted Radiation', *Solar Phys.* **162**, 189–231.

Winebarger, A. R. (2012), The Frequency of Heating in Active Region Cores: Results from the Fifth Coronal Loops Workshop, *in* L. Golub, I. De Moortel and T. Shimizu, eds, 'Fifth Hinode Science Meeting', Vol. 456 of *Astronomical Society of the Pacific Conference Series*, p. 103.

Winebarger, A. R., Schmelz, J. T., Warren, H. P., Saar, S. H. and Kashyap, V. L. (2011), 'Using a Differential Emission Measure and Density Measurements in an Active Region Core to Test a Steady Heating Model', *Astrophys. J.* **740**, 2.

Winebarger, A. R., Warren, H. P., Schmelz, J. T., Cirtain, J., Mulu-Moore, F., Golub, L. and Kobayashi, K. (2012), 'Defining the "Blind Spot" of Hinode EIS and XRT Temperature Measurements', *Astrophys. J. Lett.* **746**, L17.

Withbroe, G. L. (1975), 'The analysis of XUV emission lines', *Solar Phys.* **45**, 301–317.

Wood, B. E. and Laming, J. M. (2013), 'The Coronal Abundances of Mid-F Dwarfs', *Astrophys. J.* **768**, 122.

Xiao, F., Zhou, Q., Li, C. and Cai, A. (2008), 'BRIEF COMMUNICATION: Modeling solar energetic particle by a relativistic kappa-type distribution', *Plasma Physics and Controlled Fusion* **50**(6), 062001.

Young, P. R. (2007), 'Density diagnostics for eis'.
   URL: *http://www.pyoung.org/hinode/recommended-diags.pdf*

Young, P. R., Del Zanna, G., Mason, H. E., Dere, K. P., Landi, E., Landini, M., Doschek, G. A., Brown, C. M., Culhane, L., Harra, L. K., Watanabe, T. and Hara, H. (2007), 'EUV Emission Lines and Diagnostics Observed with Hinode/EIS', *Pub. Astron. Soc. Japan* **59**, 857.

Young, P. R., Watanabe, T., Hara, H. and Mariska, J. T. (2009), 'High-precision density measurements in the solar corona. I. Analysis methods and results for Fe XII and Fe XIII', *Astron. Astrophys.* **495**, 587–606.

Zhang, Y., Liu, X.-W. and Zhang, B. (2014), 'H I Free-Bound Emission of Planetary Nebulae with Large Abundance Discrepancies: Two-component Models versus κ-distributed Electrons', *Astrophys. J.* **780**, 93.

Zharkova, V. V., Arzner, K., Benz, A. O., Browning, P., Dauphin, C., Emslie, A. G., Fletcher, L., Kontar, E. P., Mann, G., Onofri, M., Petrosian, V., Turkmani, R., Vilmer, N. and Vlahos, L. (2011), 'Recent Advances in Understanding Particle Acceleration Processes in Solar Flares', *Space Sci. Rev.* **159**, 357–420.

Zhitnik, I. A., Kuzin, S. V., Urnov, A. M., Beigman, I. L., Bozhenkov, S. A. and Tolstikhina, I. Y. (2005), 'Extreme vacuum ultraviolet solar spectra obtained during the SPIRIT experiment aboard CORONAS-F: A catalog of lines in the range 280 330 Å', *Astronomy Letters* **31**, 37–56.

Zouganelis, I. (2008), 'Measuring suprathermal electron parameters in space plasmas: Implementation of the quasi-thermal noise spectroscopy with kappa distributions using in situ Ulysses/URAP radio measurements in the solar wind', *Journal of Geophysical Research (Space Physics)* **113**, 8111.

Zouganelis, I., Maksimovic, M., Meyer-Vernet, N., Lamy, H. and Issautier, K. (2004), 'A Transonic Collisionless Model of the Solar Wind', *Astrophys. J.* **606**, 542–554.

Zouganelis, I., Meyer-Vernet, N., Landi, S., Maksimovic, M. and Pantellini, F. (2005), 'Acceleration of Weakly Collisional Solar-Type Winds', *Astrophys. J. Lett.* **626**, L117–L120.